

AD 674644

AD

## USAAVLABS TECHNICAL REPORT 68-52

# INVESTIGATION OF THE DOWNWASH ENVIRONMENT GENERATED BY V/STOL AIRCRAFT OPERATING IN GROUND EFFECT

By

M. George

E. Kisielowski

D. S. Douglas

July 1968

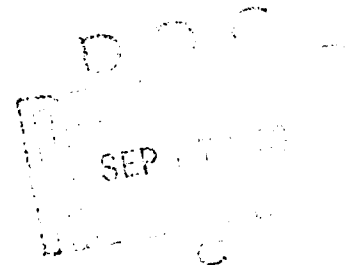
**U. S. ARMY AVIATION MATERIEL LABORATORIES  
FORT EUSTIS, VIRGINIA**

CONTRACT DA 44-177-AMC-316(T)

DYNASCIENCES CORPORATION

BLUE BELL, PENNSYLVANIA

*This document has been approved  
for public release and sale; its  
distribution is unlimited.*



## Disclaimers

The findings in this report are not to be construed as an official Department of the Army position unless so designated by other authorized documents.

When Government drawings, specifications, or other data are used for any purpose other than in connection with a definitely related Government procurement operation, the United States Government thereby incurs no responsibility nor any obligation whatsoever, and the fact that the Government may have formulated, furnished, or in any way supplied said drawings, specifications, or other data is not to be regarded by implication or otherwise as in any manner licensing the holder or any other person or corporation, or conveying any rights or permission, to manufacture, use, or sell any patented invention that may in any way be related thereto.

## Disposition Instructions

Destroy this report when no longer needed. Do not return it to originator.

[illegible]



**DEPARTMENT OF THE ARMY**  
**U. S. ARMY AVIATION MATERIEL LABORATORIES**  
**FORT EUSTIS, VIRGINIA 23604**

This report was prepared by the Dynasciences Corporation under the terms of Contract DA 44-177-AMC-316(T). It reports on the work concluded in an investigation of the dust cloud generated by several types of VTOL aircraft when hovering over a specified terrain.

The results of the analytical investigation were compared with experimental results gathered under Contract DA 44-177-AMC-289(T) and with a series of tests conducted by Dynasciences in conjunction with the above program.

This command concurs in the conclusions and recommendations presented herein.

Project 1T021701A047  
Contract DA 44-177-AMC-316(T)  
USAAVLABS Technical Report 68-52

July 1968

INVESTIGATION OF THE DOWNWASH  
ENVIRONMENT GENERATED BY V/STOL  
AIRCRAFT OPERATING IN GROUND EFFECT

Dynasciences Corporation Report DCR-275

By

M. George  
E. Kisielowski  
D.S. Douglas

Prepared by

Dynasciences Corporation  
Blue Bell, Pennsylvania

for

U. S. ARMY AVIATION MATERIEL LABORATORIES  
FORT EUSTIS, VIRGINIA

This document has been approved  
for public release and sale, its  
distribution is unlimited

## SUMMARY

Analytical methods are developed for determining the downwash environment generated by multirotor/propeller V/STOL aircraft configurations operating in ground proximity.

These methods are utilized to compute rotor flow field and contaminant dust cloud characteristics (including particle density and size distributions) for the H-21, XC-142, X-22A, X-19A, and XV-5A aircraft. The effects of the contaminated atmosphere on pilot's visibility, ground equipment, and personnel are also determined for these aircraft.

The theoretically predicted results are generally in good agreement with the limited test data. Additional full-scale test data are required to verify further the assumptions inherent in the theory.

## FOREWORD

This report presents the results of an investigation of the downwash environment generated by V/STOL aircraft operating in ground proximity.

The work was performed by the Dynasciences Corporation, Blue Bell, Pennsylvania, for the U. S. Army Aviation Materiel Laboratories (USAAVLABS), Fort Eustis, Virginia, under Contract DA 44-177-AMC-316(I) during the period from August 1965 through March 1968.

The Army technical representative was Mr. Joel Terry, who was assisted by Mr. Blair Poteate and Mr. G. William Hogg. The contributions of the Army personnel to this work are gratefully acknowledged.

The following Dynasciences Corporation personnel participated in this program:

- Mr. M. George - Project Engineer
- Mr. D. S. Douglas - Aeronautical Engineer
- Mr. J. Tang - Aeronautical Engineer
- Mr. S. Mills - Sr. Aeronautical Engineer
- Mr. E. Kisielowski - Manager, Aeronautics
- Dr. A. A. Perlmutter - Senior Vice President

## CONTENTS

	<u>Page</u>
SUMMARY . . . . .	iii
FOREWORD . . . . .	v
LIST OF ILLUSTRATIONS . . . . .	viii
LIST OF TABLES . . . . .	xiv
LIST OF SYMBOLS . . . . .	xv
I INTRODUCTION . . . . .	1
II THEORETICAL ANALYSIS . . . . .	3
A. FLOW FIELD . . . . .	3
B. DOWNWASH SIGNATURES . . . . .	27
C. DOWNWASH SIGNATURE EFFECTS . . . . .	42
III DOWNWASH ENVIRONMENT RESULTS FOR VARIOUS V/STOL AIRCRAFT . . . . .	48
A. FLOW FIELD . . . . .	48
B. DOWNWASH SIGNATURES . . . . .	63
C. DOWNWASH SIGNATURE EFFECTS . . . . .	94
IV CONCLUSIONS AND RECOMMENDATIONS . . . . .	111
V REFERENCES . . . . .	112
APPENDIX. SURFACE EROSION TEST DATA . . . . .	115
DISTRIBUTION . . . . .	129

## LIST OF ILLUSTRATIONS

<u>Figure</u>		<u>Page</u>
1	Representation of the Flow Field for a Typical Two-Rotor/Propeller V/STOL Aircraft Hovering in Ground Effect . . . . .	4
2	Definition of the Flow Regions in the Vicinity of Mutually Interacting Propellers/Rotors . . . . .	5
3	Variation of Axial Velocity Outside Vortex Cylinder Versus Radial Distance for Axial Distances of 0.5R and 1R Below the Rotor Plane . . . . .	10
4	Effect of Thrust Coefficient and Solidity on the Ground Effect Inflow Correction Factor in Hovering . . . . .	12
5	Flow Field in the Vicinity of a Hovering Rotor, Out of Ground Effect . . . . .	13
6	Downwash Velocity Distribution Below the Rotor in Ground Effect (Region 2) . . . . .	15
7	The Wall Jet Velocity Profile . . . . .	17
8	Test Data on the Decay of Dynamic Pressure With Axial Distance From the Jet Exit . . . . .	18
9	Downwash Velocity in Ground Effect for a 75-Foot Rotor at $H/R = 0.44$ . . . . .	23
10	Schematic Representation of the Flow Field in the Recirculation Region . . . . .	24
11	Schematic Representation of the Flow Field Along the Interaction Flow . . . . .	26



<u>Figure</u>		<u>Page</u>
12	Correction Factor for Determining Velocities Within the Interaction Plane . . . . .	28
13	Definition of Parameters Within the Interaction Plane . . . . .	29
14	Schematic Representation of a Lifting Rotor Vortex System in Ground Effect . . . . .	32
15	Schematic Representation of Dust Cloud Geometry . . . . .	39
16	Variation of Terminal Velocity of Particles With Particle Diameter . . . . .	41
17	The Relation Between Visual Angle and Background Intensity for Test Objects of Constant Threshold Contrast . . . . .	43
18	Pilot's Line of Sight Relative to Vehicle	46
19	Comparison of Wall Jet Velocity Distributions for Various Aircraft at the Start of the Wall Jet. Wheels on the Ground . . . . .	50
20	Comparison of Wall Jet Velocity Distributions for Various Aircraft at a Common Radial Station ( $X = 90$ Feet). Wheels on the Ground . . . . .	51
21	Wall Jet Velocity Distribution for XC-142 Aircraft at Various Radial Stations. Wheel Clearance, $H_w = 50$ Feet . . . . .	52
22	Variation of Maximum Surface Dynamic Pressure Along the Ground for Various Aircraft. Wheels on the Ground . . . . .	54
23	Horizontal and Vertical Velocity Components Along the Interaction Plane for the H-21 Aircraft. Wheels on the Ground . . . . .	57

<u>Figure</u>		<u>Page</u>
24	Horizontal and Vertical Velocity Components Along Interaction Plane for the XC-142 Air- craft. Wheels on the Ground . . . . .	58
25	Horizontal and Vertical Velocity Components Along Interaction Plane for the X-22A Air- craft. Wheels on the Ground . . . . .	59
26	Horizontal and Vertical Velocity Components Along Interaction Plane for the X-19A Air- craft. Wheels on the Ground . . . . .	60
27	Horizontal and Vertical Velocity Components Along Interaction Plane for the XV-5A Air- craft. Wheels on the Ground . . . . .	61
28	Horizontal and Vertical Velocity Components Along Interaction Plane for the XC-142 Air- craft. $H_0 = 50$ Feet . . . . .	62
29	Contour Plots of Maximum Surface Dynamic Pressure Along the Ground for the H-21 Aircraft. Wheels on the Ground . . . . .	64
30	Contour Plots of Maximum Surface Dynamic Pressure Along the Ground for the XC-142 Aircraft. Wheels on the Ground . . . . .	65
31	Contour Plots of Maximum Surface Dynamic Pressure Along the Ground for the X-22A Aircraft. Wheels on the Ground . . . . .	66
32	Contour Plots of Maximum Surface Dynamic Pressure Along the Ground for the X-19A Aircraft. Wheels on the Ground . . . . .	67
33	Contour Plots of Maximum Surface Dynamic Pressure Along the Ground for the XV-5A Aircraft. Wheels on the Ground . . . . .	68
34	Contour Plots of Maximum Surface Dynamic Pressure Along the Ground for the XC-142 Aircraft. $H_0 = 50$ Feet . . . . .	69

<u>Figure</u>		<u>Page</u>
35	Ground Sample Particle Size Distribution	71
36	Dust Cloud Size and Shape for the H-21 Helicopter . . . . .	72
37	Dust Cloud Size and Shape for the XC-142 Aircraft . . . . .	73
38	Dust Cloud Size and Shape for the X-22A Interaction Plane . . . . .	74
39	Dust Cloud Size and Shape for the X-19A Interaction Plane . . . . .	75
40	Dust Cloud Size and Shape for the XV-5A Aircraft . . . . .	76
41	Dust Cloud Size and Shape for the XC-142 Aircraft, H <sub>2</sub> 50 Feet . . . . .	77
42	Maximum Boundary of Cloud versus Slipstream Dynamic Pressure for Various Aircraft . . .	78
43	Maximum Cloud Height versus Slipstream Dynamic Pressure for Various Aircraft . . .	79
44	Particle Density Distribution for the H-21 Helicopter . . . . .	81
45	Particle Density Distribution for the XC-142 Aircraft . . . . .	82
46	Particle Density Distribution for the X-22A Aircraft . . . . .	83
47	Particle Density Distribution for the X-19A Aircraft . . . . .	84
48	Particle Density Distribution for the XV-5A Aircraft . . . . .	85
49	Particle Density Distribution for the XC-142 Aircraft, H <sub>2</sub> 50 Feet . . . . .	86

<u>Figure</u>		<u>Page</u>
50	Particle Size Profiles (Ground Sample and the Airborne Sample at the Rotor Plane) for Various Aircraft . . . . .	89
51	Particle Size Distributions for the H-21 Aircraft . . . . .	91
52	Particle Size Distributions for the XC-142 Aircraft . . . . .	92
53	Particle Size Distributions for the XV-5A Aircraft . . . . .	93
54	Variation of Incipient Erosion With Terrain	95
55	Light Transmittance for the H-21 Aircraft. Wheels on Ground, $\psi = 45^\circ$ . . . . .	96
56	Light Transmittance for the XC-142 Aircraft. Wheels on Ground, $\psi = 45^\circ$ . . . . .	97
57	Light Transmittance for the X-22A Aircraft. Wheels on Ground, $\psi = 45^\circ$ . . . . .	98
58	Light Transmittance for the X-19A Aircraft. Wheels on Ground, $\psi = 45^\circ$ . . . . .	99
59	Light Transmittance for the XV-5A Aircraft. Wheels on Ground, $\psi = 45^\circ$ . . . . .	100
60	Light Transmittance for the XC-142 Aircraft. Wheels on Ground, Wheel Height = 50 Feet	101
61	Perceivable Size of an Object Sighted Through Dust Clouds Generated by Various Aircraft	103
62	Variation of Engine Ingested Sand and Dust With Engine Airflow for a 5-Percent Reduction in Normal Rated Power . . . . .	105

<u>Figure</u>		<u>Page</u>
63	Engine Net Operational Gain for a 5-Percent Reduction in Normal Rated Power . . . . .	108
64	Effects of Rotor Downwash Upon Man and Equipment for Various Aircraft. Wheels on the Ground . . . . .	109
65	Particle Trap Layout . . . . .	117
66	Mass Erosion Rates of Particles Entrained Forward of the H-21 Helicopter, Test Condition I - Phillips Drop Zone, H = 17 Feet	124
67	Mass Erosion Rates of Particles Entrained Outboard of the H-21 Helicopter, Test Condition II - Phillips Drop Zone, H = 17 Feet	125
68	Particle Size Distribution Forward of the H-21 Helicopter, Test Condition I - Phillips Drop Zone, H = 17 Feet . . . . .	126
69	Particle Size Distribution Outboard of the H-21 Helicopter, Test Condition II - Phillips Drop Zone, H = 17 Feet . . . . .	127

# LIST OF TABLES

<u>Table</u>		<u>Page</u>
I	Geometric Parameters of V/STOL Aircraft	49
II	Horizontal Components of the Velocities in the Recirculation Region. Wheels on the Ground . . . . .	55
III	Horizontal Components of the Velocities in the Recirculation Region - $H_W = 50$ Feet .	56
IV	Predicted and Measured Average Particle Densities in the Close Vicinity of Rotor Planes for the Selected Aircraft . . . .	88
V	Results of Dust Ingestion by Various V/STOL Engines for a 5-Percent Reduction in Normal Rated Power . . . . .	107
VI	Gradation Test Results - Test Condition I, Run No. 5 . . . . .	120
VII	Gradation Test Results - Test Condition I, Run No. 7 . . . . .	121
VIII	Gradation Test Results - Test Condition II, Run No. 4 . . . . .	122
IX	Gradation Test Results - Test Condition II, Run No. 9 . . . . .	123

## SYMBOLS

A.a.B	constants as defined in the text
$A_p$	particle cross-sectional area. $\frac{\pi}{4} D_p^2$ . ft <sup>2</sup>
C	contrast between sight of object and its background
$C_u, C_y$	wall jet constants
$C_1, C_2$	constants as defined in text
$C_T$	rotor thrust coefficient out of ground effect
D	diameter of rotor. ft
$D_e$	effective rotor diameter of the contracted slipstream. ft
$D_p$	particle diameter. mm or micron
$\bar{D}_p$	mean particle diameter. mm or microns
$D_{p\%}$	mean particle diameter. percent finer by weight
$D_S$	diameter of standard 0.25 mm size particle, mm
$D_{pw}$	max water particle diameter (.50 mm)
D.L.	disc loading. lb/ft <sup>2</sup>
d	cloud penetration distance along pilot's line of vision. ft
$e_A$	percent finer by weight of airborne particles of size A

$e_G$	percent finer by weight of ground particles of size A
$(e_G)_{\max}$	percent finer by weight of ground particles of size $A_{\max}$
$F_h$	correction factor as defined in the text
H	rotor height above the ground, ft
$H_c$	height of dust cloud, ft
$H_w$	aircraft wheel height from the ground, ft
h	vertical distance measured from rotor plane, ft
$h_0$	wall jet height ( $u = 0.01 u_m$ ), ft
$I_0$	background light intensity, foot-lambert
$I_s$	object light intensity, foot-lambert
K	logarithmic constant as defined in the text
$k_t$	terrain erosion factor
$k_g$	ground effect factor
$X_L, Y_L$	half-distance between rotor, along the X or Y axis, ft
$\delta, \phi$	polar coordinates located at the center of vortex spiral
$L_v$	vertical location of dust cloud boundary from the center of vortex spiral
n	particle mass flow rate per unit area, lb/sec-ft <sup>2</sup>
$n_0$	particle mass flow rate per unit area along the ground, lb/sec-ft <sup>2</sup>



$m$	particle mass flow rate per unit width, lb/sec-ft
$N$	number of particles per cubic ft of air
$q_N$	dynamic pressure of a fully developed slipstream, $= \frac{1}{2} \rho U_N^2$ , lb/ft <sup>2</sup>
$q_s$	surface dynamic pressure along the ground, lb/ft <sup>2</sup>
$(q_s)_{eff}$	effective surface dynamic pressure along the ground, lb/ft <sup>2</sup>
$q_{smax}$	maximum surface dynamic pressure along the ground, $\frac{1}{2} \rho (U_s)_{max}^2$ , lb/ft <sup>2</sup>
$R$	rotor radius, ft
$R_c$	radius of dust cloud, ft
$R_v$	radius of vortex spiral in dust cloud, ft
$r$	radial location, ft
$Sh$	horizontal component of distance between pilot and object along pilot's line of sight, ft
$S$	distance from pilot to object along pilot's line of sight, ft
$T$	light transmittance
$T_f$	velocity interference correction factor
$t$	axial distance from jet nozzle exit, ft
$u$	local velocity within the wall jet, ft/sec
$\bar{U}$	average induced velocity at the rotor disc in ground effect, ft/sec

$\bar{U}_M$	mean momentum velocity at the jet nozzle exit, ft/sec
$u_m$	maximum velocity within the wall jet, ft/sec
$U_W$	velocity of fully developed slipstream, ft/sec
$U_0$	momentum value of induced velocity at the rotor disc, ft/sec
$U_r$	radial velocity component, ft/sec
$(U_s)_{max}$	maximum surface velocity along the ground, ft/sec
$U_x$	longitudinal velocity component along X axis, ft/sec
$U_y$	lateral velocity component along Y axis, ft/sec
$U_z$	axial velocity component, ft/sec
$U_{IGE}$	induced velocity in ground effect, ft/sec
$U_{OGE}$	induced velocity out of ground effect, ft/sec
$v$	velocity along a stream tube, ft/sec
$v_d$	drag velocity as defined in the text, ft/sec
$X, Y, Z$	right angled coordinate system with origin on the ground
$y$	height within the wall jet, ft
$y_{\frac{1}{2}}$	height within the wall jet where $u/u_m = \frac{1}{2}$ , ft
$z_v$	vertical distance above the ground to vortex spiral center, ft
$\alpha, \beta, \gamma$	angles as defined in the text, degrees
$\theta$	flow angle in the interaction plane, degrees
$\rho$	air density, slugs/cu ft

$\rho$	particle density, lb/cu ft of air
$\rho_w$	water particle density, lb/cu ft
$\sigma$	rotor solidity, $b_c/H_R$
$r$	shearing force or drag per square cm
$\phi$	polar angle within vortex spiral
$\phi_0$	constant as defined in the text
$\psi$	aircraft heading angle relative to sighted object, degrees

## I. INTRODUCTION

The downwash environment problems associated with V/STOL aircraft operating in ground proximity have become greatly magnified by the new generation of high-disc-loading multi-lift V/STOL aircraft. Due to the complexity of the flow mechanism in the vicinity of a lifting rotor operating in ground effect, formulation of an exact mathematical model for rotor downwash environment is indeed very difficult. For this reason, the previous work on the subject is limited to extremely specialized analyses covering only a very narrow portion of overall rotor downwash problems. The test information in this field consists of uncoordinated small-scale or full-scale model data without proper definition of pertinent test parameters. Consequently, there exists a need for a simple and reliable analytical method supplemented by test data which can be readily applied for predicting downwash environment of various V/STOL configurations operating in ground proximity.

The objective of this program is to develop a relatively simple mathematical model to predict the relationship which exists between V/STOL lift devices and their orientation on the aircraft as they relate to the generation of the contaminated atmosphere surrounding hovering aircraft. This model is utilized to compute contaminant cloud size and shape, particle density and size distributions within the dust cloud, and the effects of the contaminant atmosphere on pilot's visibility, ground equipment, and personnel.

This mathematical model is based on the available rotor downwash theory for the flow regions where it is considered to be most applicable, on the limited test data for the flow regions where the theory is not considered to be applicable, and on the semiempirical methods for the flow regions where both the available theory and the test data are practically nonexistent.

Section II of this report presents the details of the mathematical model developed under this program.

Section III contains the computed results of the contaminant downwash environment for the H-21, XC-142, X-22A, X-19A, and XV-5A aircraft operating in ground effect. Some test data on ground surface mass flow rates obtained during this program for the H-21 helicopter are presented in the appendix. The theory developed herein is correlated with the available test data wherever possible.

## II. THEORETICAL ANALYSIS

The downwash signature of a V/STOL aircraft operating over unprepared landing surfaces is defined as the resultant operational environment that the aircraft generates less the natural environment existing prior to the aircraft's arrival. The downwash signature can be determined by first defining the flow field in the vicinity of the aircraft hovering in ground effect and then by determining the resulting dust cloud size and content associated with this flow field.

### A. FLOW FIELD

The analytical treatment of the flow field in the vicinity of a lifting rotor in ground effect is a formidable task. Several investigators have attempted to formulate analyses for this purpose. However, as indicated in Reference 1, these analyses are considered to be inadequate. More rigorous computer methods have recently been developed to better define the flow mechanism during ground impingement of uniform jets. However, these methods could not be applied to the present program.

For this program, existing analyses and experimental data such as those of Reference 2 were applied to the regions of the downwash flow field where they were considered to be most suitable.

An artist's conception of the flow field in the vicinity of a typical two-rotor/propeller V/STOL aircraft hovering in ground effect is shown in Figure 1.

In order to facilitate the analysis, the flow field of a two-propeller/rotor configuration represented in Figure 1 is subdivided into a number of isolated flow regions as shown in Figure 2. The flow field in each of these regions is as follows.

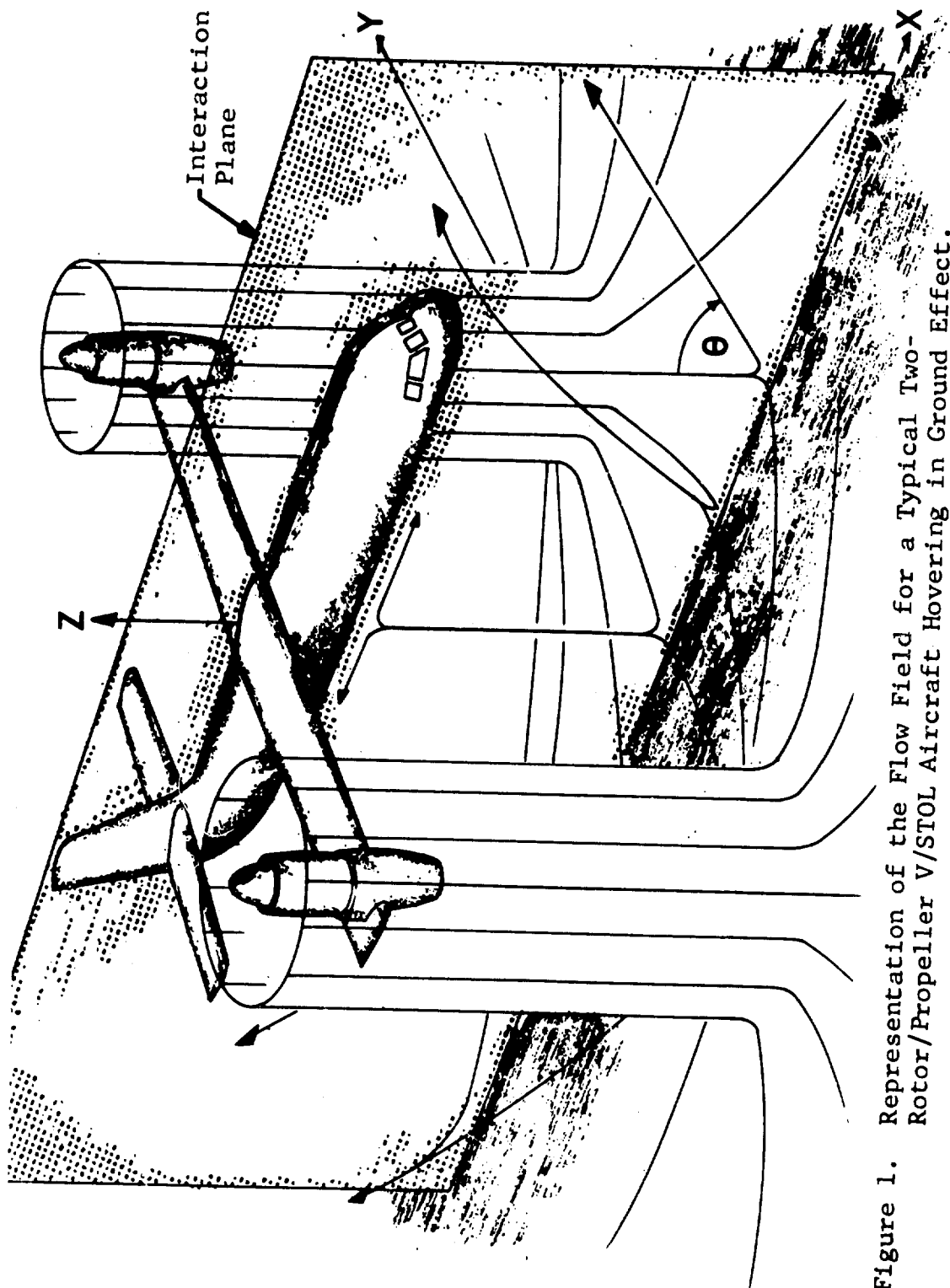


Figure 1. Representation of the Flow Field for a Typical Two-Rotor/Propeller V/STOL Aircraft Hovering in Ground Effect.

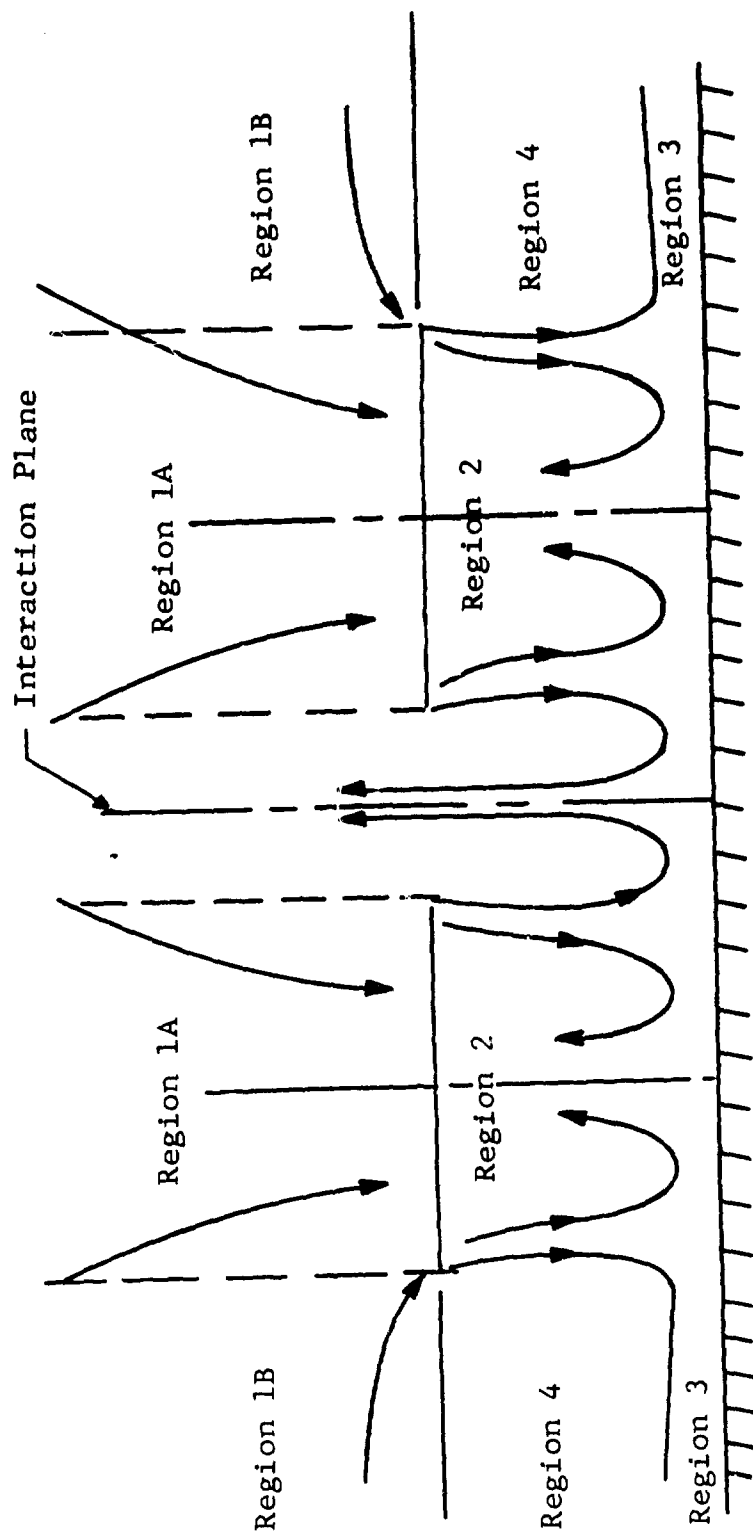


Figure 2. Definition of the Flow Regions in the Vicinity of Mutually Interacting Propellers/Rotors.



# 1. The Flow Field Above the Rotor Plane (Region 1)

## a. Region 1A

The flow field in region (1A) pertains to the flow above the rotor plane and within the vortex cylinder (see Figure 2). It is assumed that within this region the interference of adjacent rotors is negligible; therefore, the flow field in this region can be treated as that of an isolated single rotor.

Thus, using the analytical methods of Reference 3, the following relationships are obtained for the axial and radial velocity components applicable to region (1A) of a two-rotor configuration:

$$\frac{U_z}{U_N} = \frac{3}{4} \left\{ \frac{r}{R} - \frac{(Z-H)}{R} \left[ \frac{1}{\sqrt{1 - \left( \frac{Z-H}{R} \right)^2}} - \ln \frac{\sqrt{1 - \left( \frac{Z-H}{R} \right)^2} + 1}{\frac{r}{R} - \sqrt{\left( \frac{r}{R} \right)^2 - \left( \frac{Z-H}{R} \right)^2}} \right] \right\} \quad (1)$$

$$\frac{r}{R} \frac{U_r}{U_N} = \frac{3}{4} \left\{ \frac{3}{4} \left( \frac{Z-H}{R} \right)^2 \ln \left| \frac{Z-H}{R} \right| - \frac{1}{2} \frac{r}{R^2} \left[ \frac{1}{\left( 1 - \left( \frac{Z-H}{R} \right)^2 \right)^{3/2}} \right. \right.$$

$$\left. - \frac{\left( \frac{Z-H}{R} \right)^2}{\sqrt{1 - \left( \frac{Z-H}{R} \right)^2} \left( 1 - \sqrt{1 - \left( \frac{Z-H}{R} \right)^2} \right)} \right\}$$

$$\begin{aligned}
&= 1 - \ln \left( 1 + \sqrt{1 + \left( \frac{Z-H}{R} \right)^2} \right) - \frac{3}{4} \frac{r}{R} \sqrt{\frac{r^2}{R^2} + \left( \frac{Z-H}{R} \right)^2} \\
&\quad - \left( \frac{1}{2} \frac{r^2}{R^2} + \frac{3}{4} \right) \ln \left( \frac{r}{R} + \sqrt{\left( \frac{r}{R} \right)^2 + \left( \frac{Z-H}{R} \right)^2} \right) \} \quad (2)
\end{aligned}$$

As can be seen from Reference 3, the preceding relationships, which yield a closed-form solution for the nonuniform velocity distribution in the vicinity and at the plane of a lifting rotor, correlate well with more complex computer solutions such as those presented in Reference 4.

b. Region 1B

This region pertains to the flow above the rotor plane and outside the vortex cylinder. For a two-propeller/rotor configuration the velocity field is obtained by considering two point sinks located at the centers of the two rotors. Thus, using the coordinate system of Figure 1, the velocity components in the X, Y, and Z directions of a two-propeller/rotor configuration are given by:

$$\frac{U_X}{U_N} = \frac{7}{24} \left\{ \frac{\frac{X-X_L}{R}}{\left[ \left( \frac{X-X_L}{R} \right)^2 + \left( \frac{Y-Y_L}{R} \right)^2 + \left( \frac{Z-H}{R} \right)^2 \right]^{3/2}} \right.$$

$$\left. \frac{\frac{X-X_L}{R}}{\left[ \left( \frac{X-X_L}{R} \right)^2 + \left( \frac{Y-Y_L}{R} \right)^2 + \left( \frac{Z-H}{R} \right)^2 \right]^{3/2}} \right\} \quad (3)$$

$$\frac{U_Y}{U_N} = - \frac{7}{24} \left\{ \frac{\frac{Y-Y_L}{R}}{\left[ \left( \frac{X-X_L}{R} \right)^2 + \left( \frac{Y-Y_L}{R} \right)^2 + \left( \frac{Z-H}{R} \right)^2 \right]^{3/2}} \right.$$

$$\left. \frac{\frac{Y-Y_L}{R}}{\left[ \left( \frac{X-X_L}{R} \right)^2 + \left( \frac{Y-Y_L}{R} \right)^2 + \left( \frac{Z-H}{R} \right)^2 \right]^{3/2}} \right\} \quad (4)$$

$$\frac{U_Z}{U_N} = - \frac{7}{24} \frac{Z-H}{R} \left\{ \frac{1}{\left[ \left( \frac{X-X_L}{R} \right)^2 + \left( \frac{Y-Y_L}{R} \right)^2 + \left( \frac{Z-H}{R} \right)^2 \right]^{3/2}} \right.$$

$$\left. \frac{1}{\left[ \left( \frac{X-X_L}{R} \right)^2 + \left( \frac{Y-Y_L}{R} \right)^2 + \left( \frac{Z-H}{R} \right)^2 \right]^{3/2}} \right\} \quad (5)$$

Because of the three-dimensional character of the flow field defined by equations (3), (4), and (5), the pictorial presentation of the streamlines is not convenient except for the two planes of symmetry, the X-Z and the Y-Z plane.

In the X-Z plane, equations (3), (4), and (5) yield:

$$\frac{U_Y}{U_N} = \frac{U_Z}{U_N} = 0 \quad (6)$$

and

$$\frac{U_X}{U_N} = -\frac{7}{24} \left\{ \frac{1}{\left(\frac{X-X_L}{R}\right)^2} + \frac{1}{\left(\frac{X+X_L}{R}\right)^2} \right\} \quad (7)$$

At the location corresponding approximately to the leading edge of the front rotor, i.e.,  $X/R = 2X_L/R$ , equation (7) reduces to:

$$\frac{U_X}{U_N} = -\frac{7}{24} \left[ \frac{1}{\left(\frac{X_L}{R}\right)^2} + \frac{1}{9\left(\frac{X_L}{R}\right)^2} \right] \quad (8)$$

The second term of equation (8) corresponds to the effect of one rotor on the longitudinal velocity component  $U_X$  of the other rotor. Hence, at this location the mutual interference effects between the two rotors amount to approximately 11 percent of the total induced velocity component ( $U_X$ ) due to an isolated rotor.

Figure 3 shows a comparison of the results obtainable by means of equation (5) with the results of the computerized analysis presented in Reference 4. Again, a good correlation between the two methods is indicated.

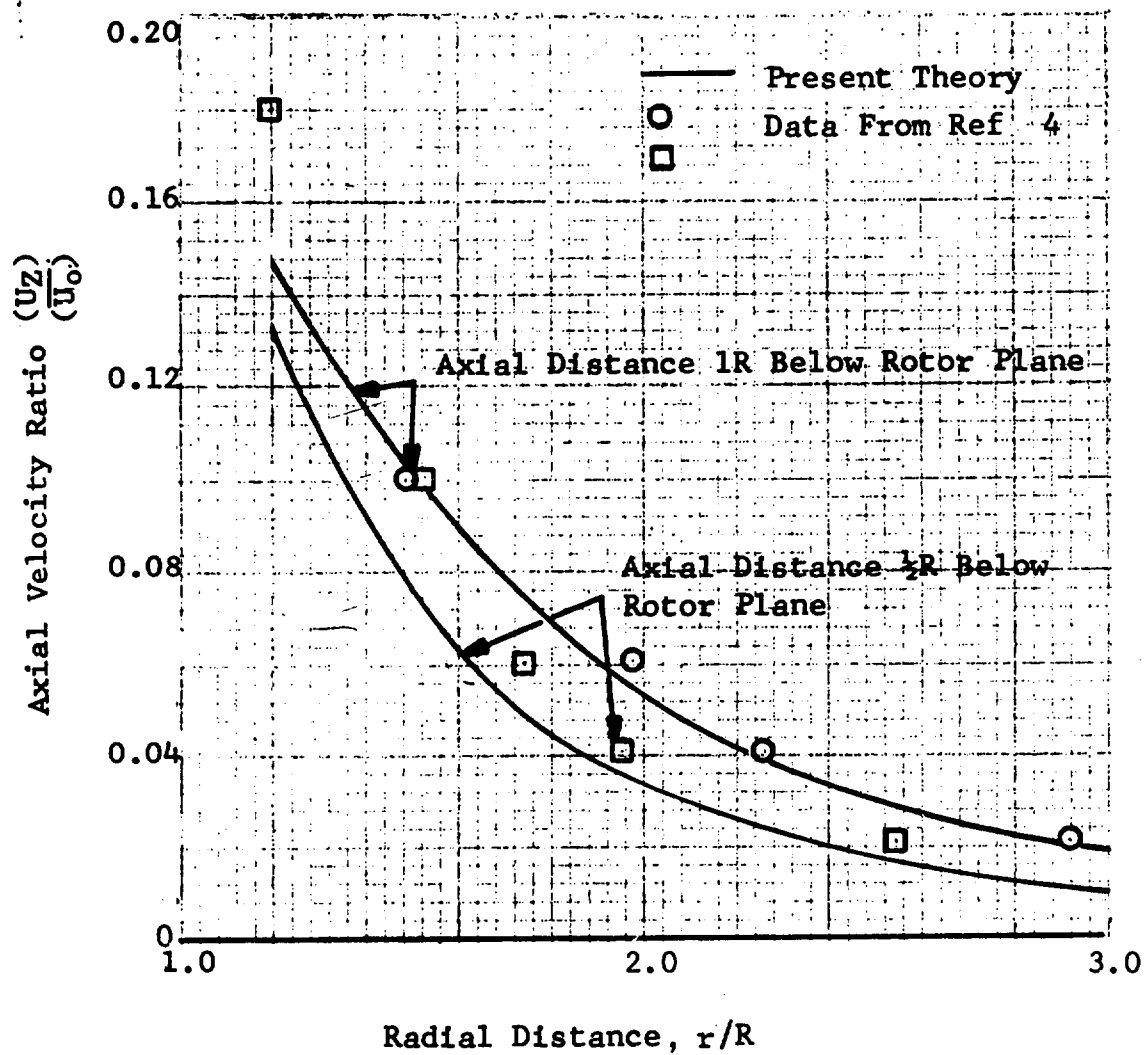


Figure 3. Variation of Axial Velocity Outside Vortex Cylinder Versus Radial Distance for Axial Distances of  $0.5R$  and  $1R$  Below the Rotor Plane.

The analysis for predicting the flow field of two mutually interacting rotors, for both inside and outside of the vortex cylinder (Region 1), applies only to out-of-ground-effect (OGE) conditions. A rotor operating in the proximity of the ground experiences a reduction in the induced velocity. This reduction can be accounted for by multiplying the out-of-ground-effect velocities by the ground correction factor,  $k_g$ . This factor is determined semiempirically as:

$$k_g = 1.0 - 0.9 e^{-2\left(\frac{H}{R}\right)} \quad (9)$$

Hence, the induced in-ground-effect ( $U_{IGE}$ ) can be expressed as follows:

$$U_{IGE} = k_g U_{OGE} \quad (10)$$

The ground effect factor,  $k_g$ , given in Figure 4 represents reasonably well the test data of Reference 5. The ground effect correction factor,  $k_g$ , given by equation (9) is plotted in Figure 4, where the test data of Reference 5 are superimposed. When this figure is examined, a good correlation can be noted between the semiempirically established  $k_g$  factor and that obtained from the test data.

Utilizing the preceding analysis, the flow field above the rotor plane (Region 1) was calculated; the non-dimensionalized results thus obtained are presented in Figure 5 for out-of-ground-effect conditions ( $H/R > 2.0$ ). For in-ground-effect operating conditions and any rotor height  $H/R \leq 2.0$  above the ground, the velocity at any point in Region 1 was determined by multiplying the velocity ratio obtained from Figure 5 by the momentum slipstream velocity ( $U_0$ ) and the appropriate  $k_g$  factor obtained from Figure 4.

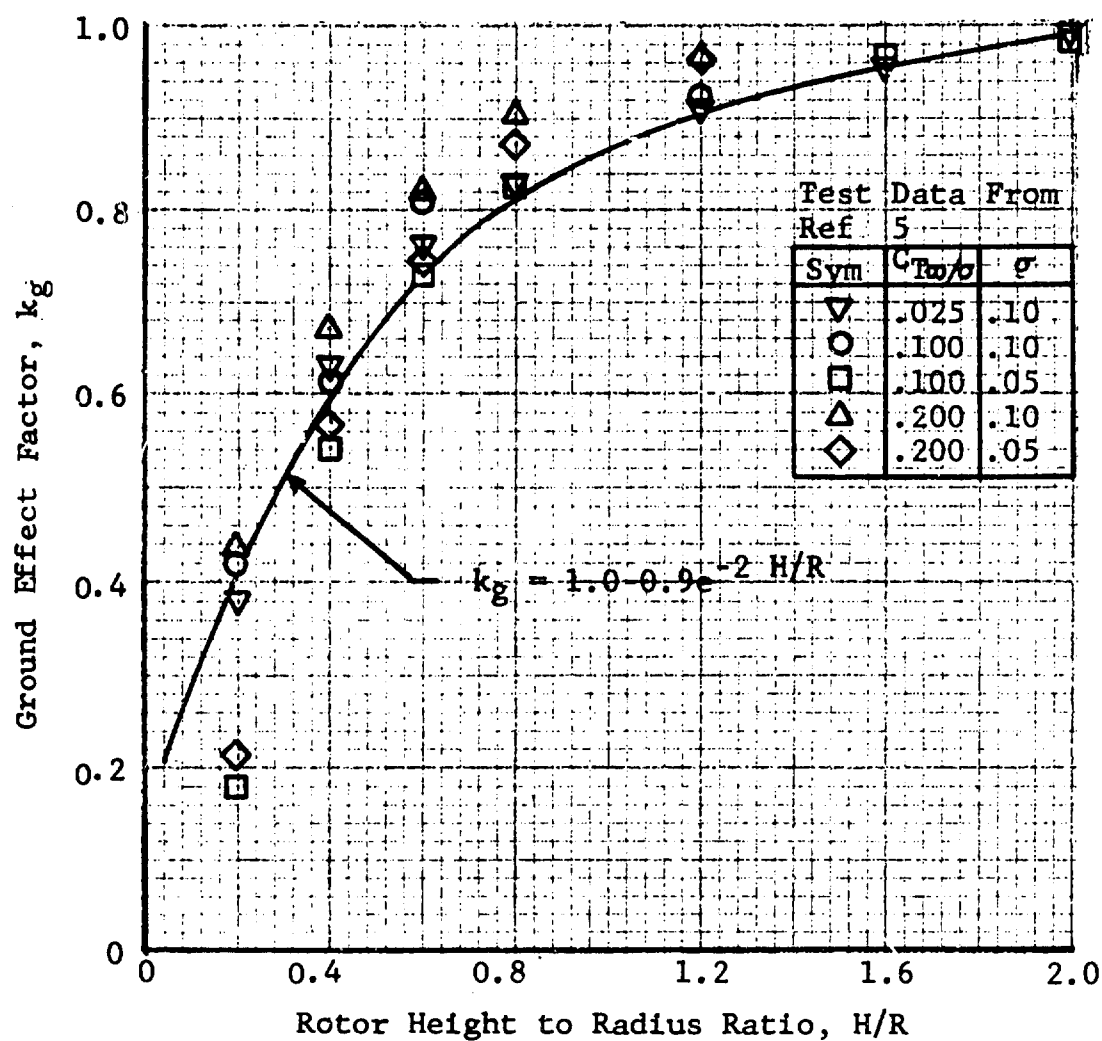


Figure 4. Effect of Thrust Coefficient and Solidity on the Ground Effect Inflow Correction Factor in Hovering.

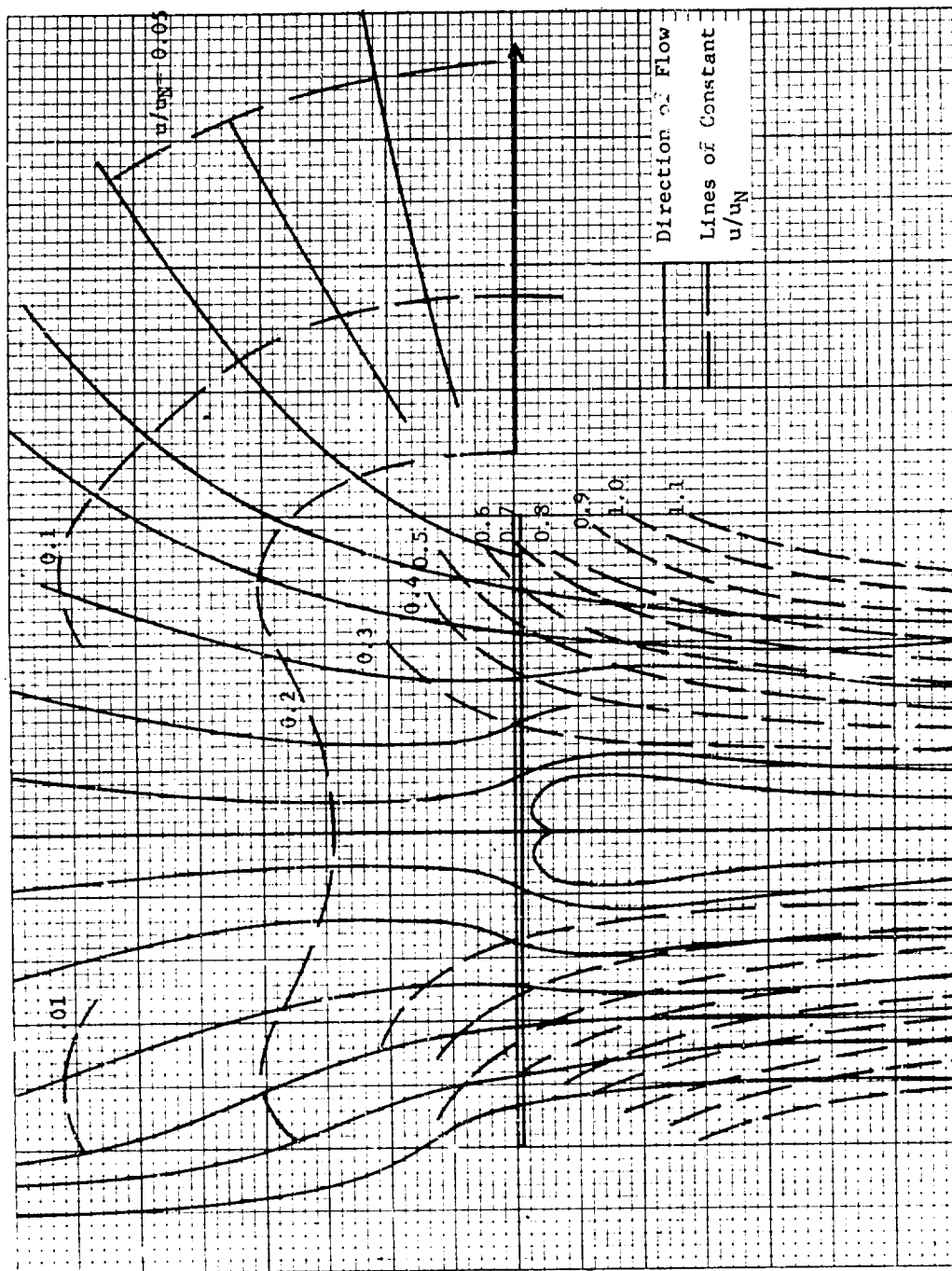


Figure 5. Flow Field in the Vicinity of a Hovering Rotor, Out of Ground Effect.



## 2. Flow Field Below the Rotor (Region 2)

Region 2 pertains to the flow field below the rotor plane and within the vortex cylinder (see Figure 2). For out-of-ground-effect conditions, this region may also be treated analytically by use of the same method used for Region 1A. In ground effect, however, these analyses are considered to be invalid. Therefore, in order to determine the flow field in this region, experimental data are herein utilized instead. Such data, though limited in quantity, are presented in Reference 2. This reference contains axial velocity profiles for rotor height of  $H/D = 0.5$ , and the smoke flow visualization data for other rotor heights. These data were utilized to construct velocity contours for other rotor heights using the superposition method of Reference 6.

Figure 6 shows the velocity distribution (contour plots) below the rotor (Region 2) for rotor heights of  $H/R = 1, .5$ , and  $.656$ . This figure can be used to obtain velocity contour plots immediately below the rotor or propeller plane of a VTOL aircraft operating at these heights to radius ratios. It should be noted that although the data presented in Figure 6 specifically apply to straight untwisted rotor blades, they are considered to be adequate for the analysis of the conventional rotor designs with moderate blade twist. For the case of high efflux jets or fans, a uniform velocity distribution at the jet exit may be assumed with the velocity reduced by  $k_g$  as in Region 1.

## 3. Flow Field in the Wall Jet (Region 3)

Region 3, as shown in Figure 2, pertains to the flow along the ground (outside the vortex cylinder) known as the wall jet region.

The behavior of flow along the ground is described in Reference 7. The radial velocity is zero at the rotor axis and increases linearly to a maximum value at a radial distance ( $r/D_e$ ) approximately equal to 1.0. Then it decreases exponentially as the radial distance increases. The point at which the radial velocity along the ground is maximum (which also corresponds to the point where the pressure is atmospheric) is defined as the beginning of the

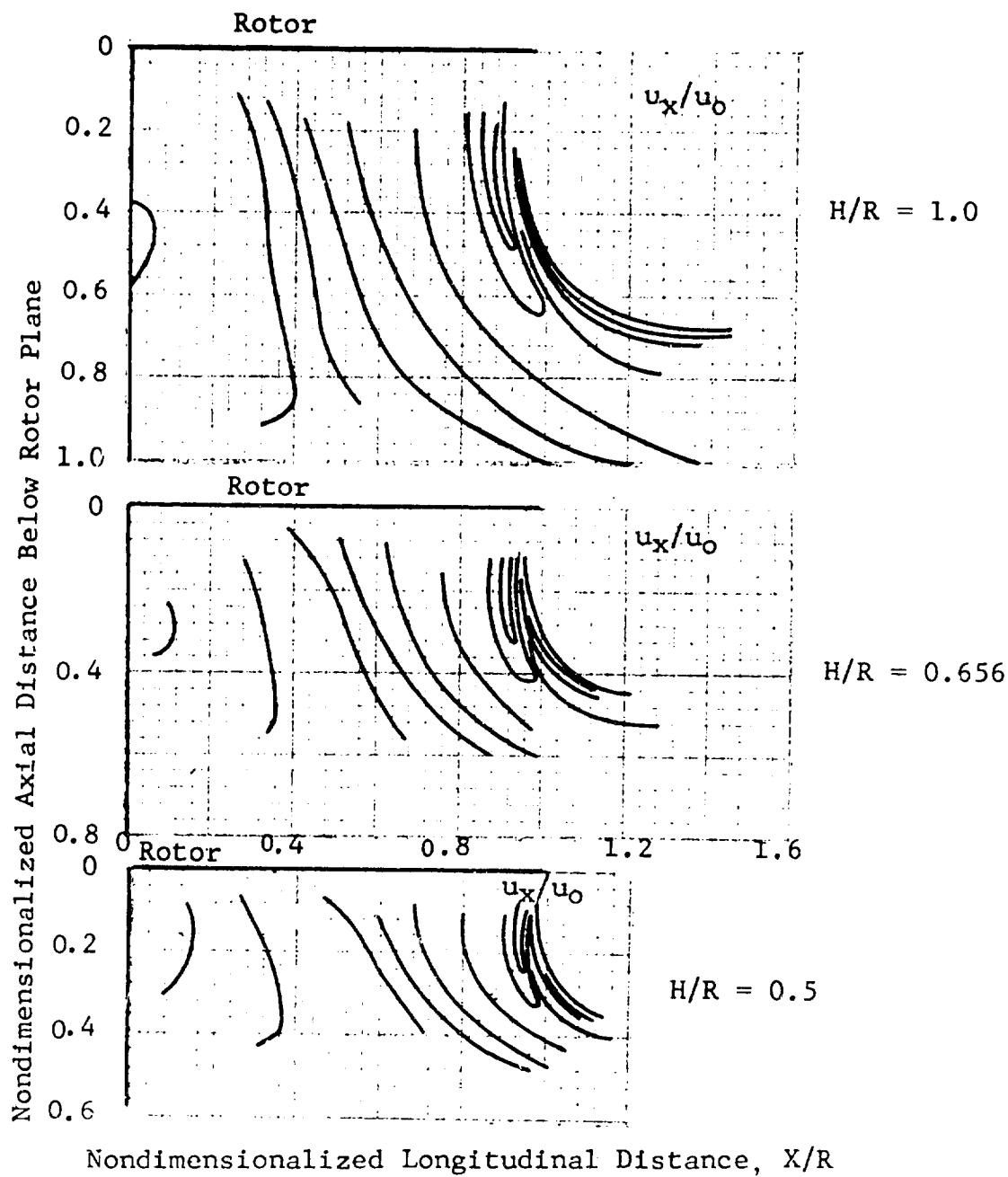


Figure 6. Downwash Velocity Distribution Below the Rotor in Ground Effect (Region 2).

wall jet. Thus, the wall jet (Region 3) extends radially from there.

Reference 8 shows that the velocity profiles at any radial station along the ground within the wall jet region are affine. The wall jet velocity profile reproduced from Reference 8 and confirmed by experimental data of Reference 7 is herein presented in Figure 7. This figure shows a distribution of the velocity ratio  $u/u_m$  as a function of vertical distance ratio  $(y/y_1)$  within the wall jet.

Reference 7 also presents an analytical treatment of the flow in the wall jet region. This analysis, however, utilizes a free jet decay which is not representative of the air jet induced velocity produced by a rotor. Therefore, to obtain the decay of the dynamic pressure ( $q_{s_{max}}/q_m$ ) for a rotor, the data of Reference 9 presented herein as a plot of  $q_{s_{max}}/q_m$  in Figure 8 are applied to the present analysis. As indicated in Reference 7, the maximum radial velocity in the wall jet ( $u_m$ ) at any radial station ( $r$ ) can be expressed as follows:

$$\frac{u_m}{U_H} = C_u \left( \frac{r}{R} \right)^{-1.143} \quad (11)$$

Also, the distance above the ground where the velocity equals half of the maximum velocity is given by:

$$\frac{y_1}{R} = C_y \left( \frac{r}{R} \right)^{1.028} \quad (12)$$

The wall jet constants  $C_u$  and  $C_y$  can be expressed as functions of the parameters  $(u_m/U_H)_c$ ,  $(y_1/R)_c$ , and  $(r/R)_c$  at the beginning of the wall jet as follows:

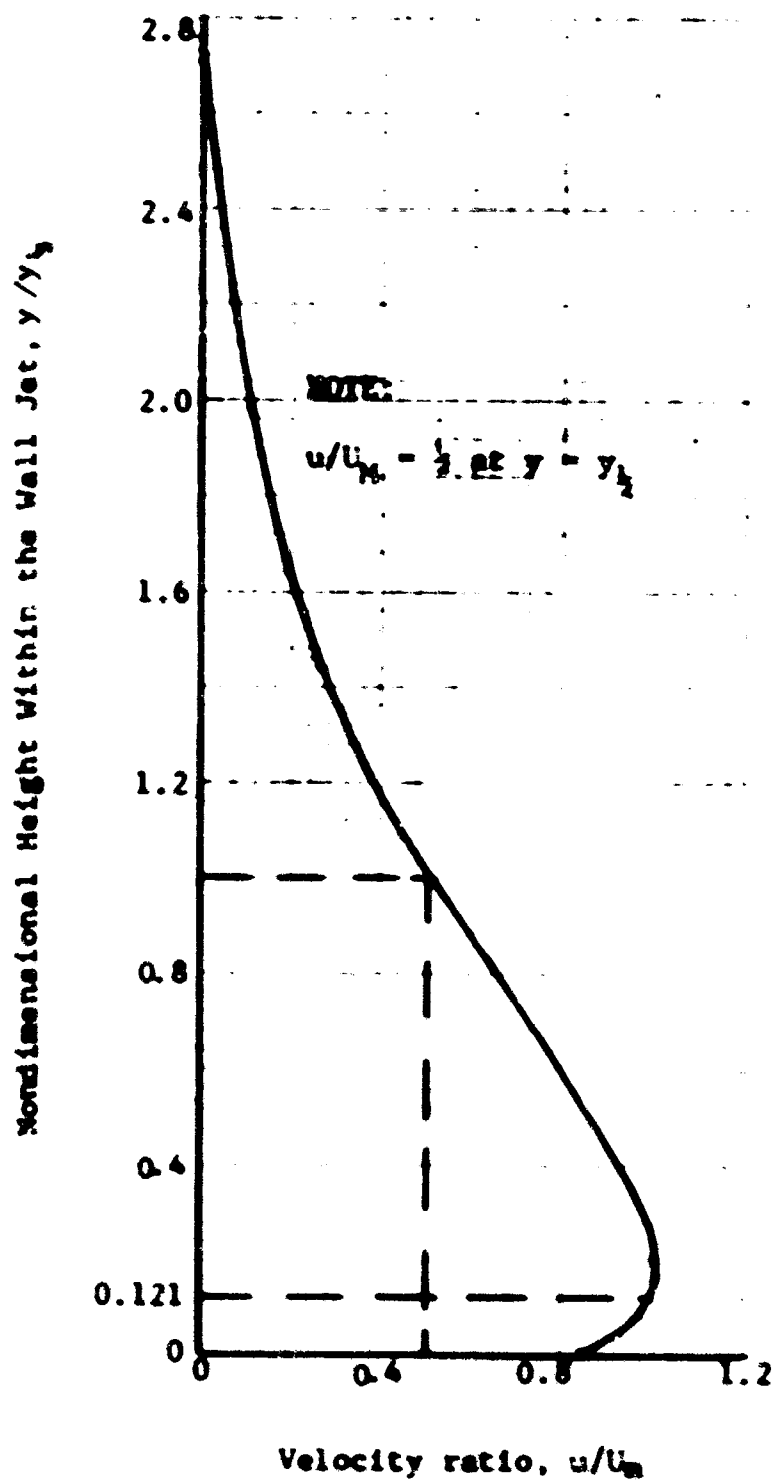


Figure 7. The Wall Jet Velocity Profile.

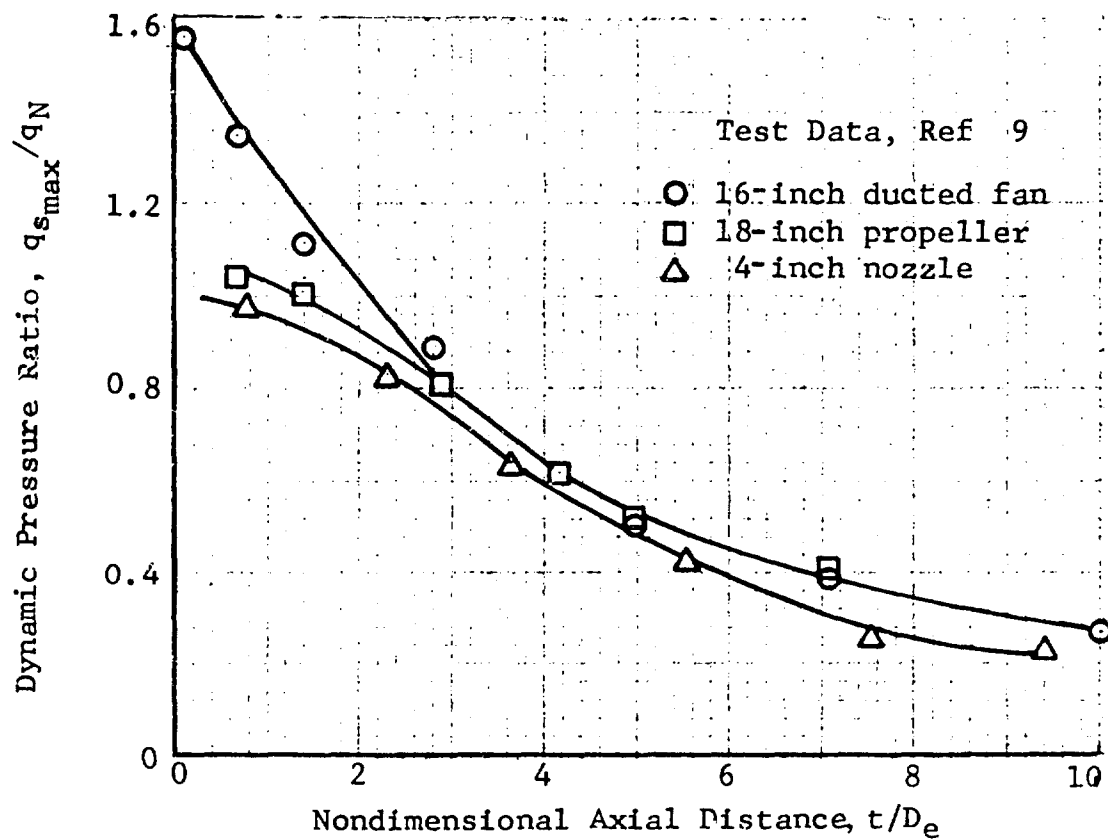


Figure 8. Test Data on the Decay of Dynamic Pressure With Axial Distance From the Jet Exit.

$$C_u = \left( \frac{u_m}{U_M} \right)_t \left( \frac{r}{R} \right)_t^{1.143} \quad (13)$$

$$C_y = \left( \frac{y_1}{R} \right)_t \left( \frac{r}{R} \right)_t^{-1.028} \quad (14)$$

The parameter  $(y_1/R)_t$  can be expressed as follows:

$$\left( \frac{y_1}{R} \right)_t = \frac{0.654}{\left( \frac{u_m}{U_M} \right)_t \left( \frac{r}{R} \right)_t} \quad (15)$$

In order to establish the wall jet constants  $C_u$ ,  $C_y$ , and  $(y_1/R)_t$  as given by equations (13) through (15), it is first necessary to determine the position of the beginning of the wall jet  $(r/R)_t$  and the maximum velocity ratio  $(u_m/U_M)_t$  at the wall jet.

This can be accomplished by utilizing the iterative procedure of Reference 7 as follows:

- (a) Determine rotor height above the ground  $(H/R)$  and assume an initial value of  $(r/R)_t \approx 2.0$ .
- (b) Calculate an equivalent free jet distance  $t/R$  using the following relationship:

$$\frac{t}{H} = \frac{H}{R} + \left[ \left( \frac{r}{R} \right)_t - 1.0 \right] \quad (16)$$

- (c) Transform the value of  $t/R$  into  $T/D_e$  which for open rotors is given by:

$$\frac{t}{D_e} = 0.707 \frac{t}{R} \quad (17)$$

- (d) Using the value of  $(t/D_e)$  from step (c), obtain the ratio of  $(q_{s_{\max}}/q_N)$  from the test data of Figure 8. Then compute

$$\frac{u_m}{U_N} = \sqrt{\frac{q_{s_{\max}}}{q_N}} \quad (18)$$

where  $U_N$  is the induced velocity of a fully developed slipstream, and for an open rotor  $U_N$  can be expressed as follows:

$$U_N = \sqrt{\frac{2 DL}{\rho}} \quad (19)$$

- (e) Obtain the value of the average induced velocity at the rotor disc in ground effect ( $\bar{U}$ ) by using  $U_N$  from step (d) and the appropriate value of the ground effect factor  $k_g$  from Figure 4:

$$\bar{U} = k_g (U_o)_{\text{OGE}} = k_g \frac{U_N}{2} \quad (20)$$

where  $(U_o)_{\text{OGE}}$  is the average induced velocity at the rotor plane out of ground effect.

- (f) Compute the radial position at which the wall jet begins:

$$\left( \frac{r}{R} \right) = \frac{(1.45)^{0.486}}{(0.52)^{1.13}} \left( \frac{\bar{U}}{u_m} \right)^{0.486} \quad (21)$$

- (g) Repeat steps (b) through (f) until convergence is obtained for the value of the position where the wall jet begins,  $(r/R)_t$ .
- (h) Using the final value of  $(r/R)_t$  from step (g),  $\bar{U}$  from step (e), and  $u_m$  from step (d), calculate  $\bar{U}_H$  using the following relationship:

$$\bar{U}_H = \left[ 0.385 \left( \frac{r}{R} \right)_t^{0.885} u_m \bar{U}^{0.14} \right]^{0.88} \quad (22)$$

- (i) Using the values of  $u_m$  from step (d),  $(r/R)_t$  from step (g), and  $\bar{U}_H$  from step (h), calculate  $(y_1/R)_t$  using equation (15).
- (j) Finally, compute the wall jet constants  $C_u$  and  $C$  by using equations (13) and (14), respectively.

#### 4. Flow Within the Recirculation Region

Region 4, as shown in Figure 2, pertains to the flow field between the wall jet boundary and the plane of the rotor outside the vortex cylinder. The wall jet boundary is herein defined as the height at which the local velocity is equal to 1% of the maximum ground surface velocity (i.e.,  $u = 0.01 u_{max}$ ).



The outward radial flow in the wall jet interacts with the inward flow induced by the rotor, and a recirculatory flow in this region results. This flow phenomenon is clearly defined in the experimental work of References 2, 10, and 11. The analytical treatment of the flow in this region is extremely difficult, and no theoretical solutions are available in the existing literature. Some qualitative experimental data pertaining to the flow field in this region are presented in Reference 11 and in Figure 9. These data, however, are not adequate for the application in the present program. Due to shear flow interaction effects and small magnitudes of the velocities in this region, quantitative experimental data are practically nonexistent.

Hence, in the present approach, the analysis of the flow in this region utilizes a number of simplifying assumptions, the validity of which must be determined experimentally.

As defined previously, the external flow along the upper boundary of the wall jet ( $u = 0.01 u_{\max}$ ) is practically stationary; i.e., the axial and radial velocity components are considered to be zero.

Furthermore, it is herein postulated that the assumptions inherent in equation (10) will also apply to the recirculation region, provided that the required boundary conditions at the wall jet and at the plane of rotor disc are satisfied. One way to achieve this is to multiply equation (10) by a correction factor  $F_h$  which varies linearly from  $F_h = 1.0$  at the plane of rotor disc to  $F_h = 0$  at the boundary of the wall jet.

Thus, equation (10) becomes

$$U_{IGE} = k_g U_{OGE} F_h \quad (23)$$

Using Figure 10, the correction factor  $F_h$  can be obtained as follows:

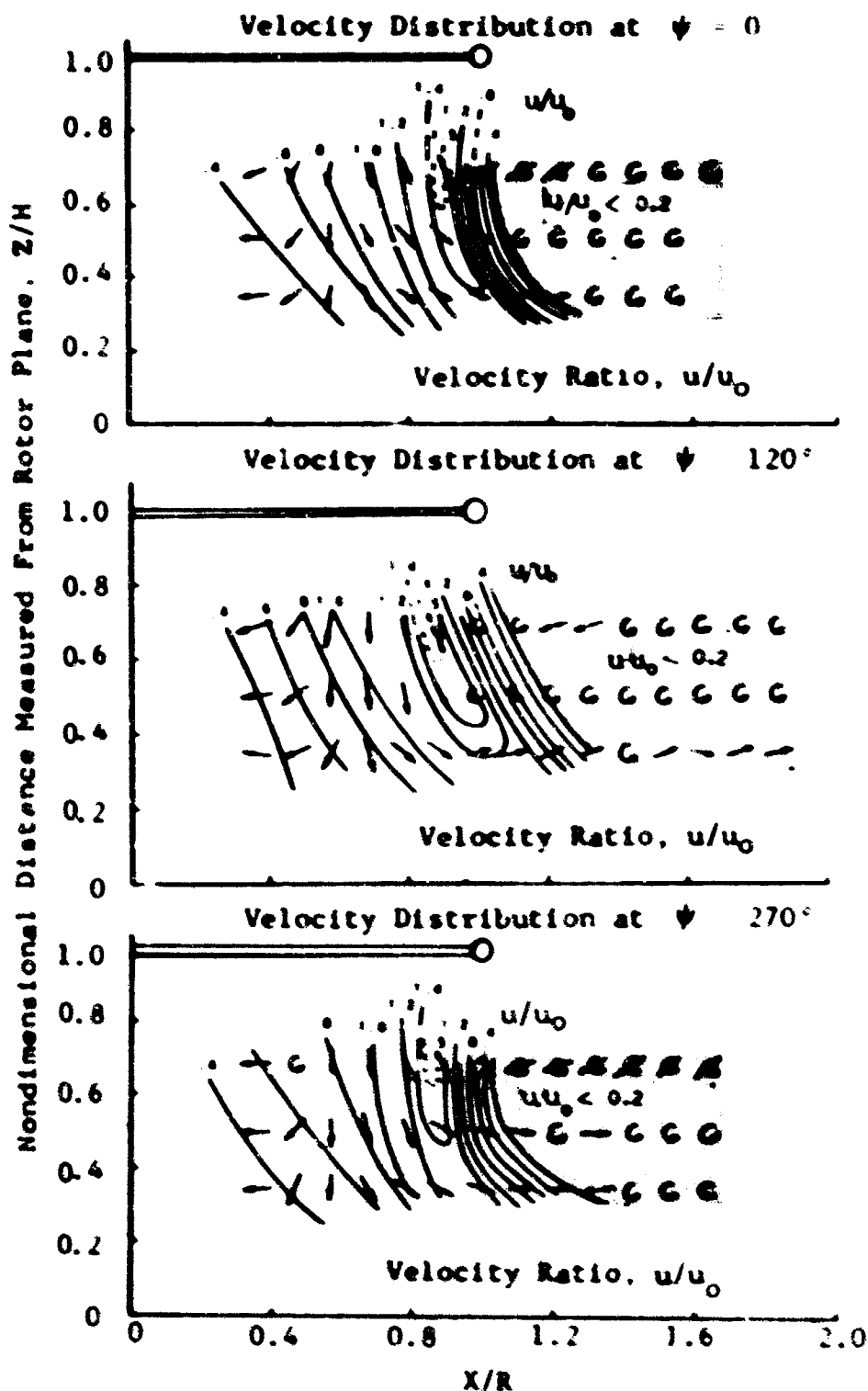
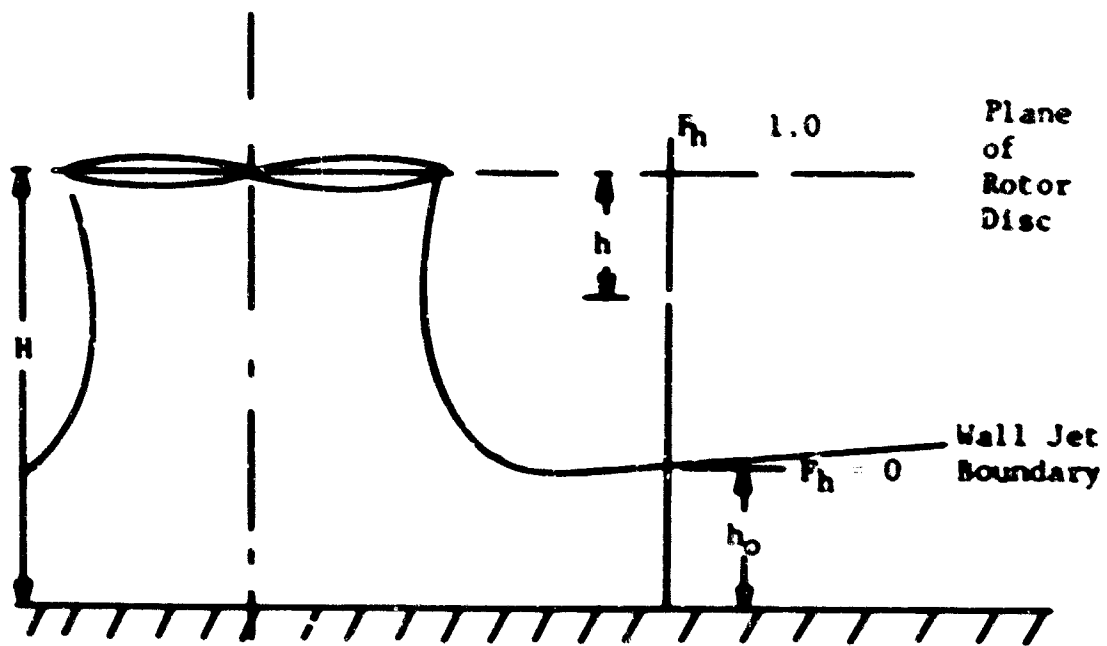
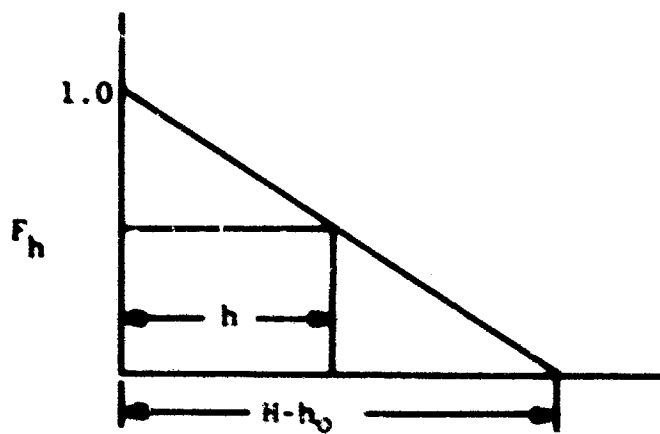


Figure 9. Downwash Velocity in Ground Effect for a 75-Foot Rotor at  $H/R = 0.44$ .



(a)



(b)

Figure 10. Schematic Representation of the Flow Field in the Recirculation Region.

$$F_h = \frac{H-h_0-h}{h-h_0} \quad (24)$$

Substituting equation (24) into equation (23), the induced velocity in the recirculation region at any radial station  $r$  and at any vertical location ( $h$ ) below the rotor disc plane can be expressed as follows:

$$U_{IGE} = k_g U_{OGE} \left( 1 - \frac{h}{H-h_0} \right) \quad (25)$$

##### 5. Flow in the Interaction Plane (Region 5)

The flow in Region 5, as shown in Figure 2, pertains to the flow in the interaction plane where the downwash from the two rotor/propellers meet. Along this plane, the downwash velocities from the two lift devices interact with each other, and the resultant flow is turned upward. For side-by-side rotor/propeller configurations, this upward flow is restrained by the fuselage and is diverted horizontally along the longitudinal axis of the aircraft. For tandem configurations with no rotor overlap, the interaction plane is along the lateral axis of the aircraft; hence, there is a minimum fuselage restraint, and practically all of the resultant flow will be turned vertically upward.

Conceptually, the interaction plane can be considered as a thin vertical wall (no flow through the wall) at which the radial flow along the ground from each rotor is deflected along the vertical plane at the same angle as if the ground flow continued (see Figure 11). Thus, the dynamic pressure (or the corresponding velocity) at a point in the interaction plane can be considered to be the same as if the flow from the single rotor continued along the ground at the same total distance from the rotor axis.

The test data of Reference 12 show that the resultant velocities along the interaction plane due to two rotors are greater than those for an isolated rotor at the same total

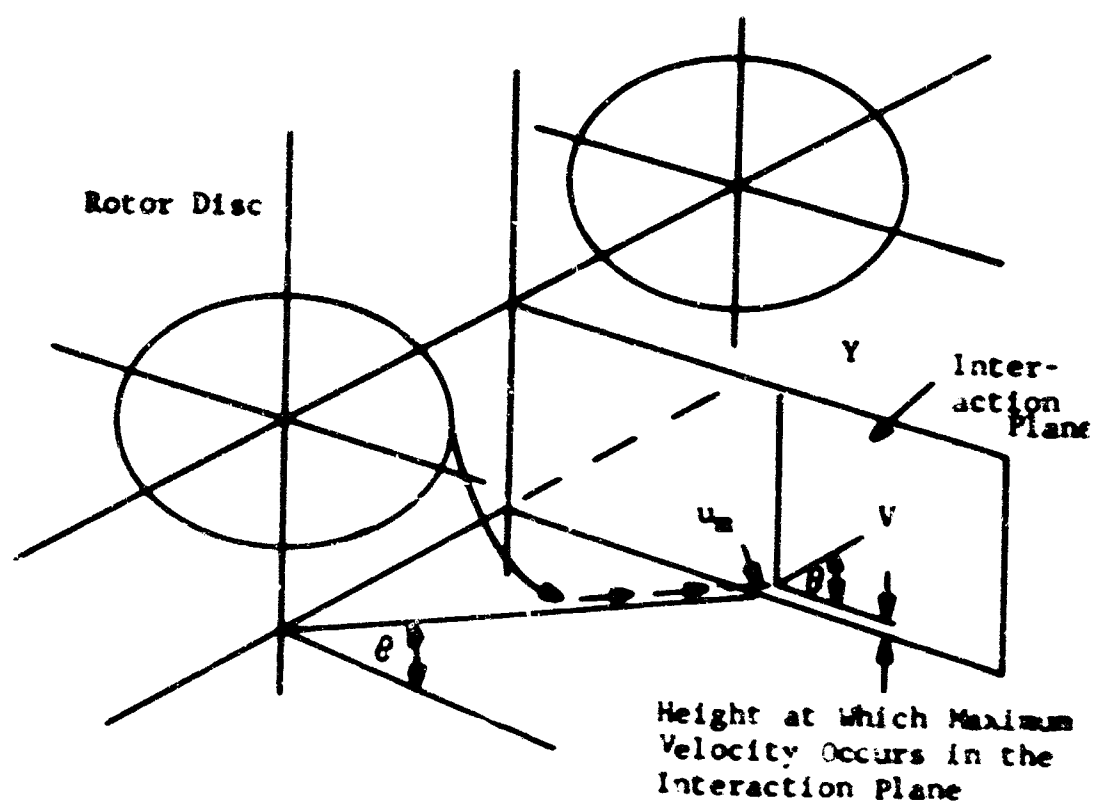


Figure 11. Schematic Representation of the Flow Field Along the Interaction Flow.

radial distance. These data have been utilized to develop a velocity interference correction factor,  $T_f$ , which is presented as a function of a total radial distance from a single rotor in Figure 12.

Using the nomenclature of Figure 13, the horizontal and vertical velocity components  $V_H$  and  $V_V$  can be expressed as follows:

$$V_H = T_f u_m (X/R) \quad (26)$$

$$V_V = T_f u_m (Y-Z)/R \quad (27)$$

## B. DOWNWASH SIGNATURES

### 1. Dust Cloud Size and Shape

As discussed previously, the impingement of rotor downwash on the ground results in a high-velocity flow along the ground and the subsequent erosion and entrainment of ground particles. These particles, once eroded, are transported aloft by the flow field generated by the hovering aircraft and thus form a dust cloud. References 9 and 13 indicate that the particle erosion upon a specific terrain is a function of the maximum dynamic pressure ( $q_{s,max}$ ) on the ground and the terrain erosion factor ( $k_t$ ) which is dependent on the terrain characteristics.

As noted in Reference 9, the parameter which governs the particle terrain erosion is related to the effective surface dynamic pressure which can be expressed as follows:

$$(q_s)_{eff} = \frac{(q_s)_{max}}{\sqrt{k_t}} \quad (28)$$

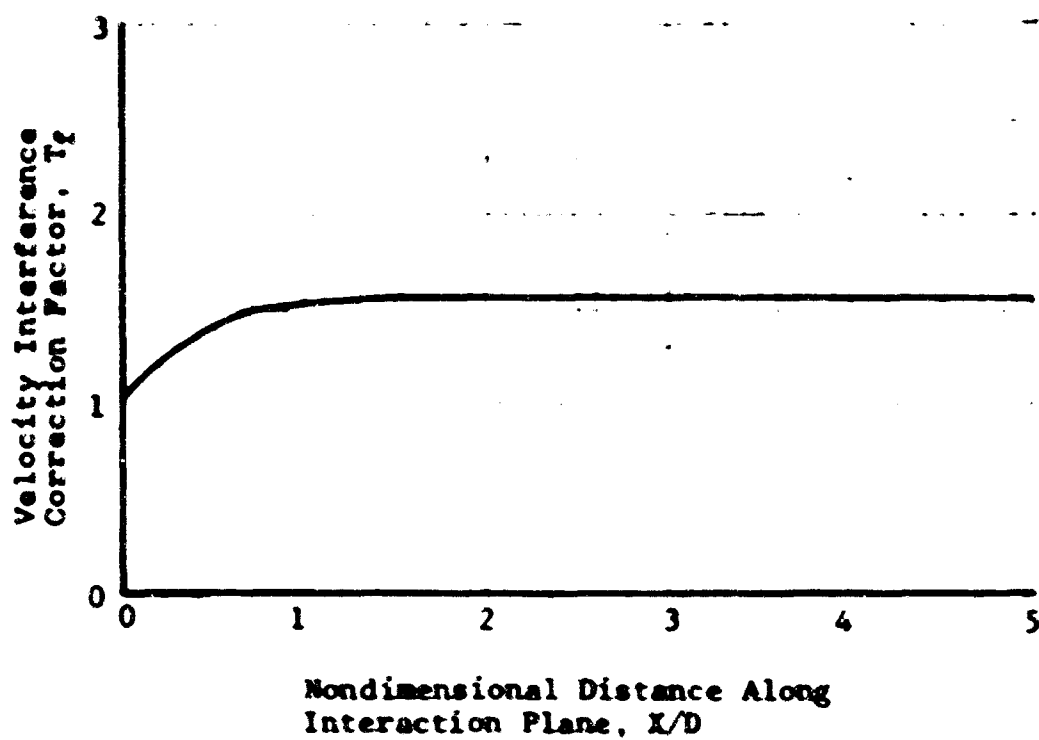


Figure 12. Correction Factor For Determining Velocities Within the Interaction Plane.

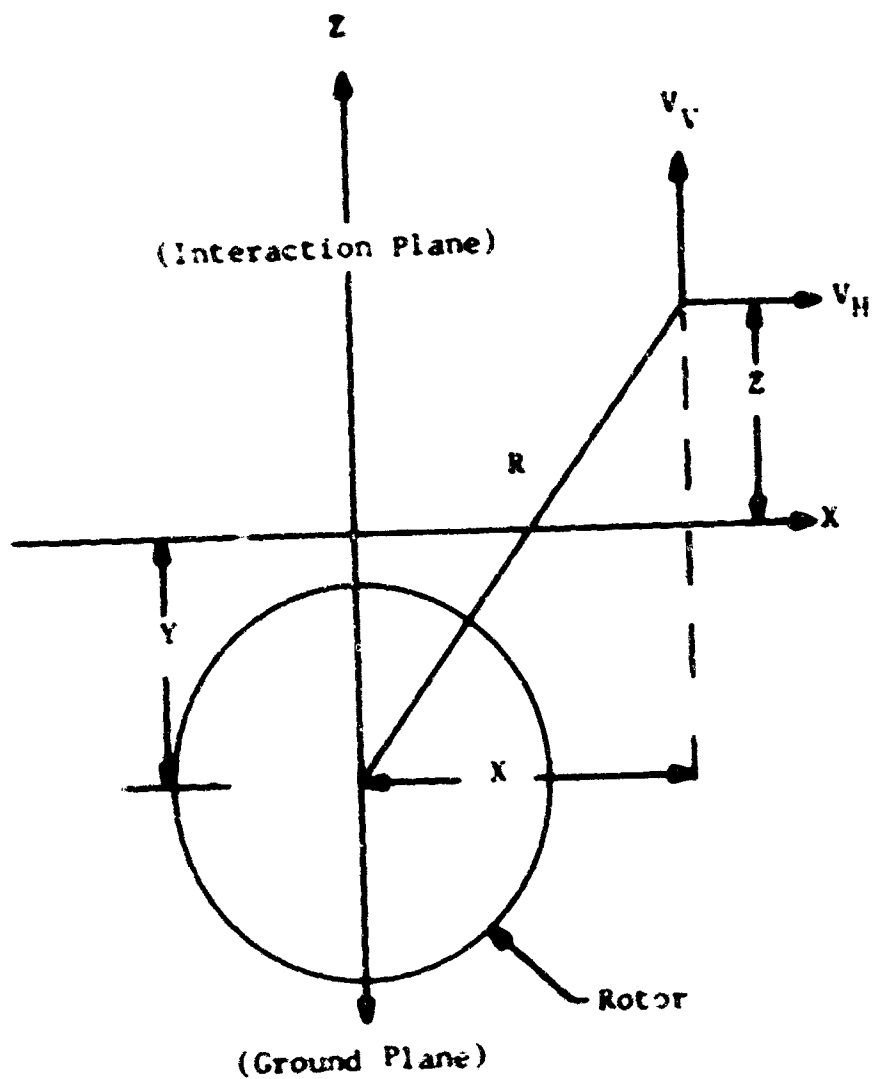


Figure 13. Definition of Parameters Within the Interaction Plane.



The terrain erosion factor,  $k_t$ , is given by:

$$k_t = \frac{\bar{D}_p \rho_p}{D_{pw} \rho_{pw}} \quad (29)$$

This terrain factor relates the terrain characteristics, i.e., terrain density and mean particle size, with water droplet size and density. Water droplet size was obtained from Reference 14.

From the film data, which were obtained by the Mine Safety Research Corporation as a part of the test program reported in Reference 15, it is determined that the dust cloud radial boundary can be approximated by the radial distance along the ground at which the surface effective dynamic pressure is approximately equal to 1.0 (i.e.,  $(q_s)_{eff} = 1.0$ ). Thus, the radial location of the dust cloud boundary can be readily obtained from equation (28) using the wall jet and the interaction plane analyses presented in Section II. A. The resulting dust cloud radius (boundary) can be expressed as follows:

$$R_c = R \left[ \frac{\sqrt{k_t}}{C_1 \rho U_m^2 C_u^2} \right]^{-.437} \quad (30)$$

where  $C_1 = 0.5$  for regions outside the interaction plane and  $C_1 = 1.1$  along the interaction plane.

The height of the dust cloud (maximum vertical location of the cloud boundary) can be approximated by considering the path of the rotor blade tip vortices as they spread along the ground. The ground spreading of the rotor blade tip vortices is believed to be the primary cause for the cloud roll-up observed from the film data.

A detailed analysis of the behavior of this vortex system along the ground can be made by replacing the continuous cylindrical vortex sheet with a finite number of discrete wing vortices. A step-by-step iteration procedure could then be applied to compute the motion of each ring vortex as it starts to expand along the ground. However, in lieu of this process, which is complicated, time consuming, and would require a computer solution, an attempt was made to analyze the roll-up process utilizing an analogy of the vortex sheet shed from the trailing edge of a lifting wing as schematically shown in Figure 14.

It can be seen that the vortex pattern behind the lifting wing (Figure 14(b)) exhibits a flow mechanism very similar to that shown along Section A-A (Figure 14(a)) of the ring vortex sheet generated by a lifting rotor. The main difference between the flow mechanism of the cylindrical vortex sheet of a rotor and the vortex sheet of a lifting wing is that the former rolls up and forms a torus ring while the latter rolls up into two line vortices.

Using the above analogy, conventional wing vortex theory such as that presented in Reference 16 is applied to predict the center of the vortex core. Using the nomenclature of Figure 14(a), the coordinates of the center of the vortex core for complete roll-up can be expressed as follows:

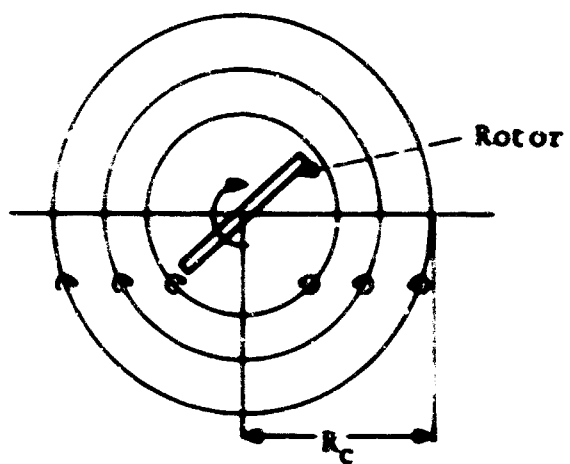
$$R_V = 0.785 R_C \quad (31)$$

$$Z_V = 0.329 R_C \quad (32)$$

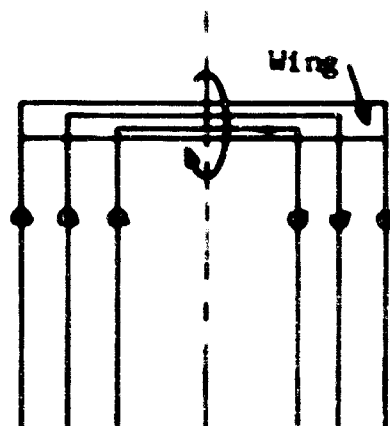
Once the center of the core is defined, the cloud roll-up is approximated by a logarithmic spiral relationship given by:

$$R = e^{a(\phi - \phi_0)} \quad (33)$$

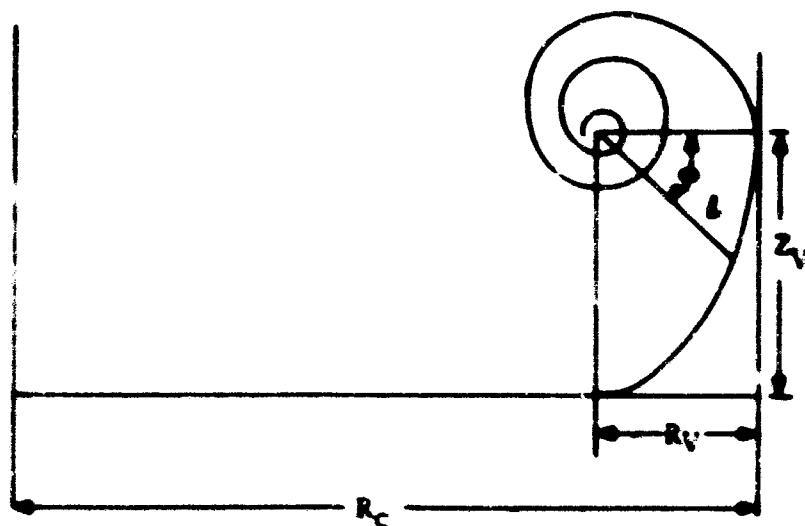
where  $a$  and  $\phi_0$  are constants which can be determined by applying the boundary conditions of  $\phi = 0$  when  $R = R_C = R_V$



(a) Lifting Rotor Vortex Pattern



(b) Lifting Wing Vortex Pattern



(c) Logarithmic Spiral Representation of Vortex Roll-Up

Figure 14. Schematic Representation of a Lifting Rotor Vortex System in Ground Effect.

and  $\phi = \pi/2$  when  $L = Z_V$ . Applying these boundary conditions to equation (33), there results:

$$a = \frac{Z_V}{\pi} \log \left( \frac{Z_V}{R_C - R_V} \right) \quad (34)$$

$$\phi_0 = \pi \log \left( \frac{R_C - R_V}{Z_V} \right) \quad (35)$$

Thus, knowing the radial location of the dust cloud boundary ( $R_C$ ) and the constants  $a$  and  $\phi_0$ , the vertical location of the dust cloud boundary measured from the center of the vortex spiral can be computed by substituting  $\phi = \pi/2$  in equation (33). Thus,

$$L_V = e^{a(-\frac{\pi}{2} - \phi_0)} \quad (36)$$

The total dust cloud height measured from the ground is then given by:

$$H_C = L_V + Z_V \quad (37)$$

## 2. Cloud Content

### a. Particle Density Distribution

#### (1) Far Field Density Distribution

In the far field flow region of VTOL aircraft (i.e., the region from the start of the wall jet to the boundary of the cloud), the particle density distribution within the cloud is derived based on the analysis presented in Reference 17.

By assuming particle characteristic paths and by considering the rate of loss of momentum of the air due to particle movement, a semi-empirical expression is derived in this reference which gives the particle mass flow rate along a lane of unit width for the case of constant wind blown over desert sand. This expression is given as:

$$q_s = C_2 \rho V_*^3 \sqrt{\frac{D_{P*}}{D_S}} \quad (38)$$

where the constant  $C_2$  was found experimentally to be  $C_2 = 1.5$  for nearly uniform sand,  $C_2 = 1.8$  for naturally graded sand, and  $C_2 = 2.8$  for sand with a wide range of grain size. The parameter  $V_*$  is given by:

$$V_* = \sqrt{\frac{\tau}{\rho}} \quad (39)$$

Reference 17 defines  $(\tau)$  as shearing force or drag per square cm of ground surface parallel to the wind direction. Also,  $V_*$ , which is merely a mathematical symbol, is defined as the drag velocity which is directly proportional to the rate of increase of the wind velocity with the log-height. Since the velocity and the log-height have a straight line relationship,  $V_*$  is proportional to the tangent of the angle which this straight line or velocity ray makes with the height ordinate. The proportionality constant is determined experimentally to be 5.75. Furthermore, Reference 17 shows that if the wind velocity close to the surface is plotted against the log-height, the zero wind

velocity occurs at a certain small but definite height above the ground surface. This height is found to be associated with the size of the irregularities which constitute the surface roughness and is approximately equal to  $1/30$  the diameter of the grain size on the surface.

In utilizing the results of Reference 17, it is now necessary to relate the mathematical parameter  $V_*$  to the parameters in the boundary layer of the rotor wall jet flow. For this purpose the boundary layer thickness ( $y_m$ ) in the wall jet flow is herein defined as the vertical distance at which the wall jet velocity is a maximum.

Although the velocity in the rotor wall jet flow is nonuniform (see Figure 7) as compared to the uniform (constant) ambient wind velocity assumed in Reference 17, it is believed that the flow in the boundary layer will be analogous for both types of flow. Therefore, the drag velocity  $V_*$  within the boundary layer of the wall jet flow can be expressed as follows:

$$V_* = \frac{u_m}{5.75 \log \left( \frac{30 y_m}{D_{p*}} \right)} \quad (40)$$

where  $y_m$ , the boundary layer thickness in the wall jet, is obtained from Figure 7 as

$$\frac{y_m}{y_b} = 0.121 \quad (41)$$

The particle mass flow rate,  $m$ , per unit width can now be obtained by substituting equation (40) into equation (38):

$$\pi_z = C_2 \rho \left[ \frac{u_g}{5.75 \log \left( \frac{30 y_m}{D_{p*}} \right)} \right]^3 \sqrt{\frac{D_{p*}}{D_S}} \quad (42)$$

Also, examining the test data of Reference 14, it can be noted that the particle mass flow rate  $\pi$  (lb/sec-ft<sup>2</sup>), when plotted on a log scale versus height (Z), exhibits linear relationship with height. Furthermore, the integrated value of  $\pi$  with respect to Z yields the particle mass flow per unit width:

$$\pi_w = \int_0^{H_c} \pi \, dZ \quad (43)$$

Using equation (43), the particle mass flow rate per unit area  $\pi_0$  (lb/sec-ft<sup>2</sup>) along the ground can now be expressed in terms of the particle mass flow rate per unit width  $\pi_w$  (lb/sec-ft) as follows:

$$\pi_0 = 10^{-K} + 2.3 \frac{\pi_w}{H_c} (K - \log \pi_0) \quad (44)$$

where K is a positive integer chosen such that  $\pi \approx 0$  when  $\pi_0 \leq 10^{-K}$ .

In performing graphical solutions of equation (44), it was determined that a value of  $K \geq 6$  did not affect the numerical values of  $\pi_0$ .

Therefore, the value of  $K = 6$  was utilized in the subsequent analysis. The parameter  $10^{-K}$  represents the particle mass flow rate at the boundary of the cloud ( $H_c$ ). In previous theoretical analyses of the cloud constant, that value was assumed to be zero. However, from actual observation of the cloud patterns, it is inferred that certain small particle mass flow will exist even at the cloud boundary. It is therefore believed that the representation of this small mass flow rate by a factor of  $10^{-K}$  is more realistic than the assumption of  $m = 0$  at the cloud boundary.

The particle mass flow rate distribution as a function of height within the duct cloud  $m(Z)$  can now be obtained graphically by knowing a value of  $m_0$  and drawing a straight line on a log-m scale from  $m_0$  to  $m = 10^{-K}$  at the cloud boundary ( $H_c$ ).

## (2) Near Field Density Distributions

The near flow field particle density distribution (at or below the rotor disc) in the region where the rotor induced flow is down through the disc was computed utilizing the flow continuity concept within a given stream tube. In this approach, it is assumed that the dust particles which get entrained from the dust cloud into the rotor plane travel along discrete stream tubes of the flow in which the basic law of mass flow continuity applies. It is further assumed that no particles are added or taken away from each stream tube and that there is no cross flow between the stream tubes.

If this concept of particle flow within a confined stream tube is utilized, it follows that the particle density distribution at points within the rotor plane or in the rotor slipstream (near flow field) is the same as that at



the appropriate locations within the dust cloud where the stream tube of the rotor induced flow immerses in the cloud. Hence, the near flow field particle density distribution can be computed knowing the far flow field densities at the appropriate locations within the dust cloud. The far flow field particle densities can be obtained utilizing the following equation:

$$(\rho_p)_{Av} = \frac{m}{u} \quad (45)$$

In utilizing equation (45), the average value of the near flow field density can be approximately obtained as that corresponding to the center point of the cloud roll-up above the rotor plane (Figure 15).

Although the above approach is considered to be adequate for predicting an average (order of magnitude) particle concentration at or below the rotor plane, it is believed to be inadequate for computing detailed particle distributions in the rotor near flow field. This is due to the fact that some of the dust particles which actually recirculate through the rotor disc are those which are entrained directly from the ground under their own momentum through the rotor "fountain flow" and from the recirculation region discussed previously.

An analytical treatment of the trajectories of discrete particles as affected by the airflow, the particle initial momentum, and the aerodynamic and gravitational forces acting on each particle is indeed very complicated and is considered to be outside the scope of the present work.

Because of a lack of such rigorous theoretical analysis on particle trajectories, a semi-empirical method postulated on pages 37 and 38 is

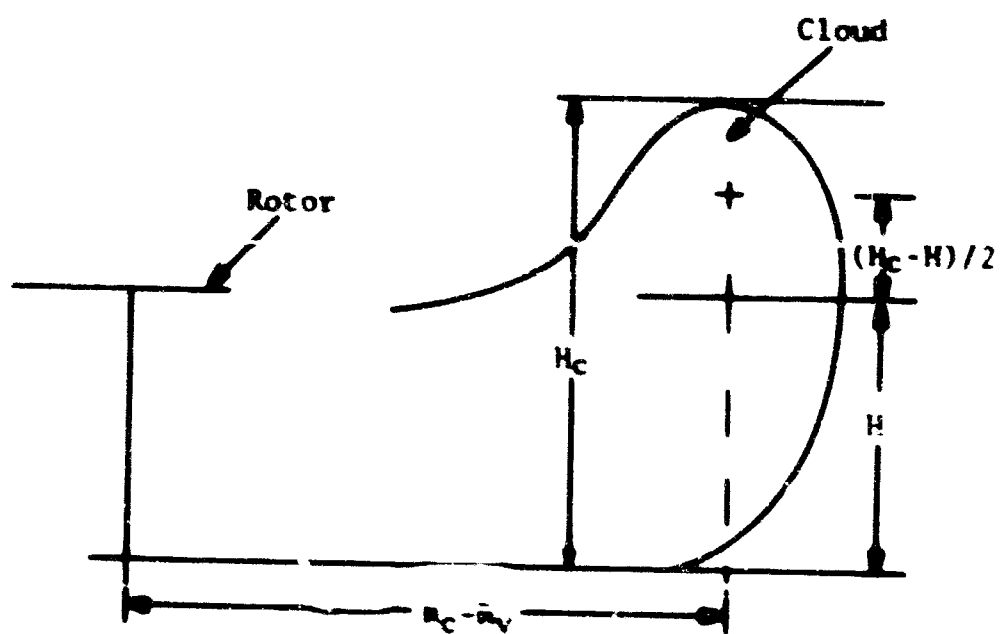


Figure 15. Schematic Representation of Dust Cloud Geometry.

herein utilized to obtain an indication of the order of magnitude of dust particle concentration at the rotor plane or at the probable location of engine intakes below the rotor. The results obtained by this method are expected to be lower than those obtained from the tests primarily because of the nature of the assumptions utilized in the analysis.

b. Particle Size Distribution

A method of predicting the particle size distribution in the downwash is presented in Reference 9. This method is based on the terminal velocity principle set forth by Kuhn in Reference 18, in which the free-fall terminal velocity of a particle is equated to the upflow velocity required to support this particle. This relationship was used to predict the maximum size of spherical ~~and~~ particles that can be supported by a given air velocity. The results are shown in Figure 16, which is reproduced from Reference 18.

The general procedure for determining the maximum size particles is to first obtain the magnitudes of the upflow velocities in the vicinity of the rotor operating in ground effect. Then the maximum size of the transported particles is obtained from Figure 16.

Once the maximum size of particles that can be supported by the local airflow is determined, it is related to the distribution of particles on the ground in the following manner. If the maximum size of transported particles is larger than the maximum size of particles available on the ground, then the distribution of particles in the air is assumed to be equal to that of the ground sample. If, however, the predicted maximum size of particles that can be supported by the local airstream is smaller than the maximum size on the ground, then the airborne particle distribution is modified as follows:

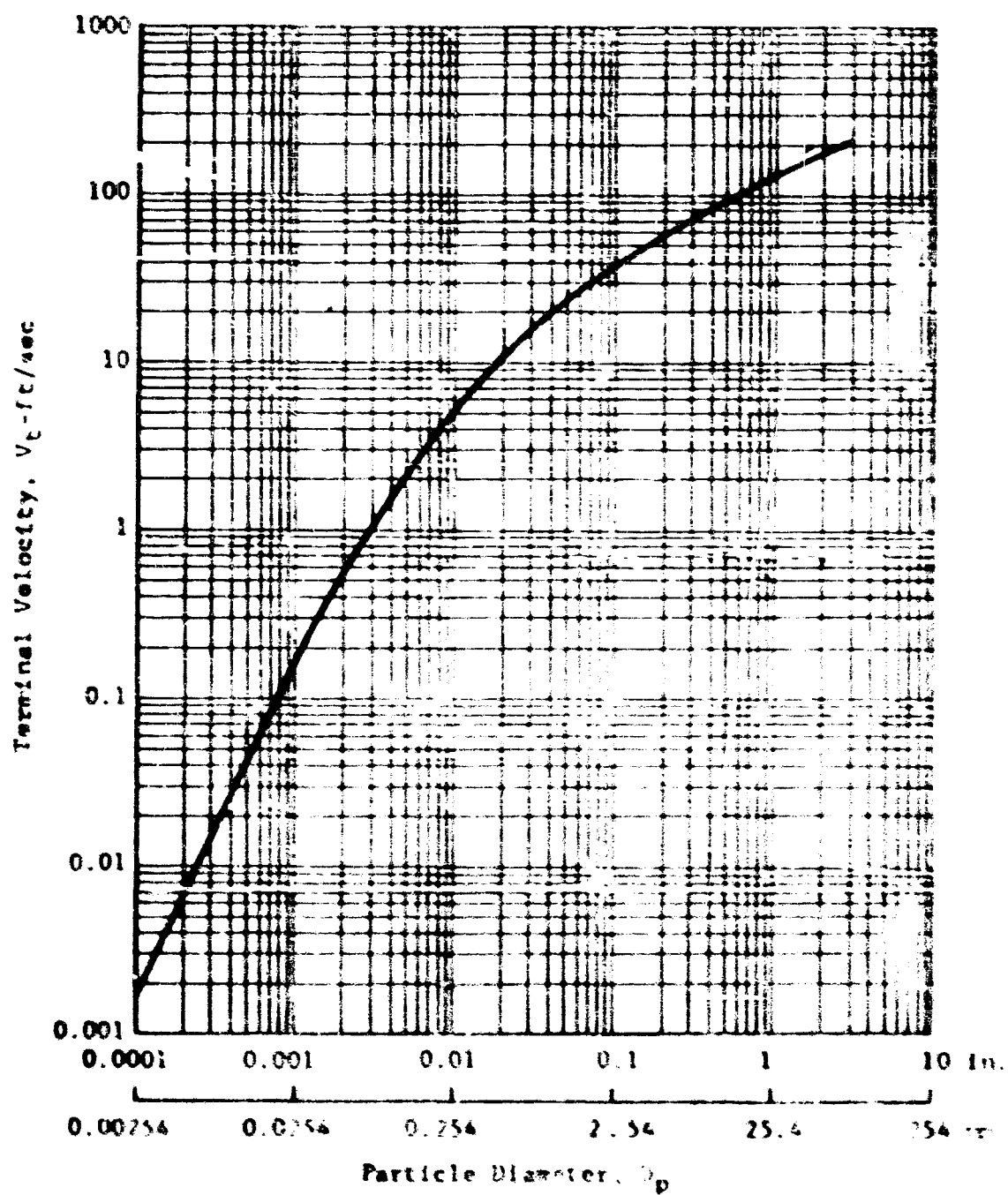


Figure 16. Variation of Terminal Velocity of Particles With Particle Diameter.

$$e_A = \frac{100}{(e_G)_{\max}} e_G \quad (46)$$

At each radial station, the maximum particle size distribution with height is obtained from Figure 16 where the terminal velocity is a local resultant velocity determined in Section II. A.

### C. DOWNWASH SIGNATURE EFFECTS

Presented in this section is a brief analysis of the effects of rotor downwash environment on pilot's visibility, engine, ground equipment, and personnel.

#### i. Pilot's Visibility

One of the potential hazards of operating a V/STOL aircraft in ground proximity is the loss of pilot's visibility due to the dust cloud formation generated by the rotor downwash.

The process of seeing involves the reception of light impressions by the eye from the sighted object. These light impressions are very much dependent on the contrast between object and background, the absolute background light intensity, and the geometric angle the object subtends at the eye. The relationship between these parameters has been established in Reference 19; the results directly applicable to this study have been extracted and are summarized in Figure 17.

The following analysis determines pilot visibility in terms of minimum perceivable object size for various distances from the pilot as affected by reduction of contrast and background light intensity created by the dust cloud.

Using Reference 20, the visibility reduction in terms of contrast reduction,  $C'$ , due to the contaminated atmosphere is given by:

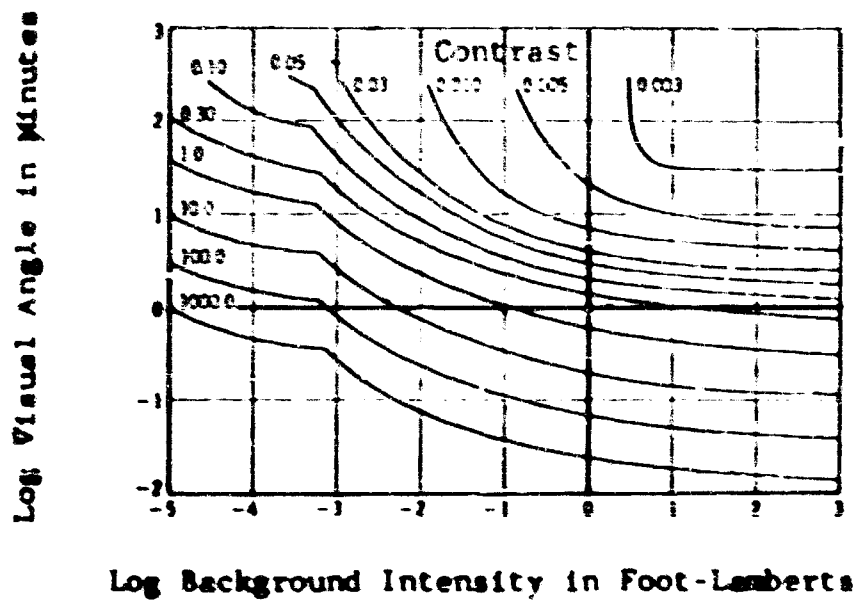


Figure 17. The Relation Between Visual Angle and Background Intensity for Test Objects of Constant Threshold Contrast.

$$C' = C \left( \frac{I_0}{I'_0} \right) T \quad (47)$$

where the uncontaminated contrast  $C$  is given by

$$C = \frac{I_s - I_0}{I_0} \quad (48)$$

Assuming that the background (terrain) intensity is independent of distance and cloud density, i.e.,  $I'_0 = I_0$ , then equation (47) reduces to

$$C' = TC \quad (49)$$

In equation (49), the parameter  $T$  represents the light transmittance which is defined as the ratio of light intensity emitted by the object placed within the dust cloud to that when the object is sighted in uncontaminated atmosphere. The light transmittance  $T$  can be expressed as follows:

$$T = e^{-NA_p d} \quad (50)$$

In the above equation, the number of particles per cubic foot of air,  $N$ , can be obtained by assuming that all airborne particles are equal to the mean particle size of the terrain. Using this assumption, equation (50) can be expressed as:

$$T = e^{-\left( \frac{\rho_p d}{1.5 \rho_G D_{ps}} \right)} \quad (51)$$

The geometric parameters which affect pilot's vision are the cloud penetration distance (d) measured along the pilot's line of vision to the object and the horizontal distance ( $S_h$ ) from the pilot to the object. The cloud penetration distance (d) is determined knowing the height (size) of the sighted object and the dust cloud geometry previously determined. The horizontal distance ( $S_h$ ) between the pilot and the object can be obtained from basic geometry.

Thus, using the nomenclature of Figure 18, the distance ( $S_h$ ) can be expressed in terms of radial distance (r) measured from the rotor centerline, the heading angle  $\psi$  relative to the object, and the aircraft geometry:

$$S_h^2 = r^2 - C^2 - 2rC \cos \alpha \quad (52)$$

where

$$C = \sqrt{A^2 + B^2} \quad (53)$$

$$\alpha = \psi - \vartheta - \beta - \sin^{-1} \left[ \frac{C}{r} \sin (90 - \vartheta - \beta) \right] \quad (54)$$

and

$$\beta = \tan^{-1} \left( \frac{A}{B} \right) \quad (55)$$



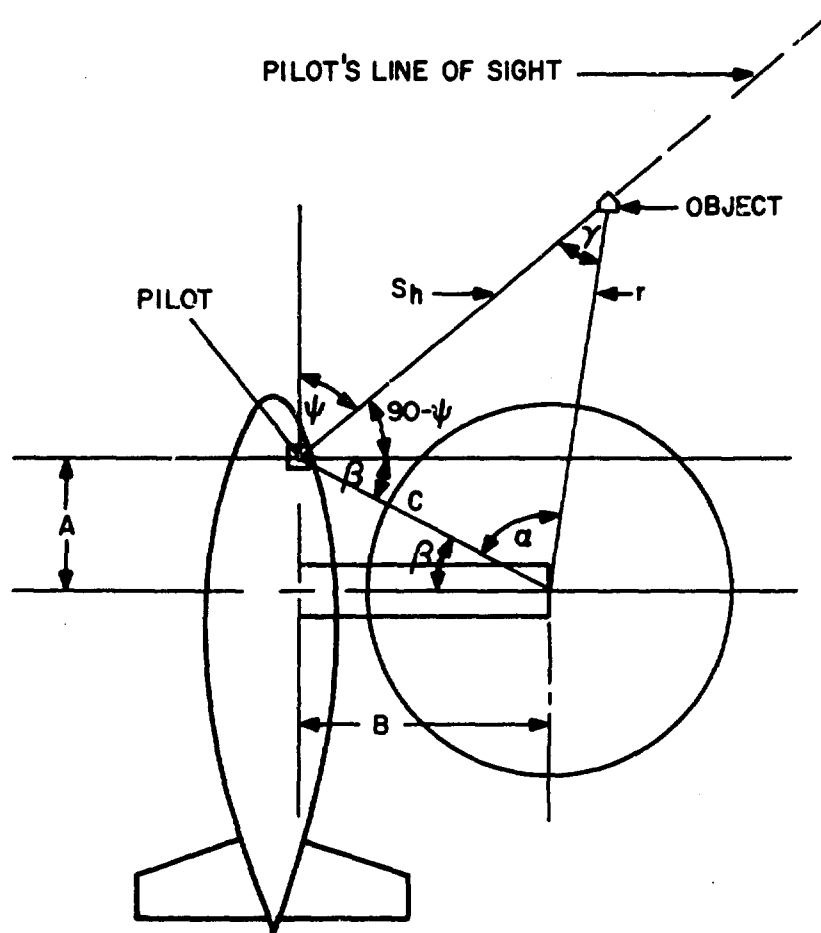


Figure 18. Pilot's Line of Sight Relative to Vehicle.

## 2. Engine and Equipment Damage

The rotor downwash environment generated by high-disc-loading V/STOL aircraft can cause severe damage to aircraft components (engine), equipment, and personnel placed in the vicinity of hovering aircraft.

No specific analytical methods are available to predict the degree of such damage. However, some information on this subject was obtained from the pertinent wind tunnel and full-scale flight tests and is presented in Section III. C.

### III. DOWNWASH ENVIRONMENT RESULTS FOR VARIOUS V/STOL AIRCRAFT

Although the analytical methods presented in the previous section are completely general, the application of these methods for predicting the downwash environment of a specific V/STOL configuration requires minor modification to properly account for the number of lift devices, aircraft geometry, and terrain conditions.

These methods have been used to predict the contaminant cloud characteristics for the H-21, XC-142, X-22A, X-19A, and XV-5A V/STOL aircraft operating over silty sand. The results obtained for these aircraft are presented below.

#### A. FLOW FIELD

##### 1. Flow Field Above Rotor Plane (Region 1)

The nondimensionalized velocity profiles of the flow field above the rotor plane (inside and outside vortex cylinder - Regions 1A and 1B) applicable to the H-21, XC-142, X-22A, X-19A, and XV-5A V/STOL aircraft configuration are presented in Figure 5. The dimensional values of the flow field for each aircraft can be obtained by multiplying the nondimensional values of Figure 5 by the corresponding average momentum velocities of the fully developed slipstream of each aircraft and the appropriate ground effect factor given in Figure 4.

##### 2. Flow Field Below Rotor Plane (Region 2)

The velocity profiles below the rotor plane (Region 2) applicable to the H-21, XC-142, X-22A, X-19A, and XV-5A V/STOL aircraft are presented in the nondimensional form in Figure 6. The dimensional values of the slipstream velocity for each aircraft can be obtained by multiplying the values of Figure 6 by appropriate average momentum value of the induced velocity at the rotor plane.

##### 3. Wall Jet Flow (Region 3)

Using the analytical methods developed in Section II. A. 3 and the aircraft geometric parameters listed in Table I,

TABLE I				
GEOMETRIC PARAMETERS OF V/STOL AIRCRAFT				
Aircraft	Gross Weight (lb)	Rotor/Prop Diameter (ft)	Disc Loading (psf)	Rotor Height With Wheels on Ground (ft)
H-21	13,000	44.0 x 2	4.28	16.0
XC-142	37,500	15.6 x 4	49.68	20 (avg)
X-22	15,800	7.0 x 4	103.0	7.5 (avg)
X-19	13,660	13.0 x 4	25.73	12.02
XV-5A	9,200	5.2 x 2	288.8	5.15
Sea-Level Conditions				

the wall jet velocity profiles have been calculated for the selected aircraft for wheels on the ground and also for wheels 50 feet above the ground for the XC-142 aircraft.

The results for zero wheel clearance of the selected aircraft are presented in Figures 19 and 20, which show the wall jet velocity distribution at the location where the wall jet begins and at a common radial station 90 feet from the rotor centerline, respectively. From these figures, it can be noted that the wall jet contours for high-disc-loading aircraft are substantially lower in overall thickness than those for low-disc-loading aircraft. It can also be seen that although a much higher surface velocity occurs close to the high-disc-loading aircraft, these velocities decrease more rapidly with increasing radial distance than those for low-disc-loading aircraft.

Figure 21 shows the velocity profiles for the XC-142 aircraft operating at 50 feet wheel clearance from the ground. Comparing the results of Figures 19, 20, and 21 for this aircraft,

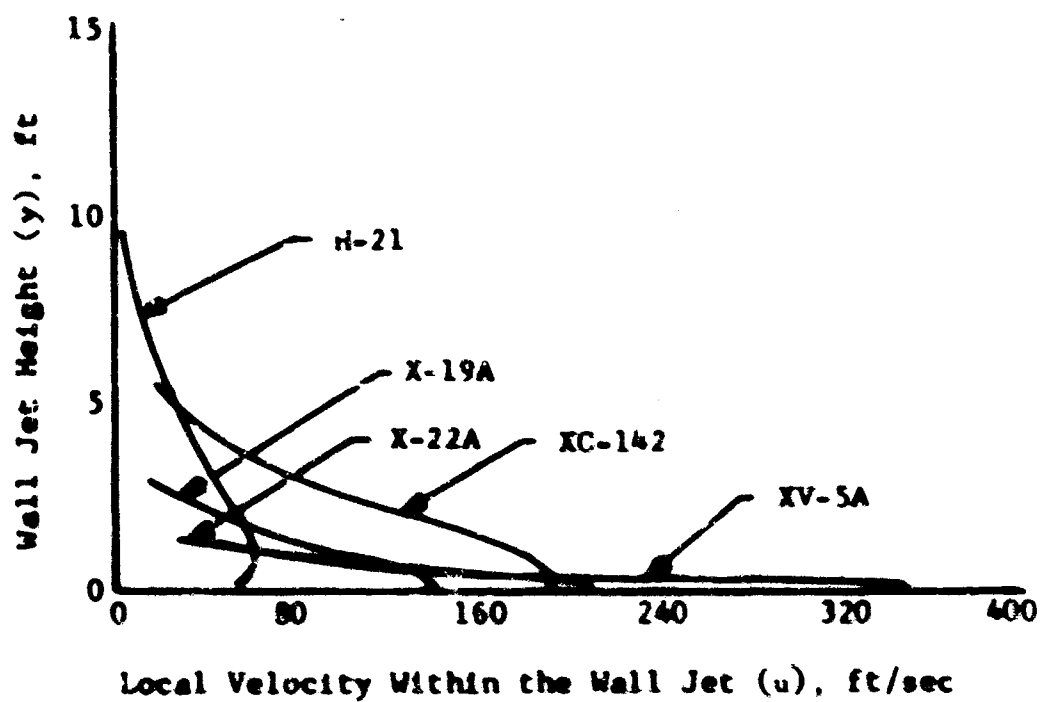


Figure 19. Comparison of Wall Jet Velocity Distributions for Various Aircraft at the Start of the Wall Jet. Wheels on the Ground.

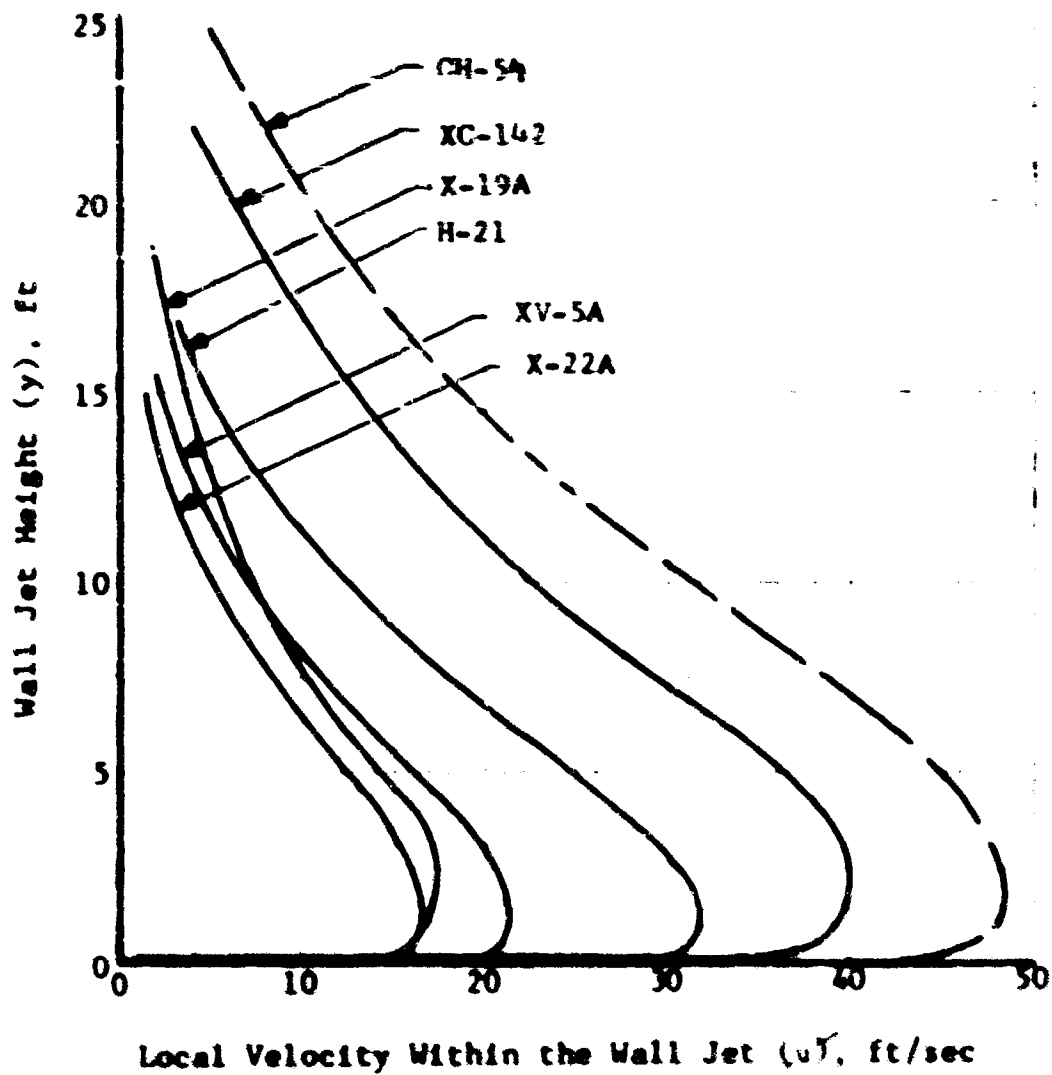


Figure 2C. Comparison of Wall Jet Velocity Distributions for Various Aircraft at a Common Radial Station ( $X = 90$  Feet). Wheels on the Ground.

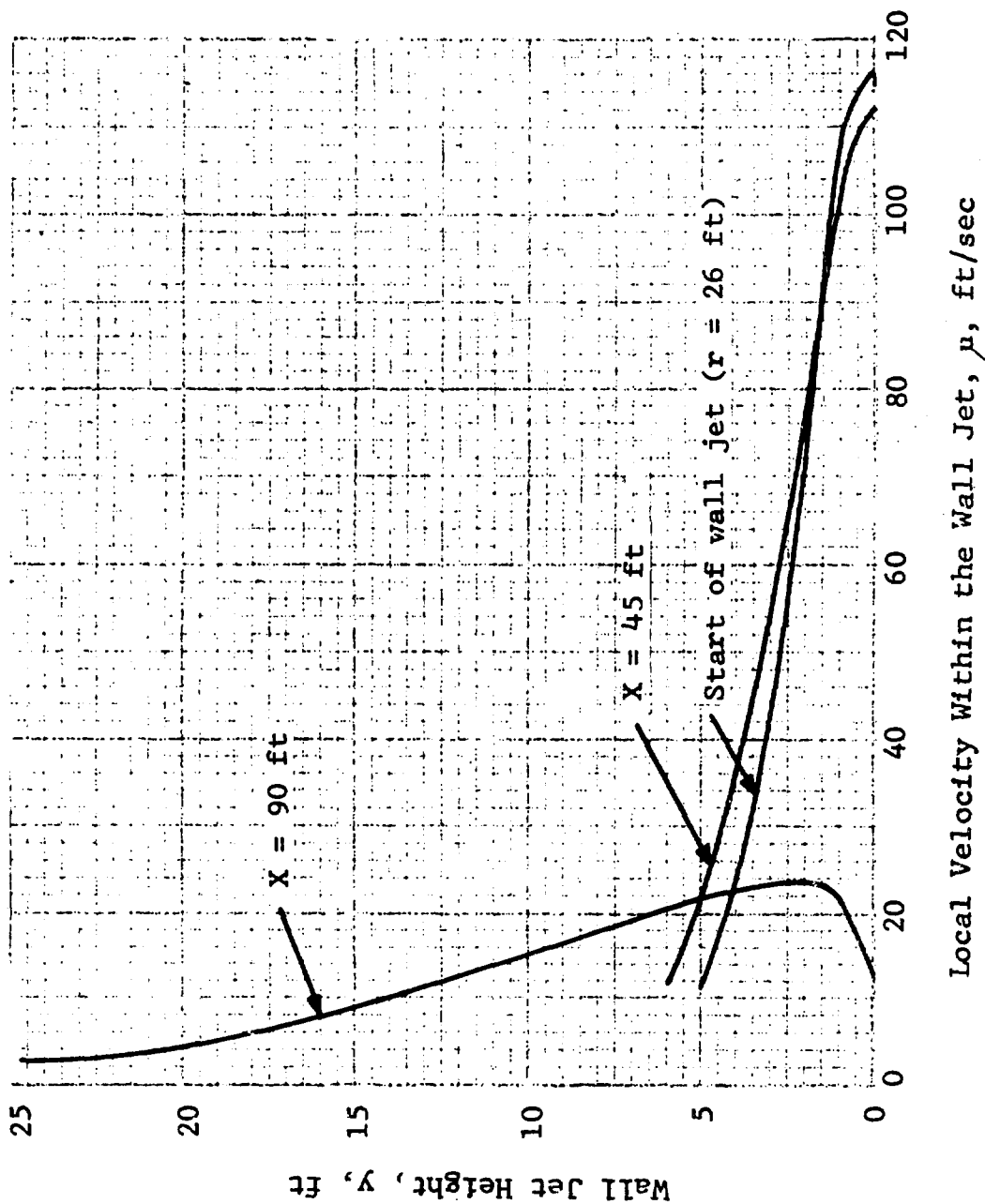


Figure 21. Wall Jet Velocity Distribution for XC-142 Aircraft at Various Radial Stations, Wheel Clearance,  $H_W = 50$  Feet.

it can be noted that the effect of rotor height above the ground is to reduce the magnitudes of the wall jet velocities at an approximate rate of 1 percent per foot height of the corresponding wall jet velocity with wheels on the ground.

The results of Figure 19 are replotted in Figure 22 in terms of maximum surface dynamic pressure versus radial distance from the rotor centerline. This figure indicates that the maximum surface dynamic pressure at the radial location where the wall jet begins is a strong function of aircraft disc loading. This trend is not indicated at other radial locations within the wall jet.

#### 4. Recirculation Flow (Region 4)

The flow recirculation area for the aircraft having four lifting devices arranged side by side and in tandem is bounded by two expanding interaction planes, one along the longitudinal and one along the lateral plane of symmetry. For these aircraft, the flow recirculation area as defined in Section II. A. 4 is comparatively small and does not warrant special analysis. Therefore, the computations of the flow field in this region were performed only for the H-21 and XC-142 aircraft and are presented in Table II. Table III presents the results for the XC-142 aircraft operating at 50 feet wheel clearance from the ground.

From the results shown in Tables II and III, it can be noted that the magnitudes of the velocities in this region are quite small (less than 9 ft/sec). Furthermore, the effect of wheel clearance (rotor height) on the magnitudes of these velocities is negligible.

#### 5. Flow in the Interaction Region

The equations derived in Section II. A. 5 have been utilized to compute the horizontal and vertical velocity components in the interaction plane at distances of 45 and 90 feet. The results are presented in Figures 23 through 27 for all selected aircraft with wheels on the ground, and in Figure 28 for the XC-142 aircraft operating at 50 feet wheel clearance from the ground. It should also be noted that since the results presented in Figures 23 through 28 do not include



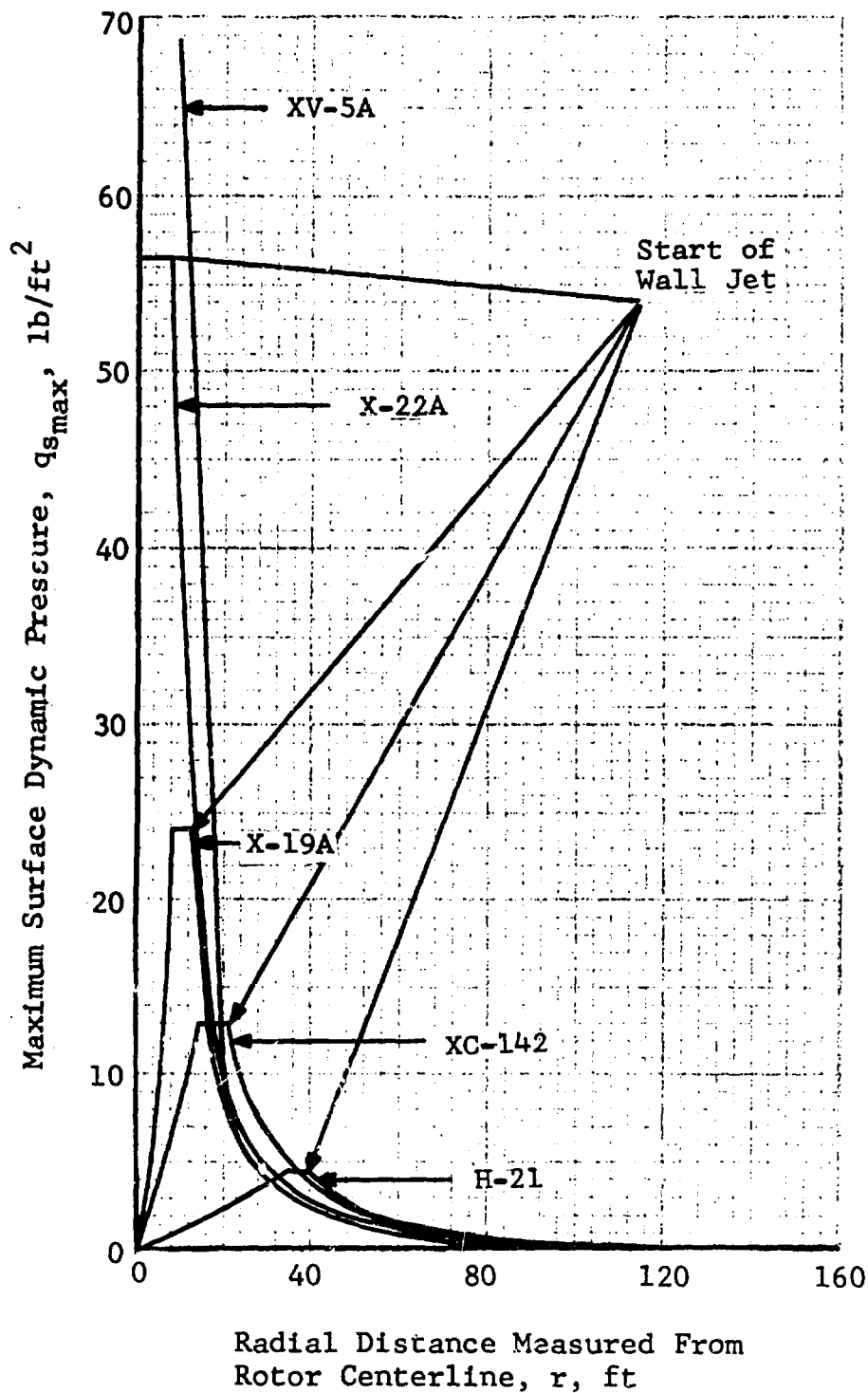


Figure 22. Variation of Maximum Surface Dynamic Pressure Along the Ground for Various Aircraft. Wheels on the Ground.

TABLE II					
HORIZONTAL COMPONENTS OF THE VELOCITIES* IN THE RECIRCULATION REGION, WHEELS ON THE GROUND					
(a) H-21					
h, ft measured from rotor plane	X=50 ft $U_X$	X=60 ft $U_X$	X=70 ft $U_X$	X=80 ft $U_X$	X=90 ft $U_X$
0	2.6	3.88	2.84	2.18	1.72
2.5	4.4	2.94	1.96	1.4	0.94
5	3.26	2.04	1.06	0	0
8	1.86	.92	0		
10	0.94	0			
12	0				
(b) XC-142					
h, ft measured from rotor plane	X=50 ft $U_Y$	X=60 ft $U_Y$	X=70 ft $U_Y$		
0	9.2	5.45	3.66		
2	7.6	4.36	2.74		
4	6.1	3.3	1.83		
6	4.6	2.1	.914		
8	3.0	1.07	0		
10	1.5	0			
12	0				
*Velocities in Feet per Second					

TABLE III				
HORIZONTAL COMPONENTS OF THE VELOCITIES* IN THE RECIRCULATION REGION - $H_{ty} = 50$ Feet				
XC-142				
h, ft measured from rotor plane	X=50 ft $U_y$	X=75 ft $U_y$	X=100 ft $U_y$	X=125 ft $U_y$
0	9.46	3.18	1.62	0.99
10	7.88	2.54	1.21	0.66
20	6.31	1.91	0.81	0.33
30	4.73	1.27	0.40	0
40	3.15	0.64	0	
50	1.58	0		
60	0			
*Velocities in Feet Per Second				

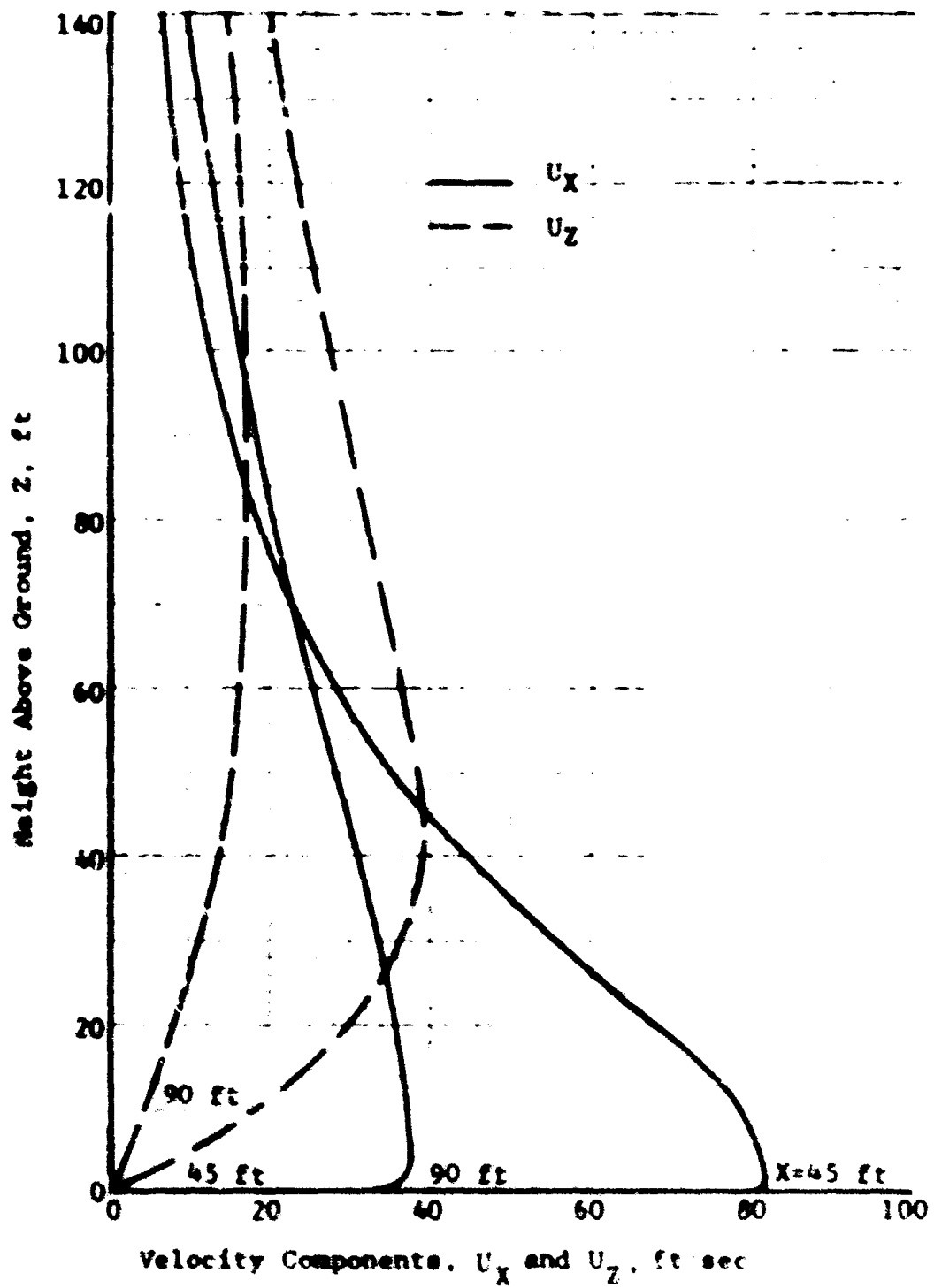


Figure 23. Horizontal and Vertical Velocity Components Along the Interaction Plane for the H-21 Aircraft. Wheels on the Ground.

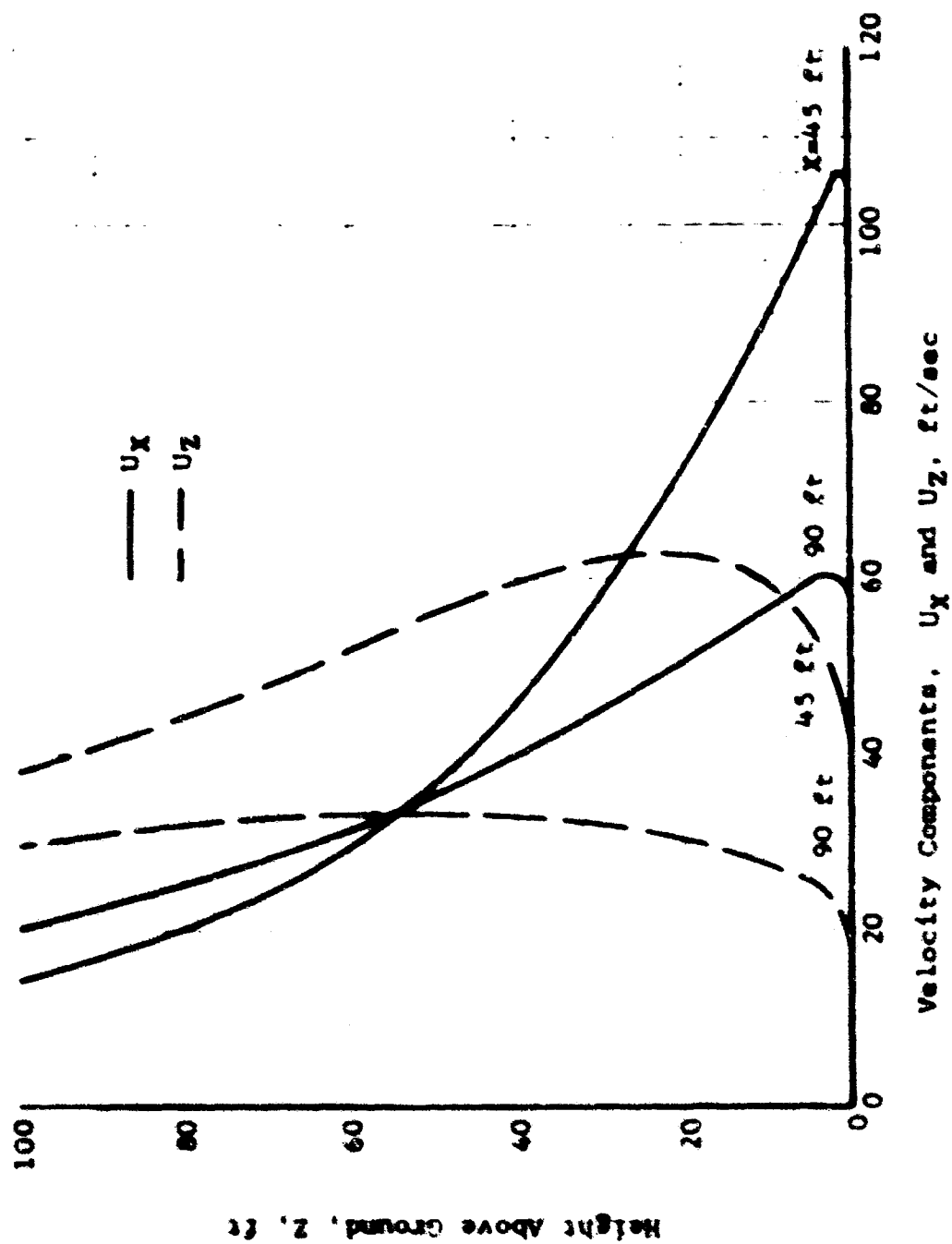


Figure 24. Horizontal and Vertical Velocity Components Along Interaction Plane for the XC-142 Aircraft. Wheels on the Ground.

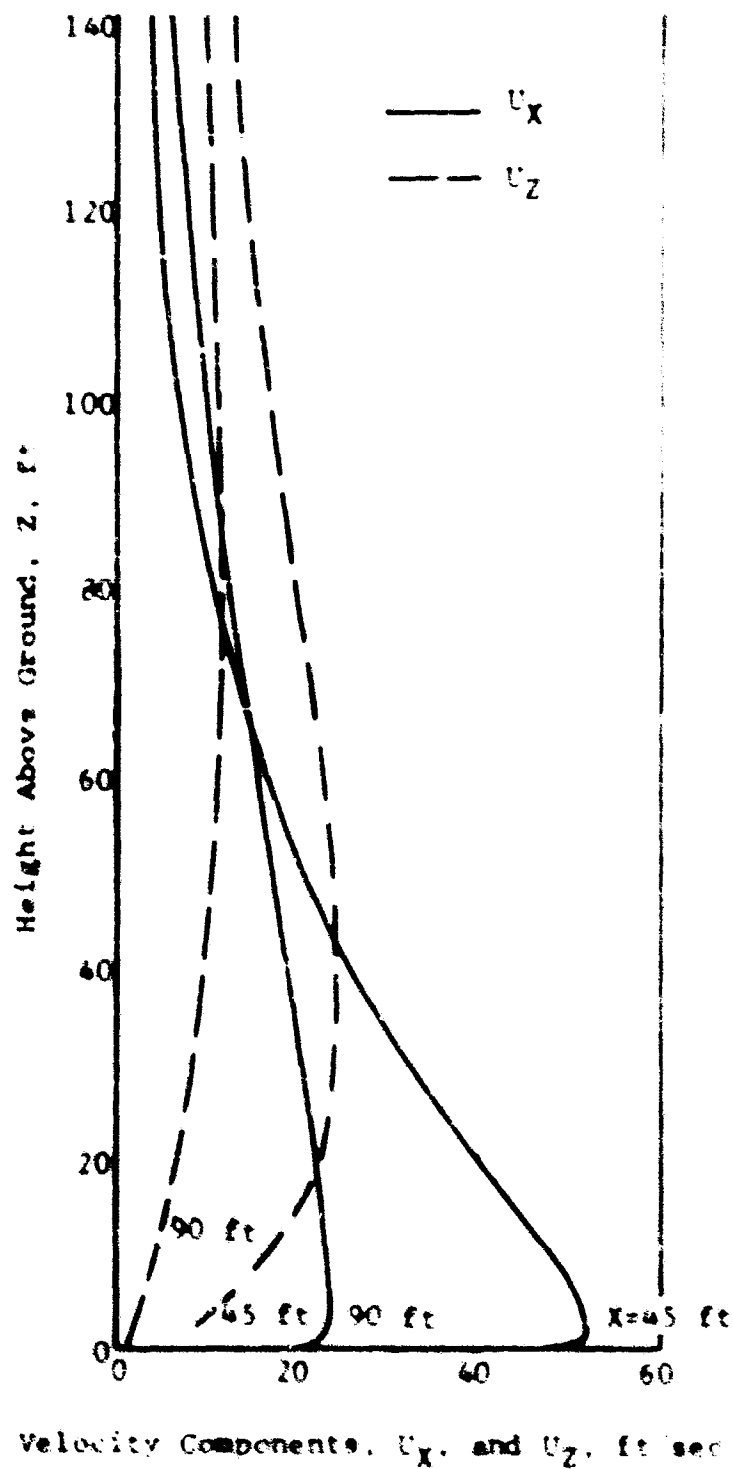


Figure 25. Horizontal and Vertical Velocity Components Along Interaction Plane for the X-22A Aircraft. Wheels on the Ground.

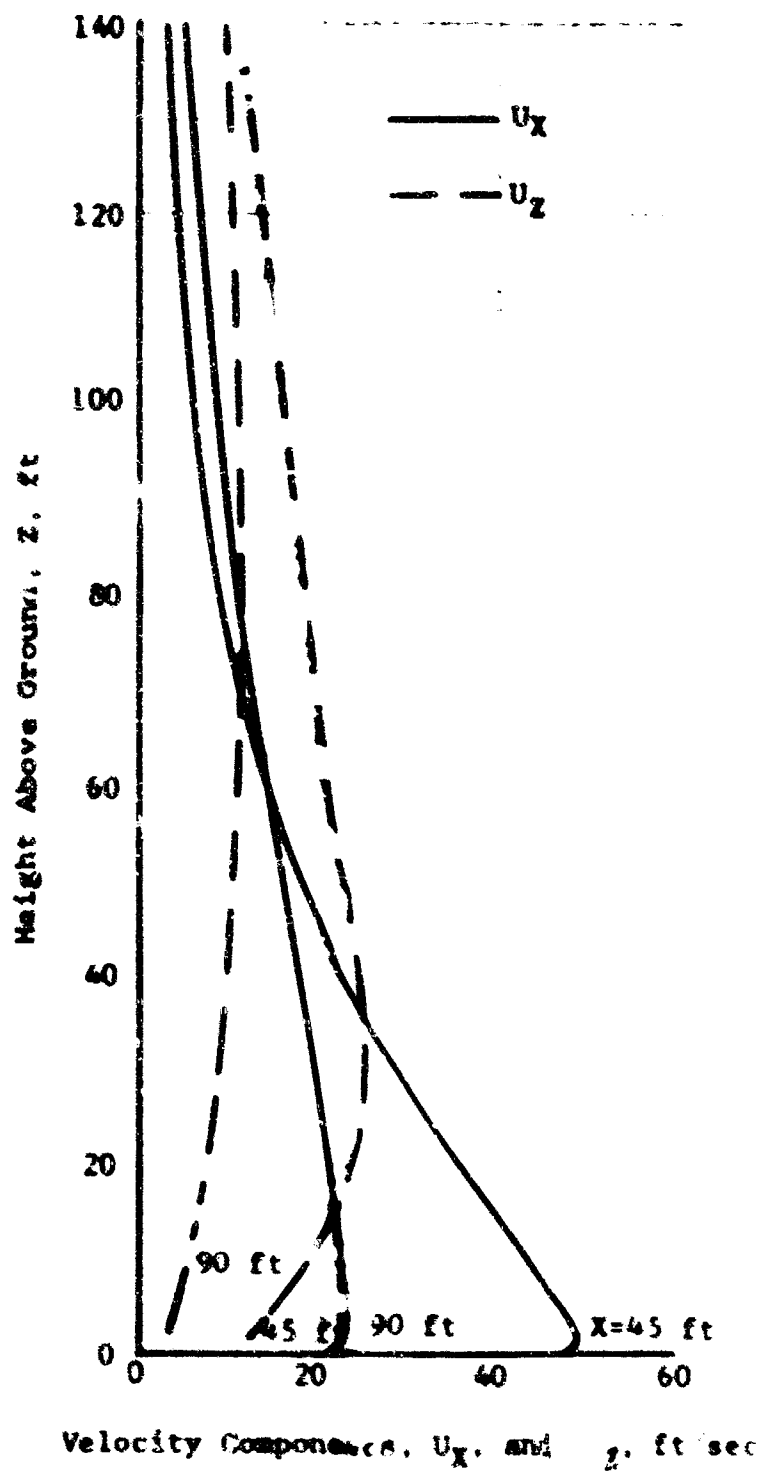


Figure 26. Horizontal and Vertical Velocity Components Along Interaction Plane for the X-19A Aircraft. Wheels on the Ground.

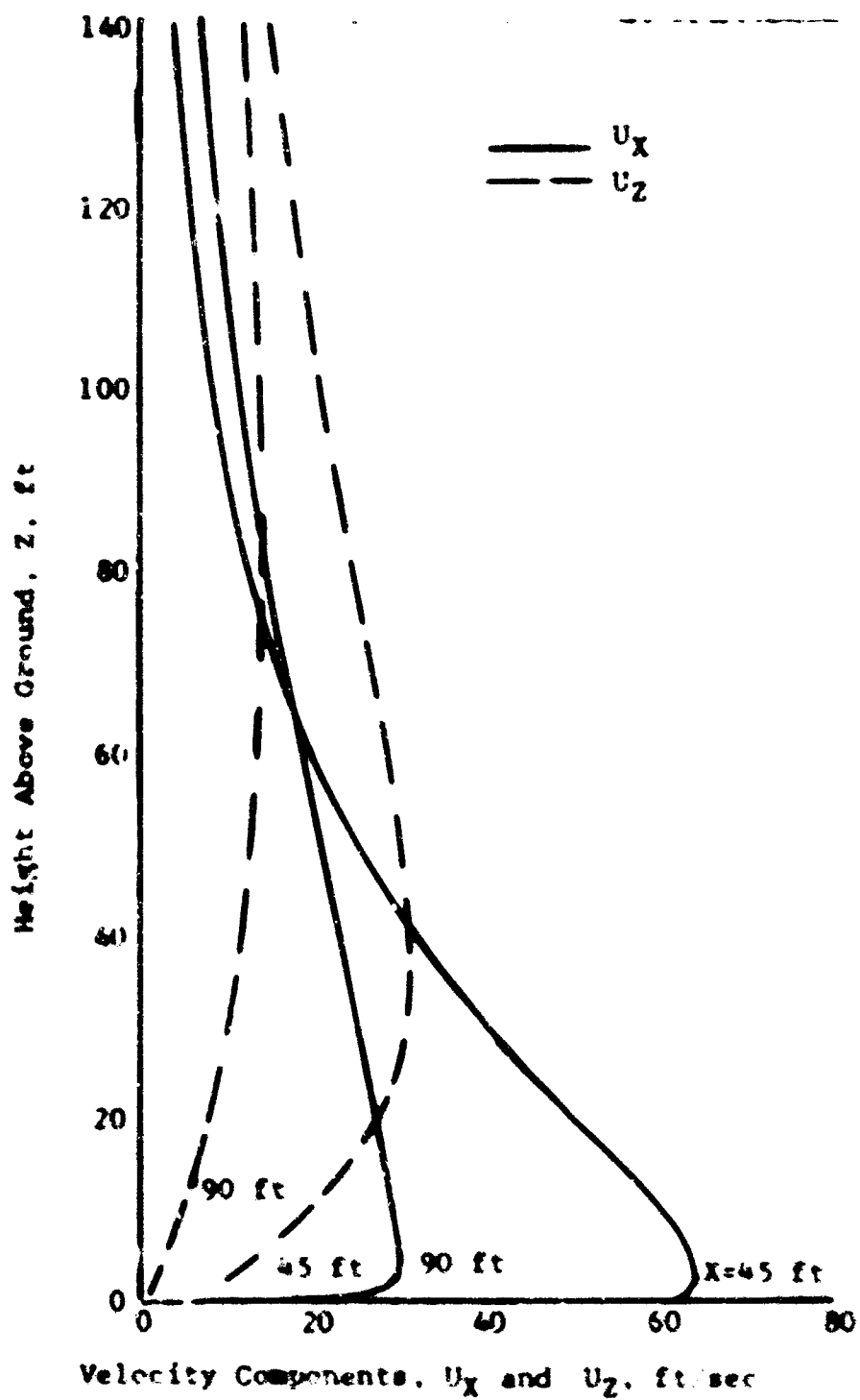


Figure 27. Horizontal and Vertical Velocity Components Along Interaction Plane for the XV-5A Aircraft. Wheels on the Ground.



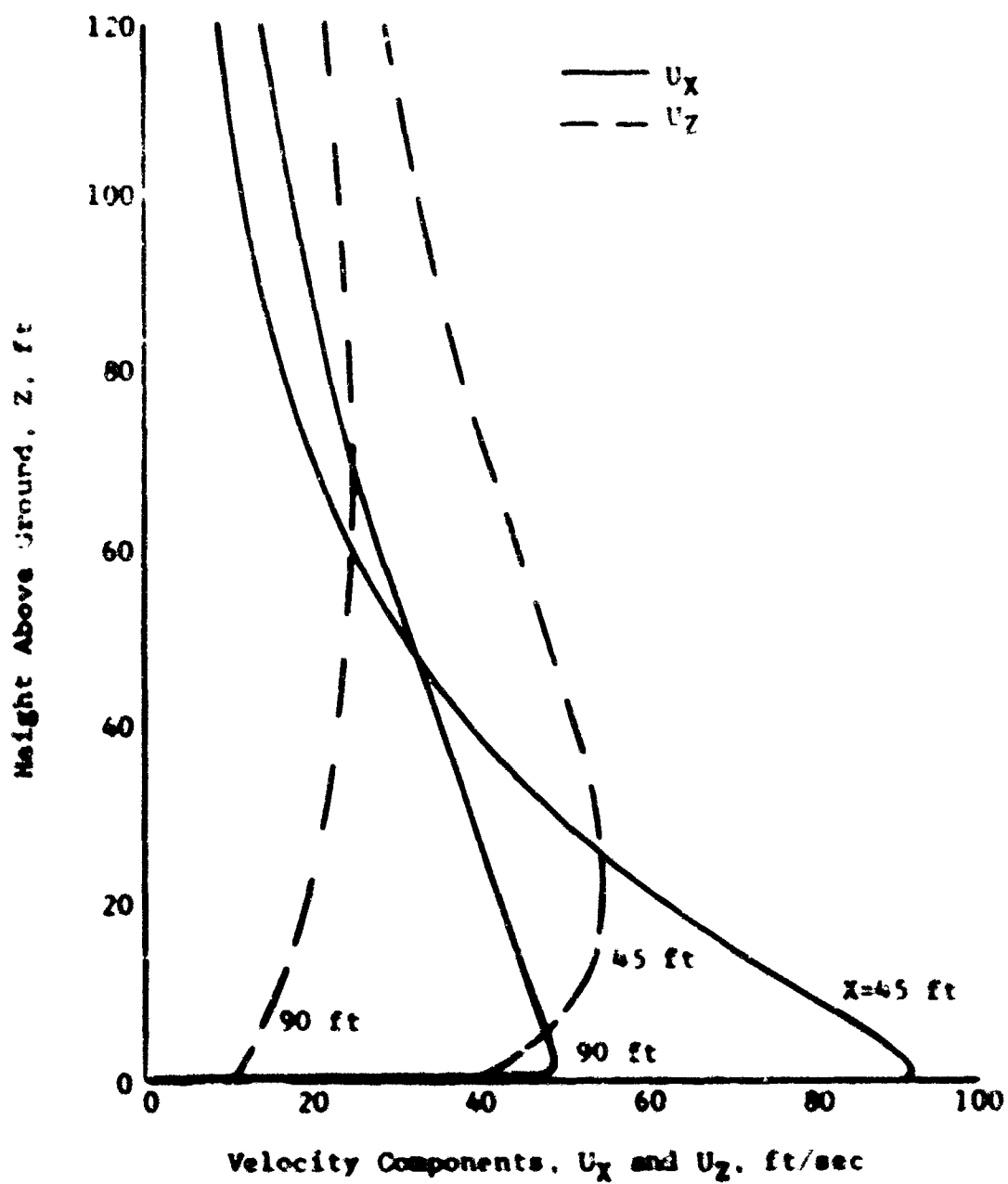


Figure 28. Horizontal and Vertical Velocity Components Along Interaction Plane for the XC-142 Aircraft,  $H_w = 50$  Feet.

air viscosity effects, the calculated values represent upper bounds of the velocities to be expected in this region.

#### 6. Contour Plots of Maximum Surface Dynamic Pressure

It is convenient to combine the velocity results computed in Region 3 (Wall Jet Region) and Region 5 (Interaction Plane Region) for the selected aircraft in the form of contour plots of the maximum surface dynamic pressure along the ground. Such comparative contour plots obtained for the H-21, XC-142, X-22A, X-19A, and XV-5A aircraft with wheels on the ground are presented in Figures 29, 30, 31, 32, and 33, respectively. Figure 34 shows the results for the XC-142 aircraft operating at 50 feet wheel clearance from the ground.

From these figures, it can be noted that along the interaction plane of two rotor configurations, higher maximum dynamic pressures are generally indicated than those of a single jet configuration. This is readily apparent in regions far from the aircraft center. Near the aircraft, however, the flow in the interaction plane is nearly vertical; hence, the horizontal component of the dynamic pressure shown in the contour plots is smaller than that for an equivalent single jet.

Furthermore, as was previously noted, the dynamic pressure along the ground in the wall jet region for a low disc loading aircraft is relatively low, but it persists at much greater distances as compared to high disc loading aircraft of equivalent gross weight.

#### B. DUSTWASH SIGNATURES

##### 1. Cloud Size and Shape

The radial boundary ( $R_c$ ) and height ( $H_c$ ) of the dust clouds for the selected V/STOL aircraft were computed utilizing techniques developed in Section II. B. 1. The details of the dust cloud shape were established utilizing good engineering judgement based on the actual observations and recorded film data of a variety of V/STOL aircraft operating in dust environment. The consistency of the ground terrain considered for this study is loose silty sand found at Phillips Drop Zone

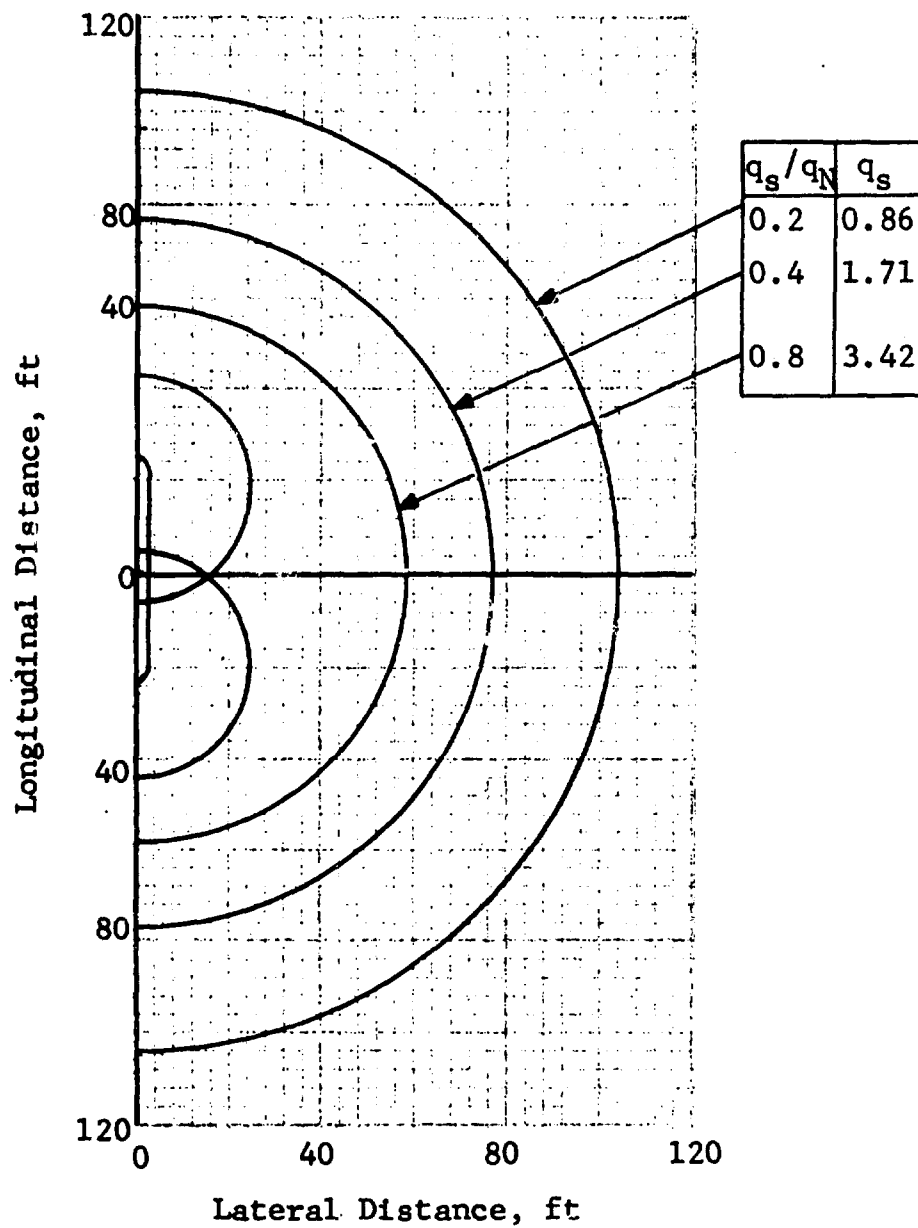


Figure 29. Contour Plots of Maximum Surface Dynamic Pressure Along the Ground for the H-21 Aircraft. Wheels on the Ground.

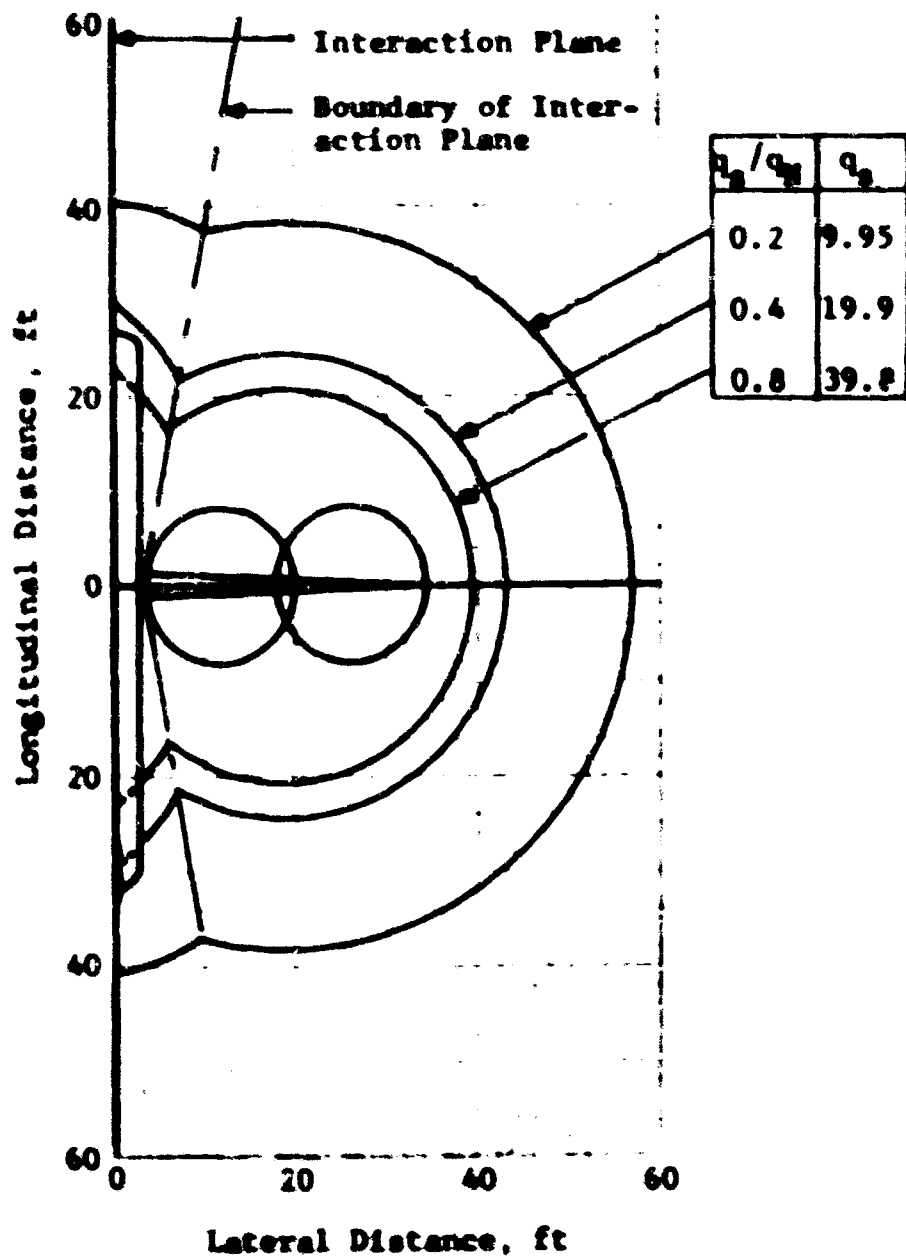


Figure 30. Contour Plots of Maximum Surface Dynamic Pressure Along the Ground for the XC-142 Aircraft. Wheels on the Ground.

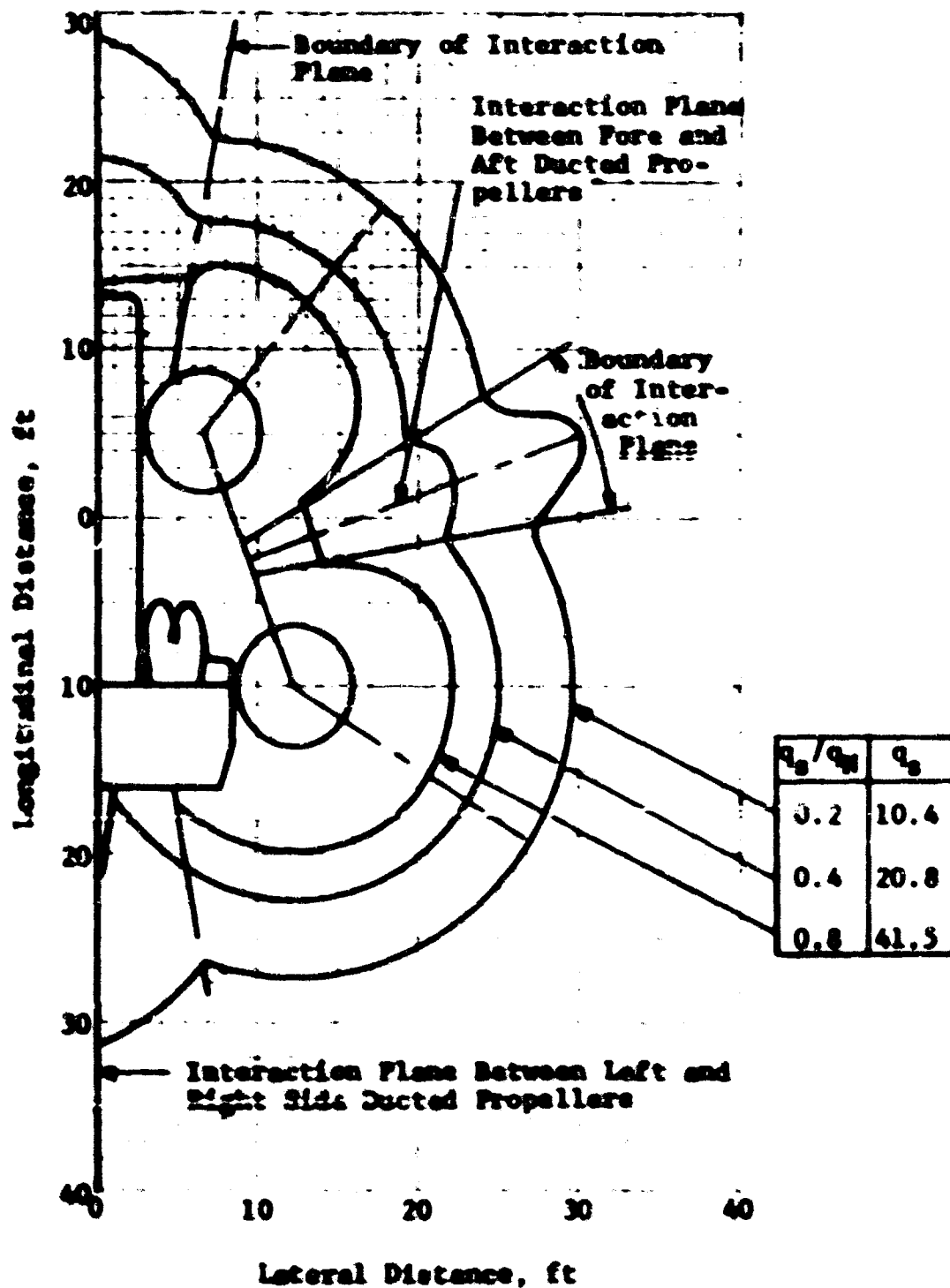


Figure 31. Contour Plots of Maximum Surface Dynamic Pressure Along the Ground for the X-22A Aircraft. Wheels on the Ground.

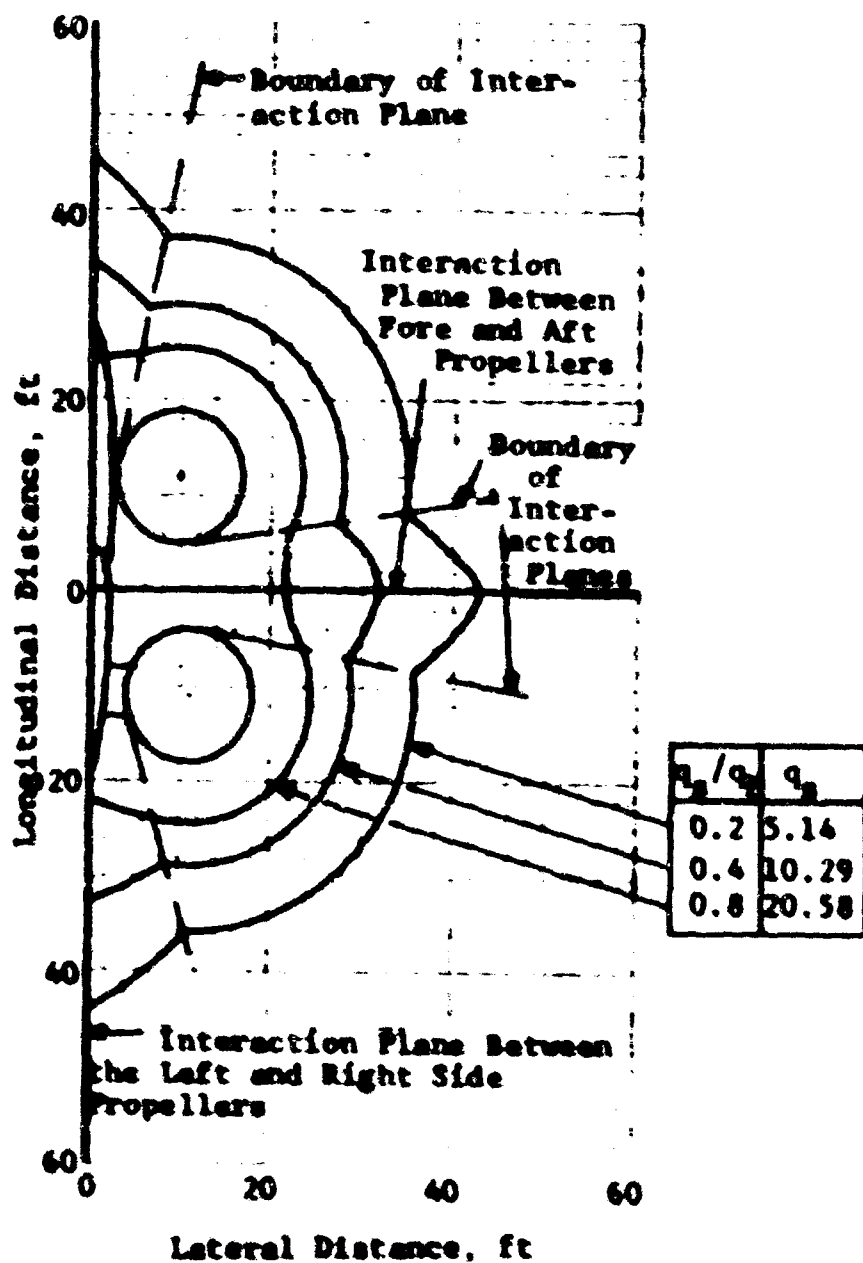


Figure 32. Contour Plots of Maximum Surface Dynamic Pressure Along the Ground for the X-19A Aircraft. Wheels on the Ground.

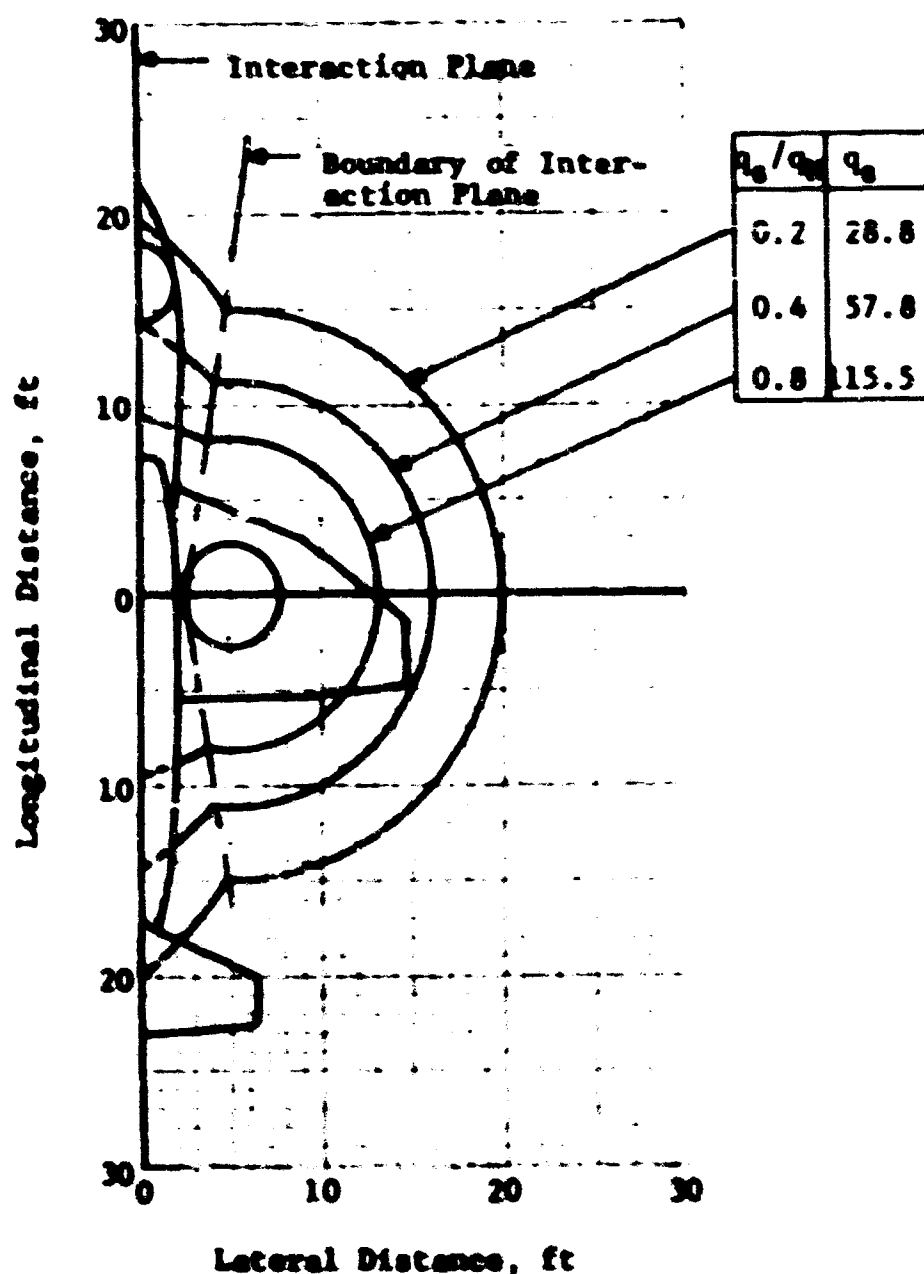


Figure 33. Contour Plots of Maximum Surface Dynamic Pressure Along the Ground for the XV-5A Aircraft. wheels on the Ground.

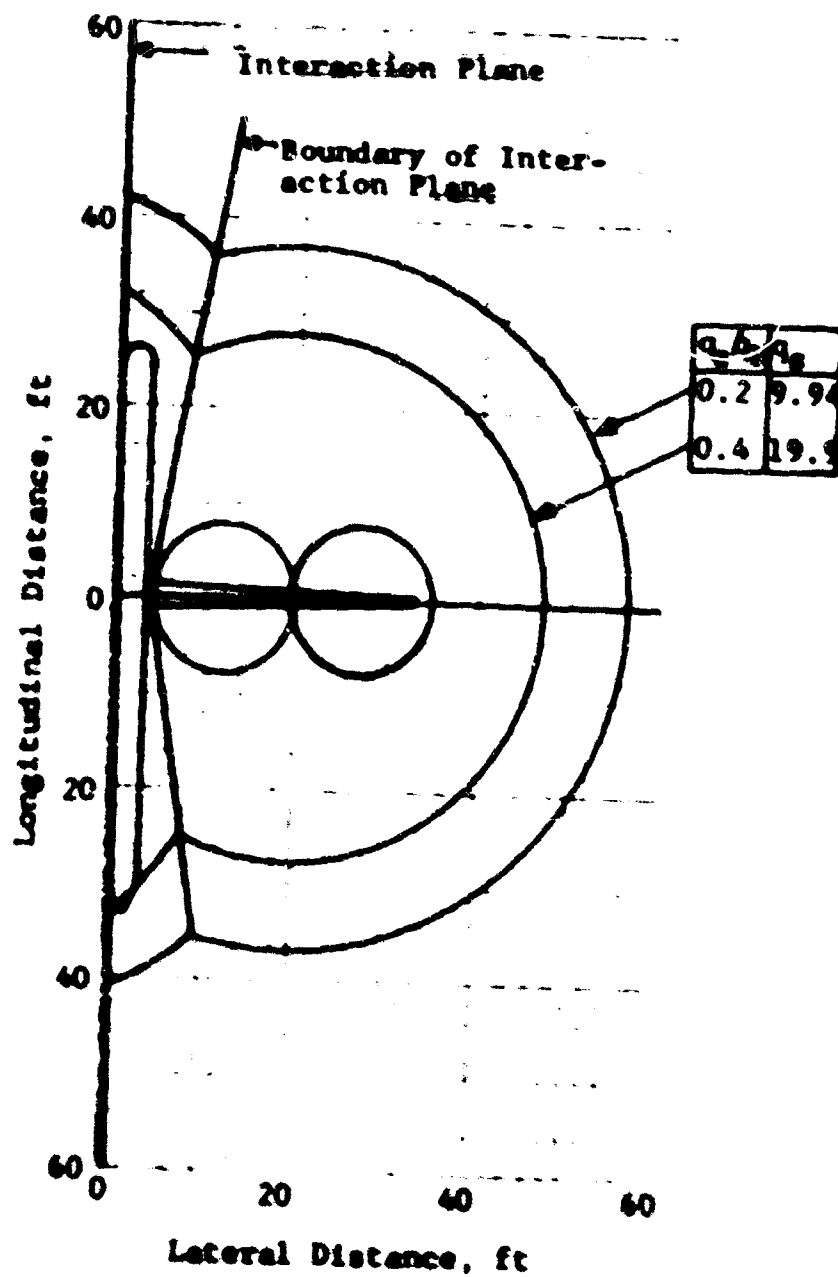


Figure 34. Contour Plots of Maximum Surface Dynamic Pressure Along the Ground for the XC-142 Aircraft,  $H_W = 50$  Feet.



of Yuma Proving Grounds. The ground sample selected for this study and presented in Figure 35 shows ground particle size distribution by weight. Additional information on the ground sample is presented in the appendix.

Figures 36, 37, 38, and 40 show the dust clouds predicted for the H-21, XC-142, X-22A, X-19A, and XV-5A aircraft, respectively. These figures present the cloud sizes and shapes along both longitudinal and lateral planes for each aircraft for zero wheel clearance. Figure 41 shows the corresponding results for the XC-142 aircraft operating at 50 feet wheel clearance from the ground.

For multirotor configurations, one or both of these planes is the interaction plane. Figures 36 through 41 clearly indicate the asymmetry of the cloud shapes in the two planes. Film data such as those obtained from the test program reported in Reference 15 indicate that the cloud shape resembles that of a torus, or a doughnut, with its center at the center of the aircraft.

In order to obtain a better indication of the effects of aircraft parameters on dust cloud size, the results of Figures 36 through 40 are cross-plotted in Figures 42 and 43, which show the variation of maximum radial and vertical cloud sizes as a function of the dynamic pressure of a fully developed slipstream for each aircraft. It can be noted from these figures that for approximately constant gross weight (e.g., CH-47B, CH-54, and XC-142 aircraft), both the maximum dust cloud radius and height slightly decrease with an increase in disc loading. Furthermore, the maximum dimensions of the dust cloud increase appreciably with an increase of aircraft gross weight (compare H-21 or X-22 data with XC-142 data).

These figures also present the available test data obtained from the films of References 15 and 21 and the unpublished test data obtained at Edwards Air Force Base for the selected aircraft. Incidentally, good correlation can be noted between the predicted cloud sizes and those obtained from the films.

The effect of rotor height on cloud sizes can be obtained by comparing the results of Figure 37(a) (zero wheel clearance)

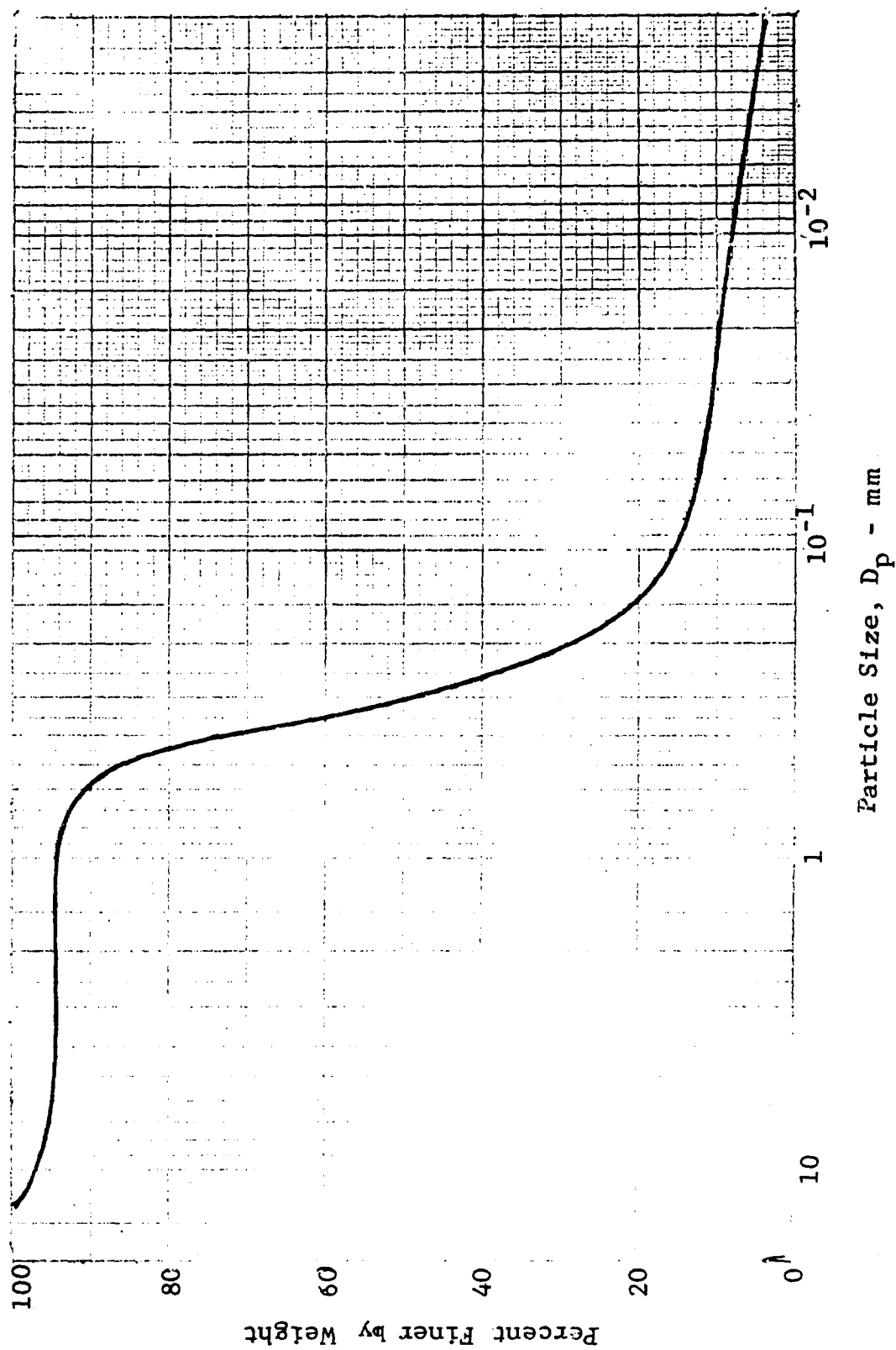


Figure 35. Ground Sample Particle Size Distribution.

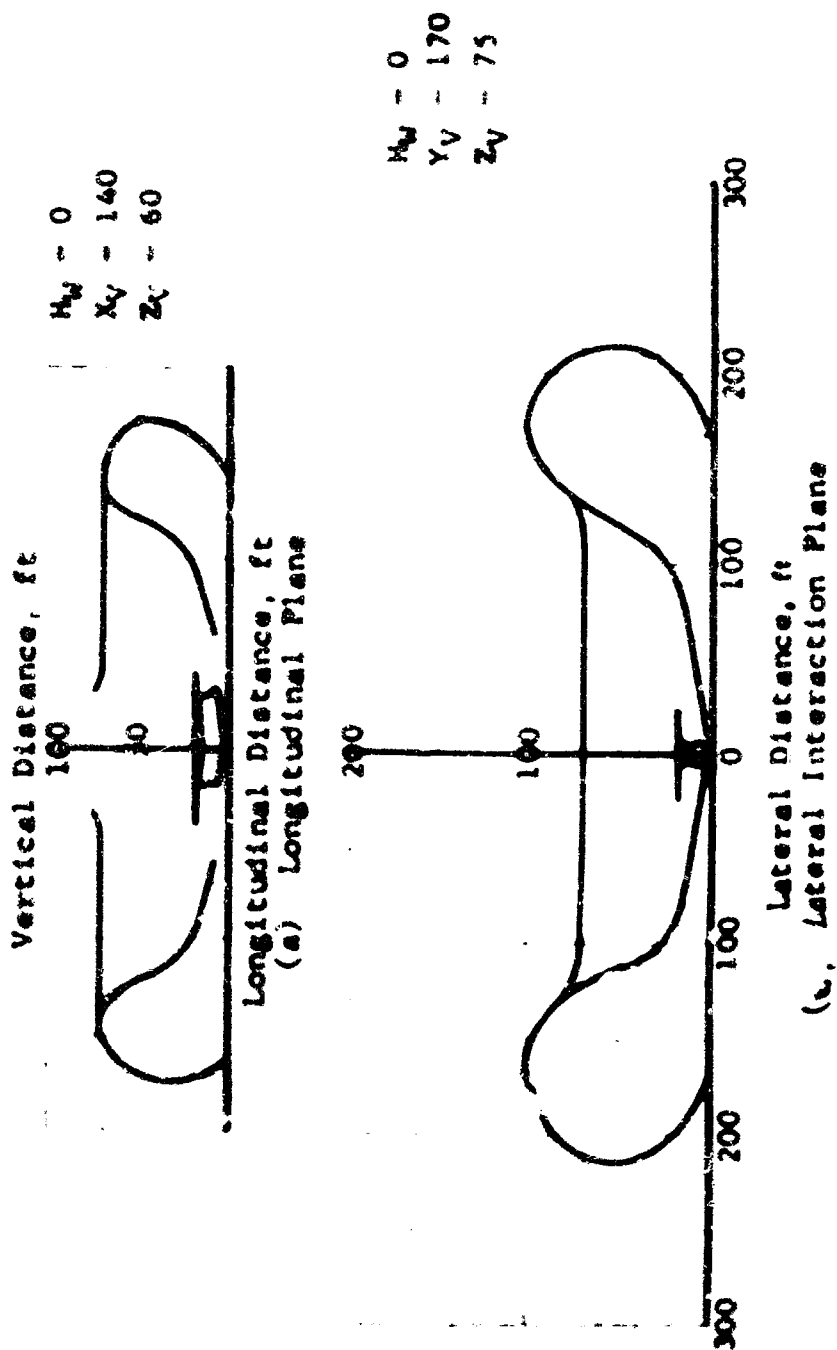


Figure 36. Dust Cloud Size and Shape for the H-2i Helicopter.

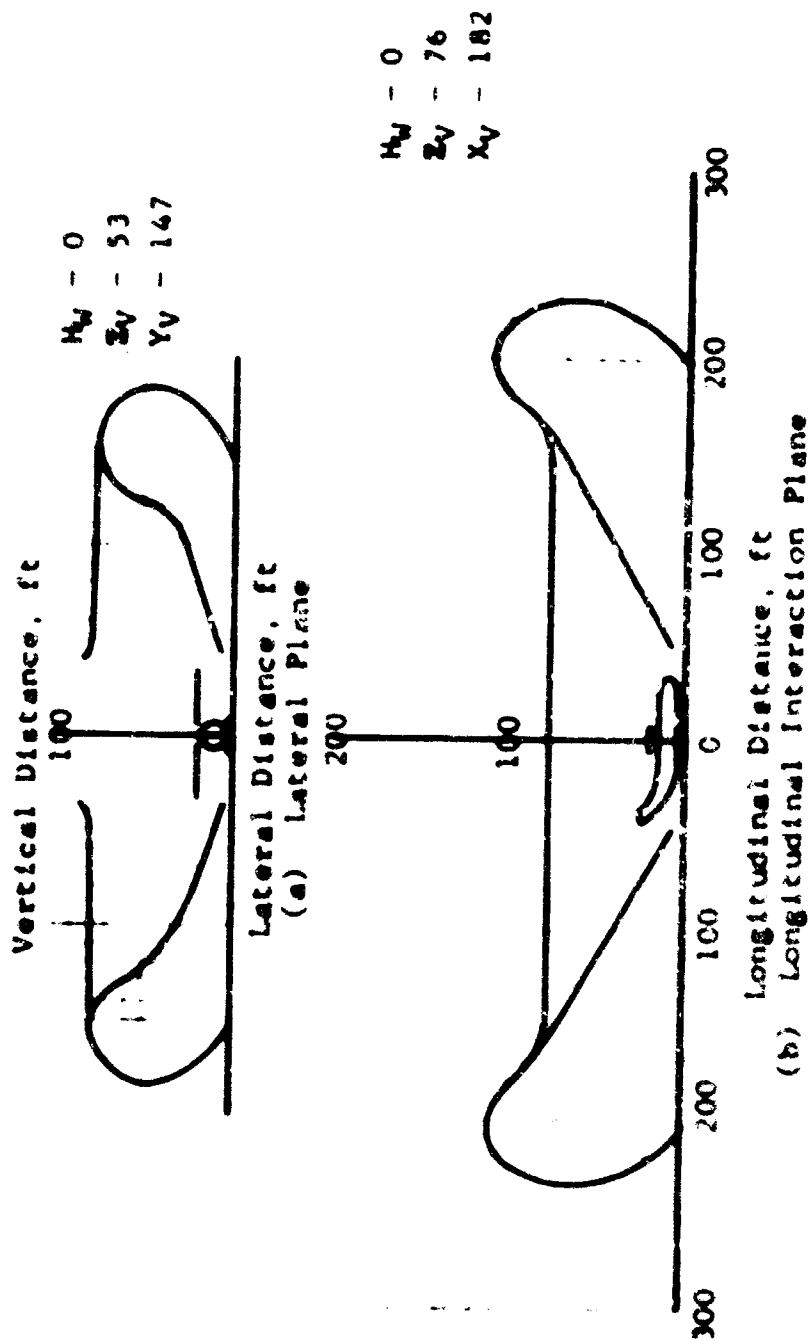


Figure 37. Dust Cloud Size and Shape for the XC-142 Aircraft.

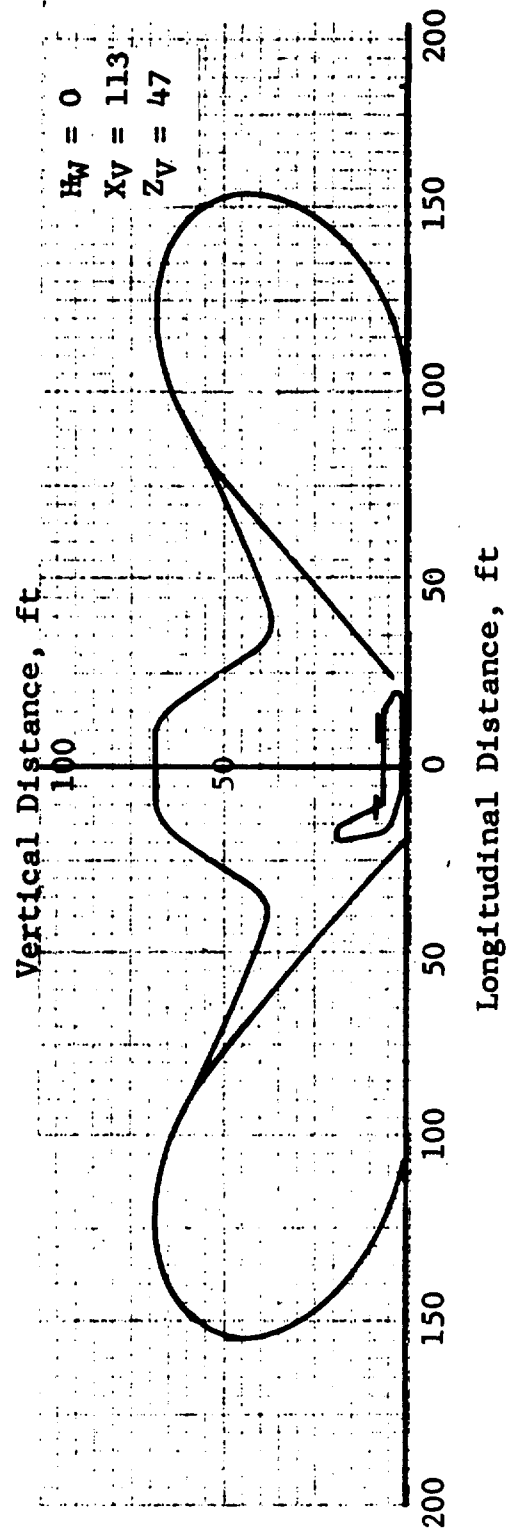


Figure 38. Dust Cloud Size and Shape for the X-22A Interaction Plane.

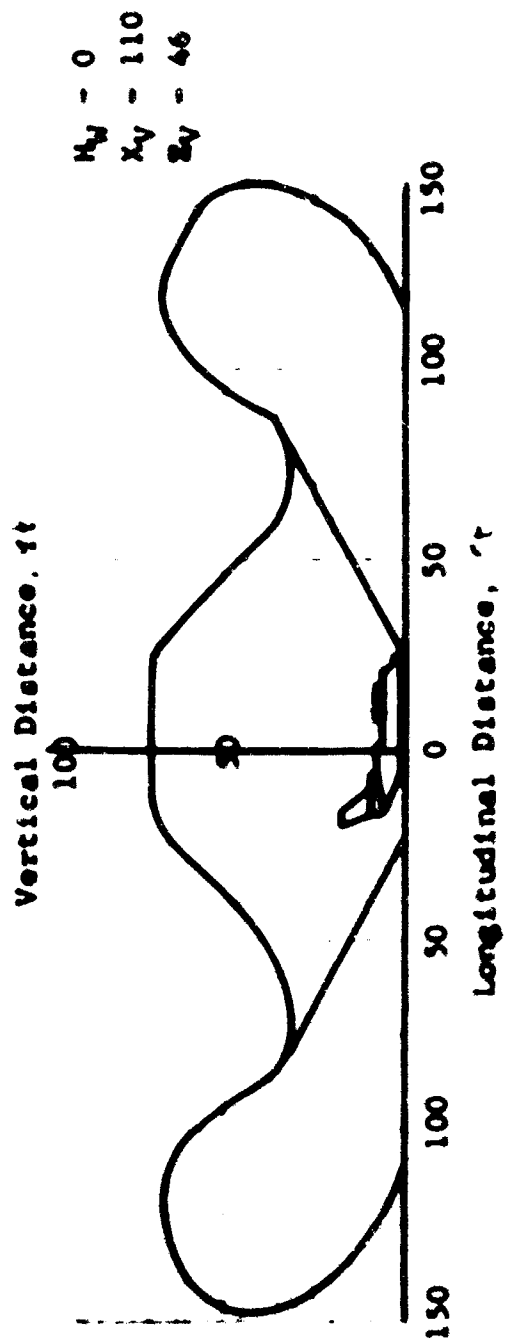


Figure 39. Dust Cloud Size and Shape for the X-19A Interaction Plane.

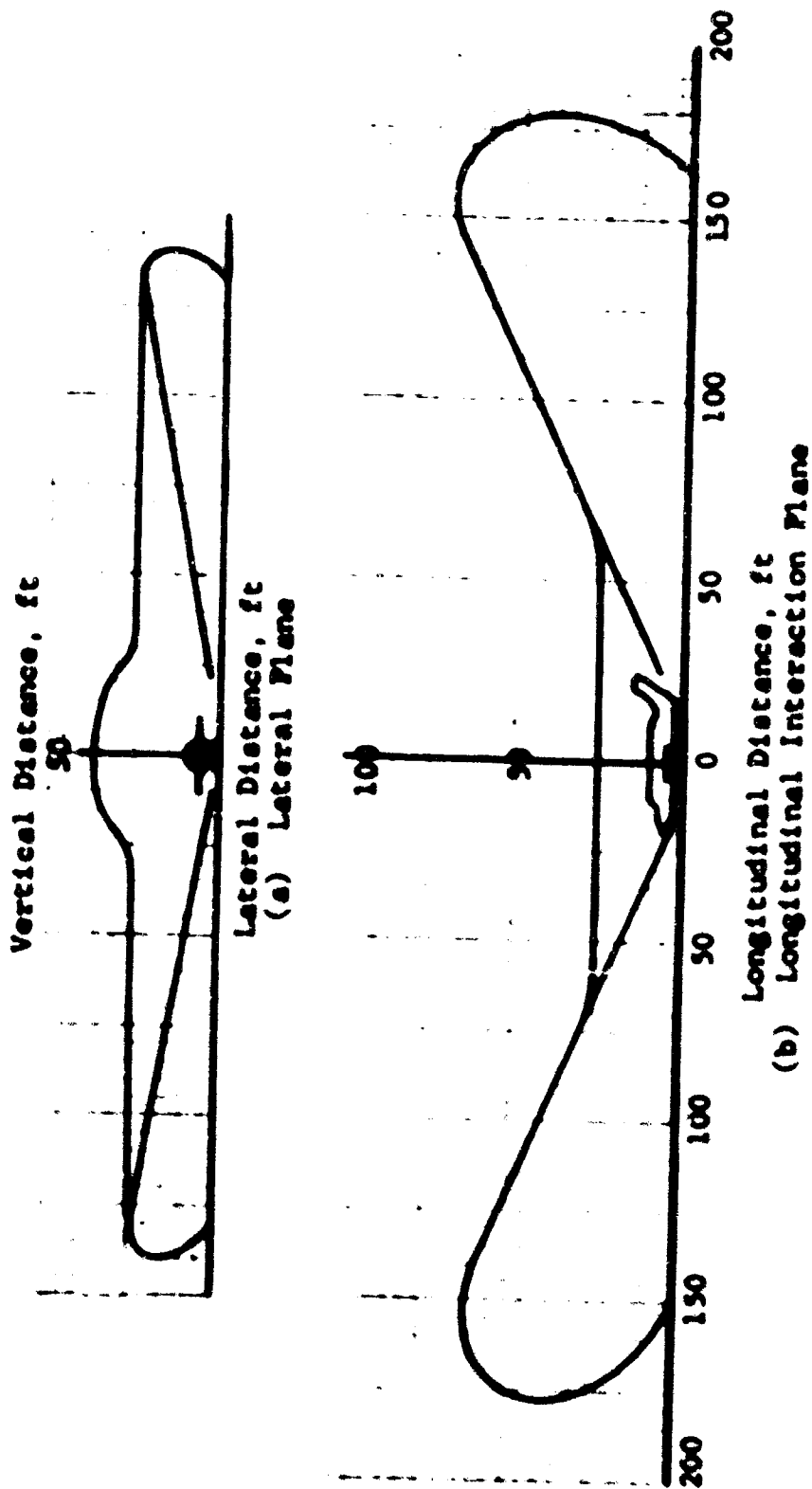


Figure 40. Dust Cloud Size and Shape for the XV-5A Aircraft.

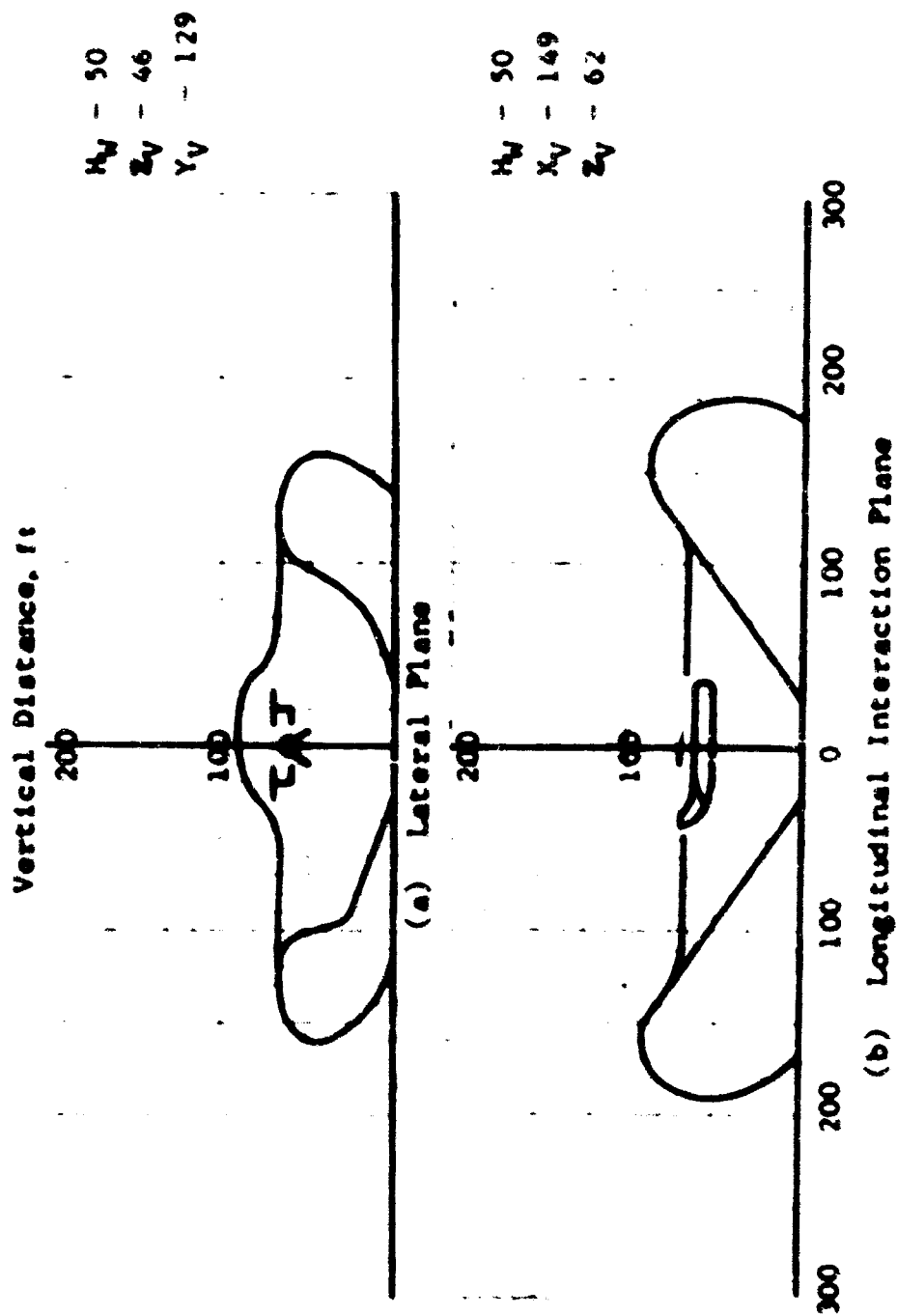


Figure 41. Dust Cloud Size and Shape for the XC-142 Aircraft.  $H_W - 50$  Feet.



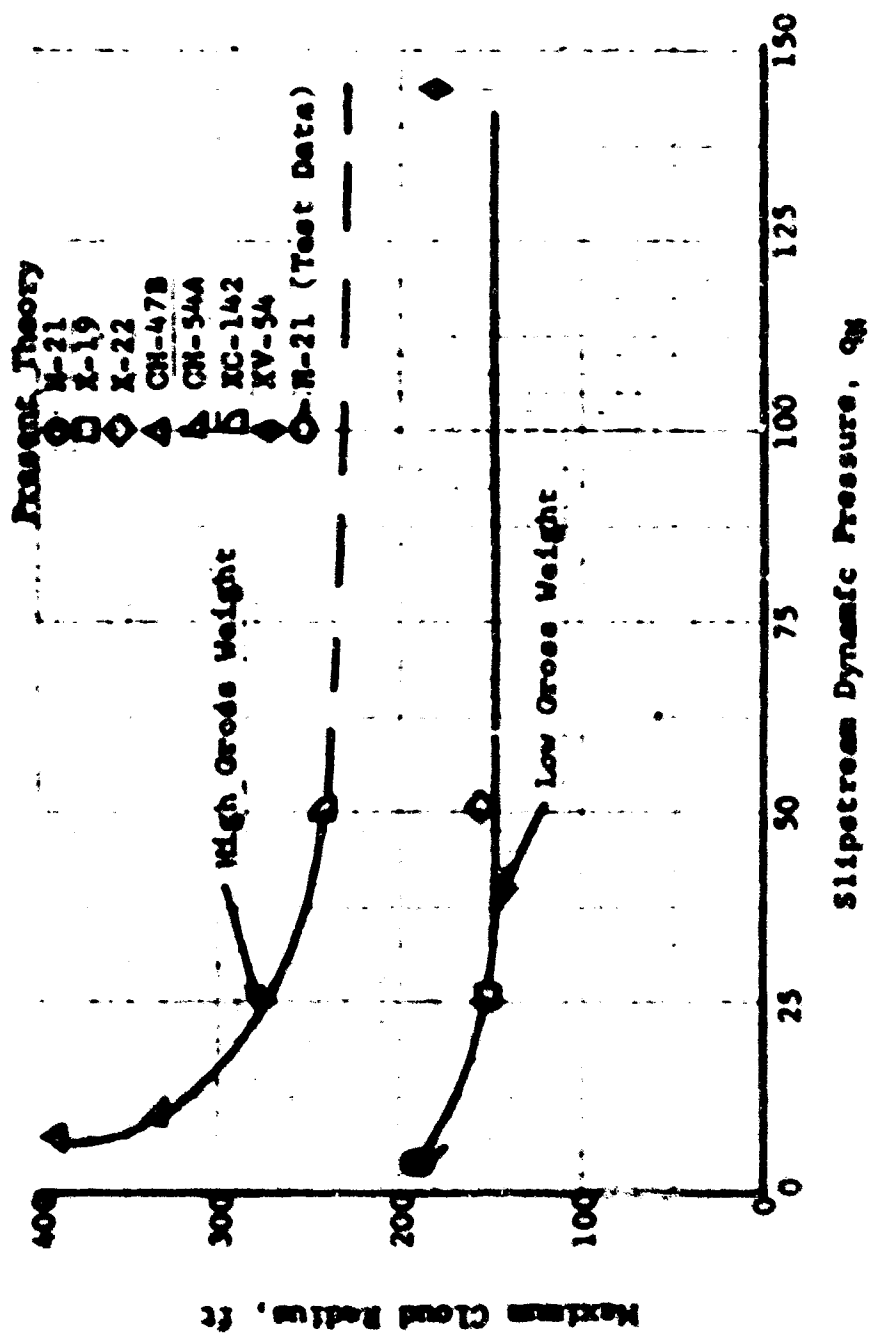


Figure 42. Maximum Boundary of Cloud versus Slipstream Dynamic Pressure for Various Aircraft.

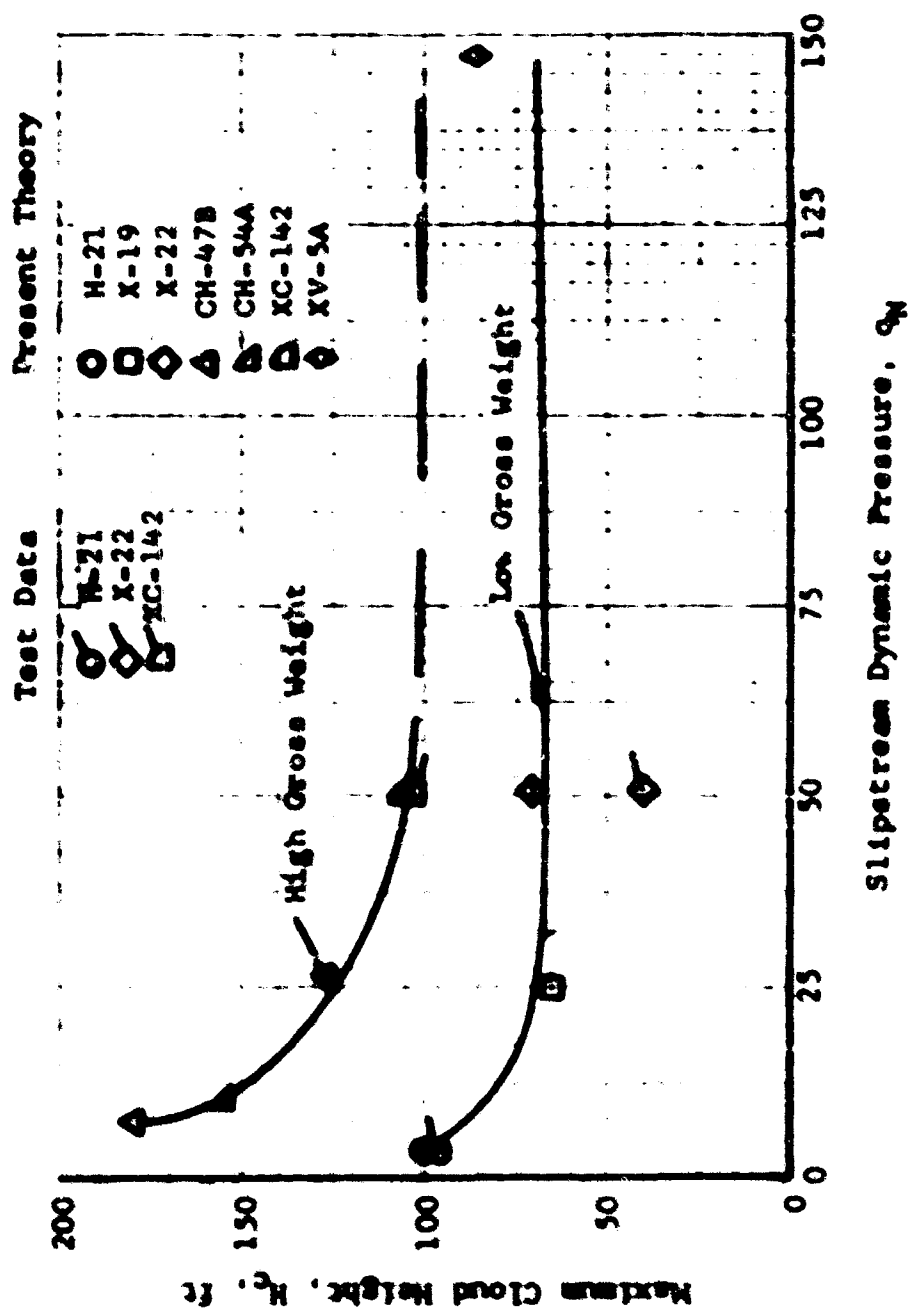


Figure 43. Maximum Cloud Height versus Slipstream Dynamic Pressure for Various Aircraft.

with Figure 41 (50 feet wheel clearance) for the XC-142 aircraft. It can be noted from these figures that for high disc loading aircraft (such as the XC-142), 25 percent reduction in cloud height and about 17 percent reduction in cloud radius is indicated for a 50 foot increase in wheel clearance from the ground.

## 2. Cloud Content

### a. Particle Density Distribution

#### (1) Far-Field Density Distribution

The far-field particle density distribution for the selected V/STOL aircraft at two radial locations,  $X = 45$  feet and  $X = 90$  feet, are presented in Figures 44 through 49. These results were obtained by first computing mass flow rate distribution and local velocities within the dust cloud using analytical techniques developed in Section II. Equation (45) was then applied to compute the corresponding density distribution. This analytical technique was checked against the test data obtained for the H-21 helicopter operating over desert sand. A comparison of the theoretical results with test data is presented in Figure 44, which shows a good correlation of the present theory with test.

From Figures 44 through 49, it can be noted that for a constant radial location, the particle density increases with a decrease in vertical distance from the ground.

Furthermore, for the radial stations closer to the rotor centerline ( $X = 45$  feet), a greater density decay rate is indicated with height from the ground as compared to that for larger radial stations ( $X = 90$  feet).

The effect of rotor height above the ground on particle density distribution for the XC-142 aircraft can be seen by comparing Figure 45

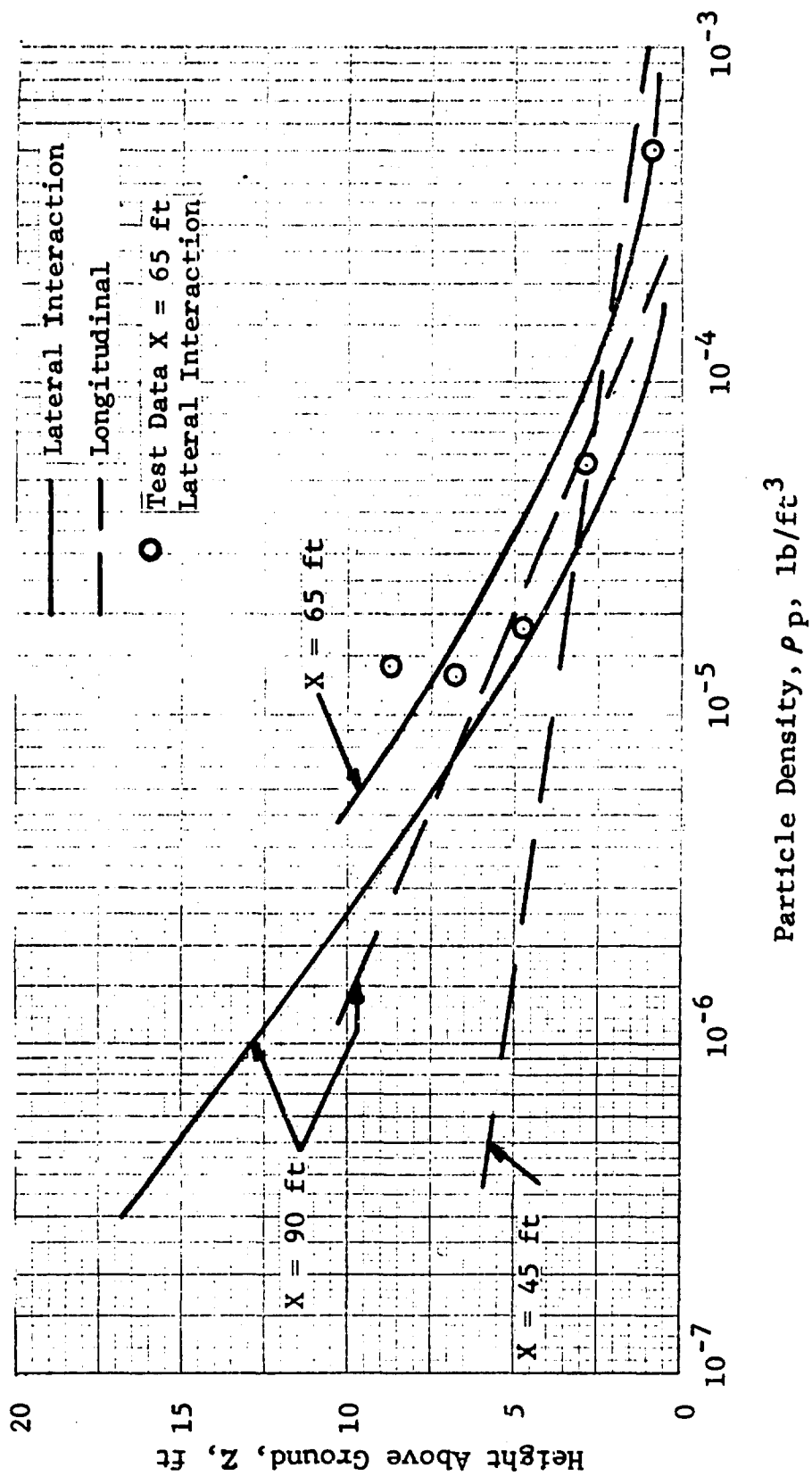


Figure 44. Particle Density Distribution for the H-21 Helicopter.

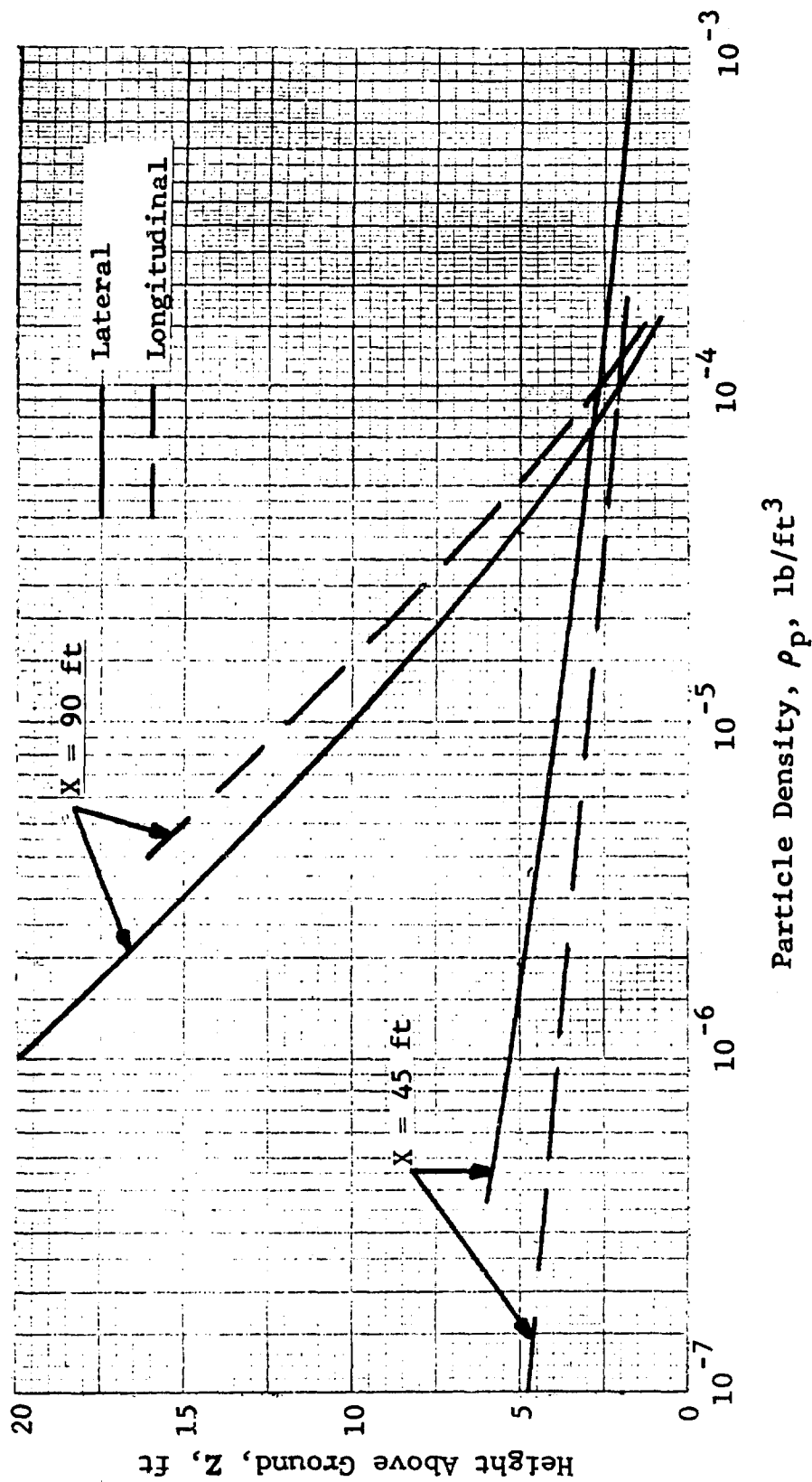


Figure 45. Particle Density Distribution for the XC-142 Aircraft.

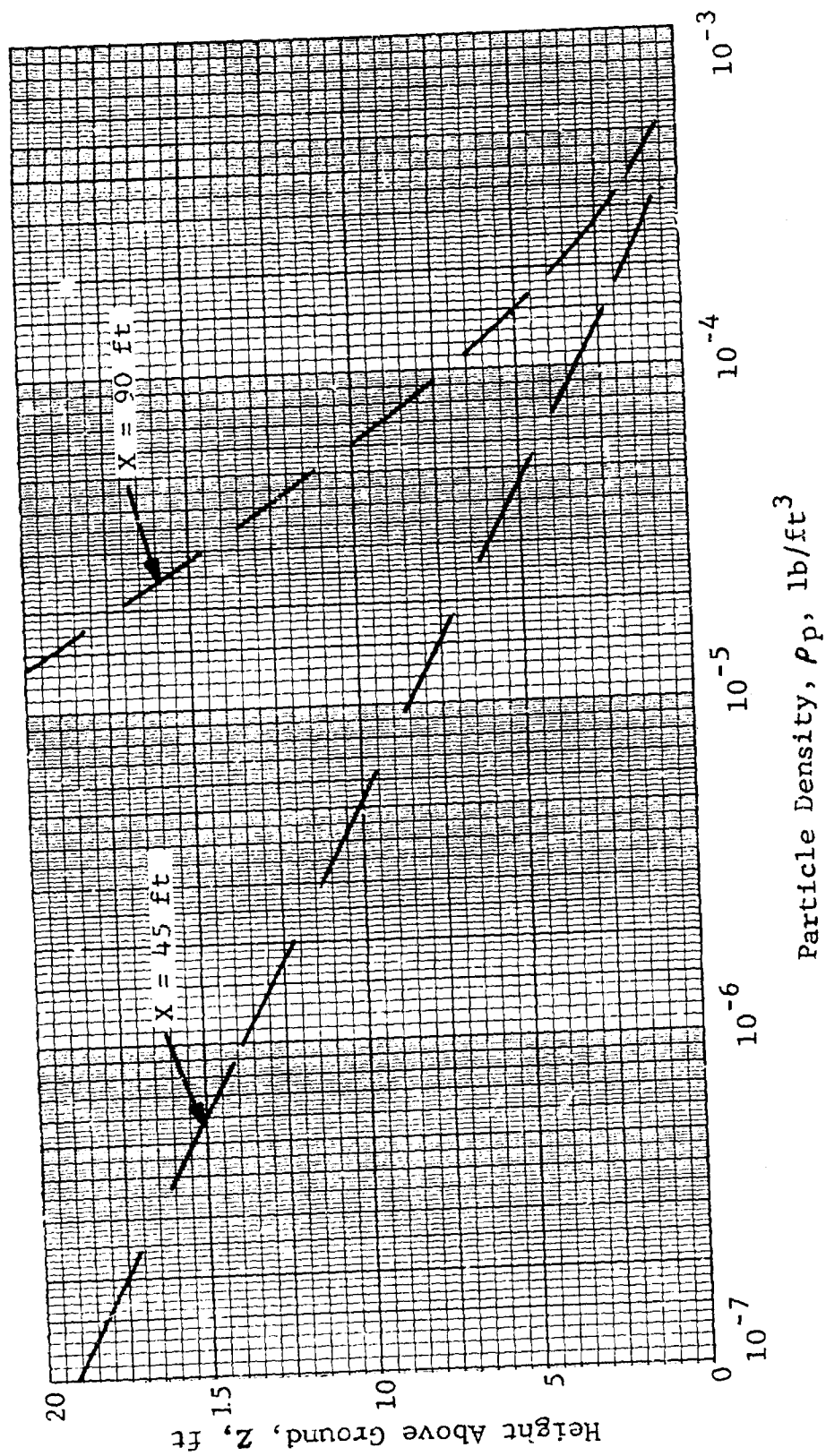


Figure 46. Particle Density Distribution for the X-22A Aircraft.

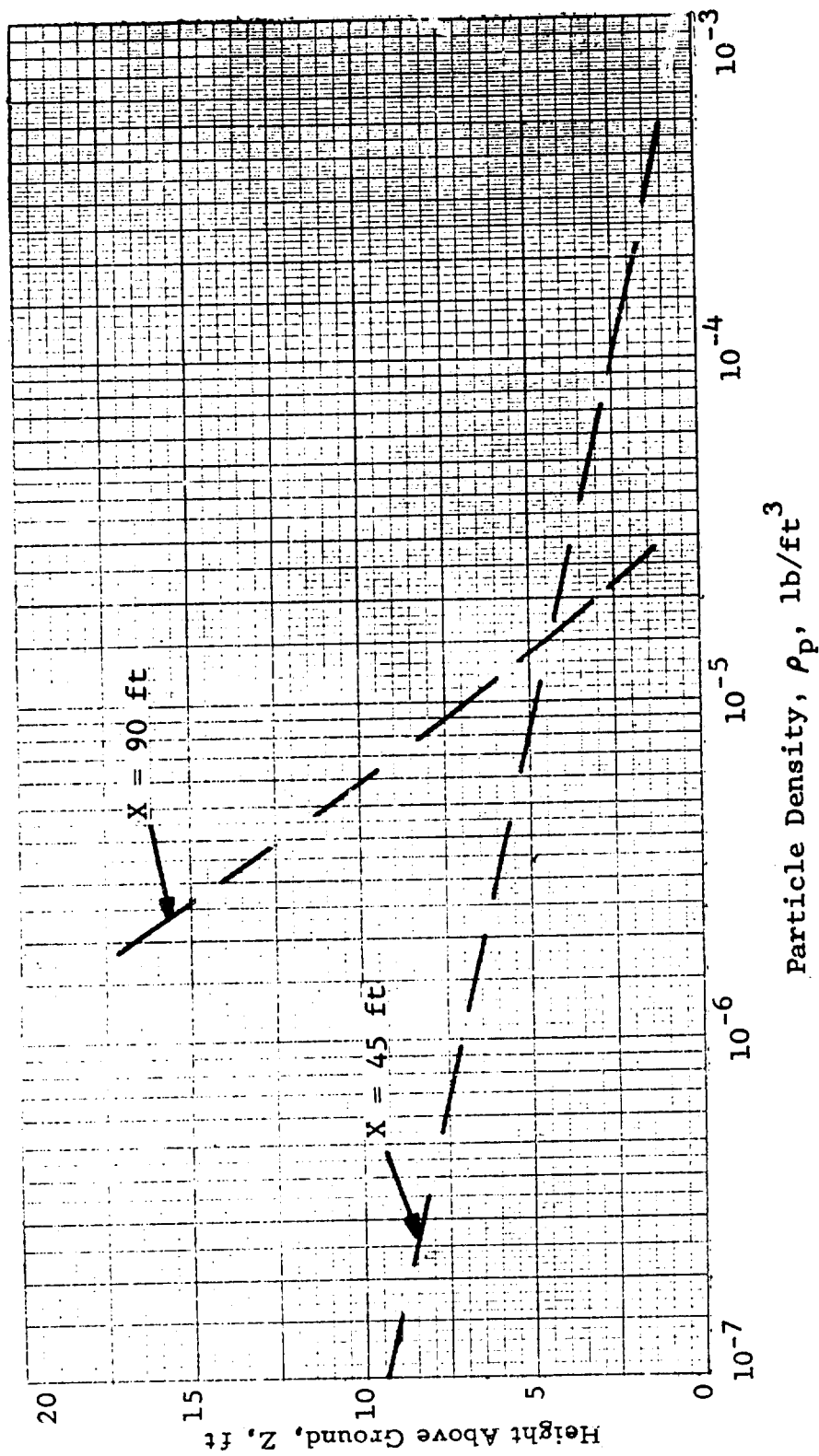


Figure 47. Particle Density Distribution for the X-19A Aircraft.

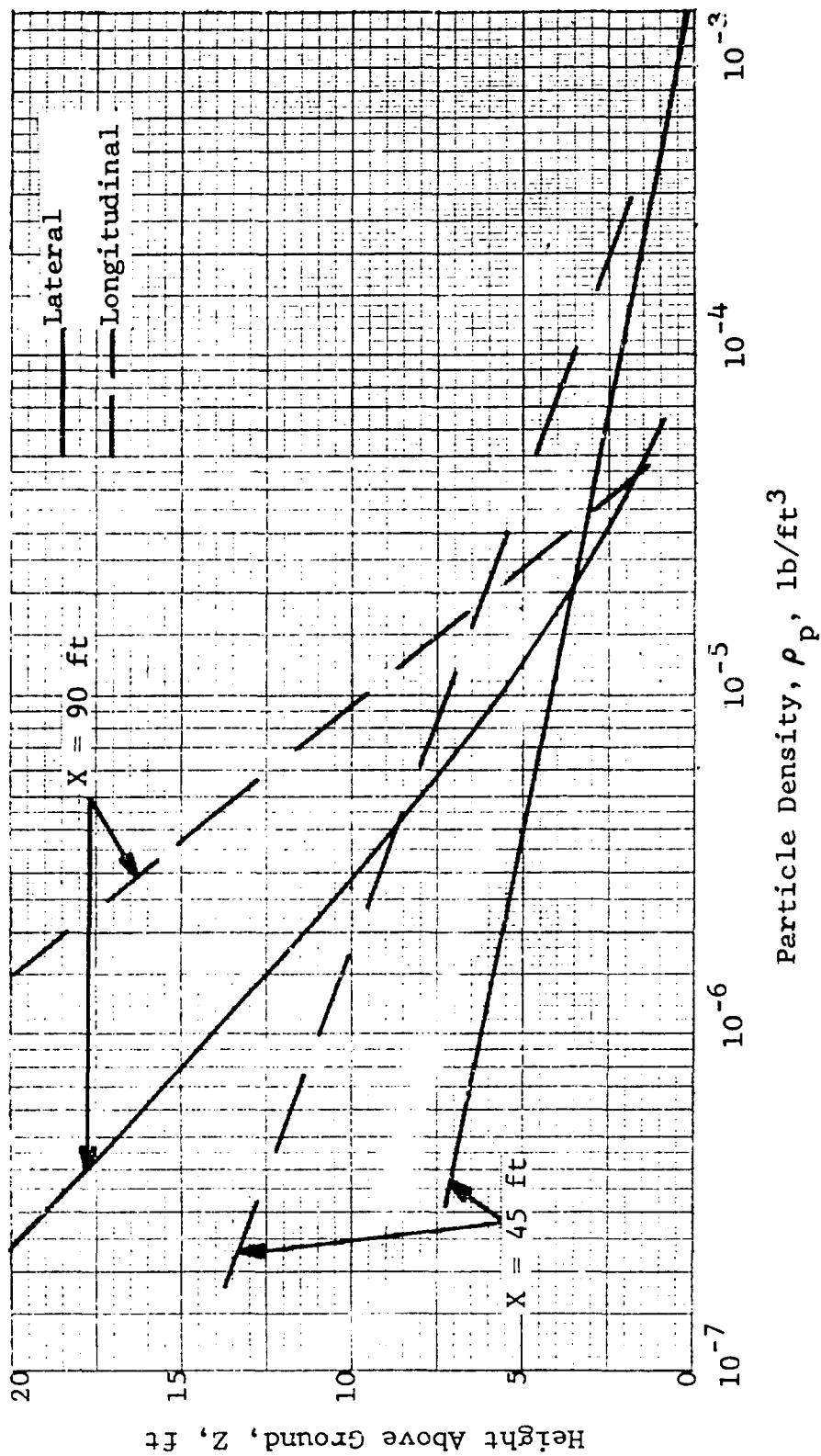


Figure 48. Particle Density Distribution for the XV-5A Aircraft.



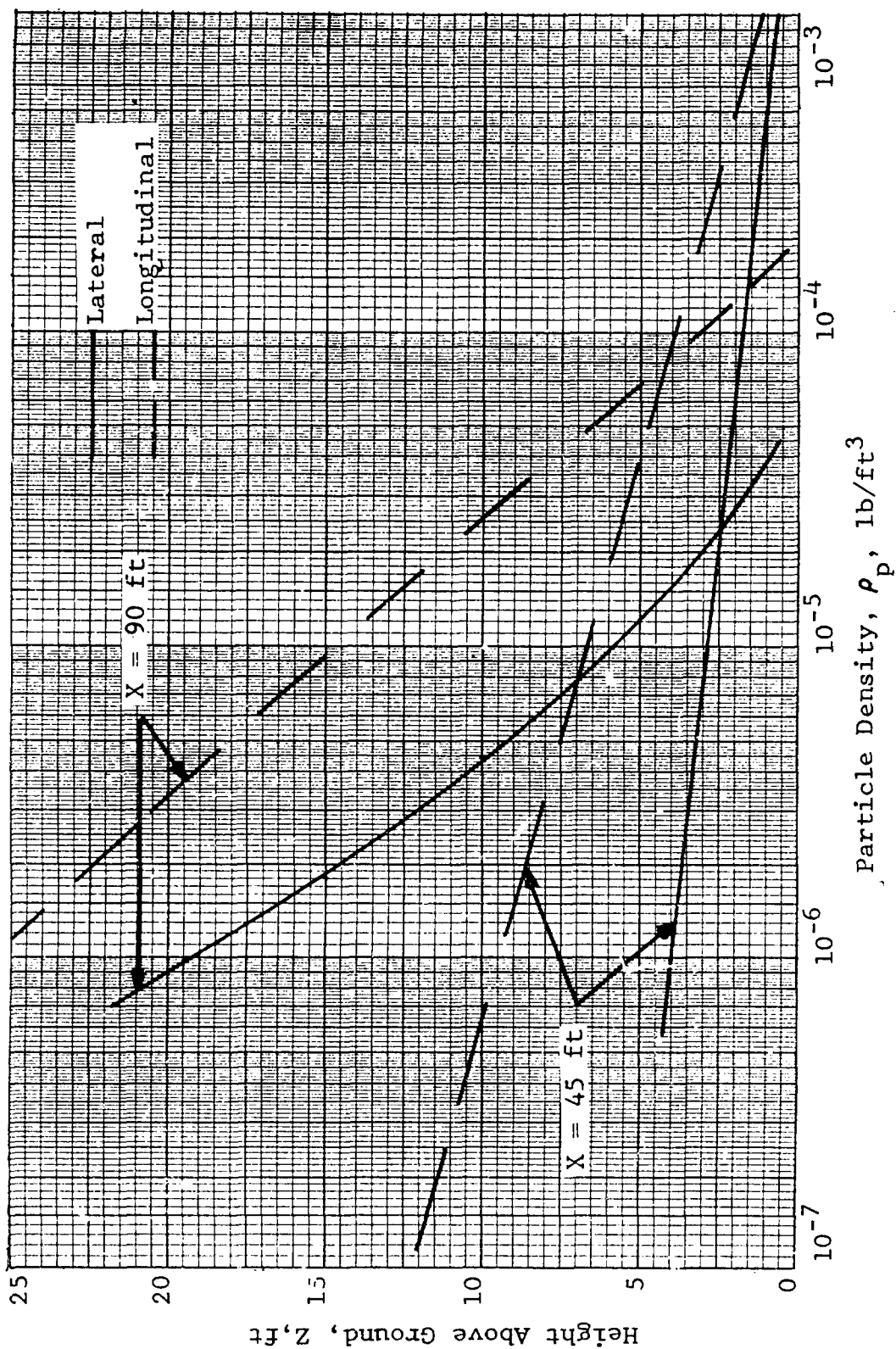


Figure 49. Particle Density Distribution for the XC-142 Aircraft,  $H_W = 50$  Feet.

(zero wheel clearance) with Figure 49 (50 feet wheel clearance). It can be noted from these figures that particle density decreases as the aircraft lifts off the ground.

(2) Near-Field Density Distributions

As discussed previously, the near-field particle density distributions at or below the rotor disc (within the vortex cylinder) were computed utilizing the flow continuity concept within a given flow stream tube. The results thus obtained for the selected V/STOL aircraft are presented in Table IV, which also contains the pertinent test data.

It can be noted from this table that the predicted particle densities are generally higher along the interaction planes of multi-rotor configurations than along other locations in the close vicinity of rotor planes. Furthermore, the magnitudes of the predicted particle densities generally fall between the maximum and minimum values obtained from the tests for various V/STOL aircraft.

b. Particle Size Distributions

The particle size distributions for the selected V/STOL aircraft were computed based on the specified ground sample size profile.

This ground sample, together with the airborne particle size profile at the rotor planes for the selected V/STOL aircraft, is presented in Figure 50.

It can be noted from this figure that the airborne particle size (at the rotor plane) for the XC-142, X-22A, and XV-5A aircraft is not much different from the ground sample profile. This implies that practically all size particles present in the ground sample will be airborne as a result of the downwash velocities generated by these aircraft.

TABLE IV		
PREDICTED AND MEASURED AVERAGE PARTICLE DENSITIES IN THE CLOSE VICINITY OF ROTOR PLANES FOR THE SELECTED AIRCRAFT		
a. <u>Predicted Particle Densities at the Rotor Plane</u>		
Aircraft	Densities (mg/ft <sup>3</sup> )	
	Lateral Plane	Longitudinal Plane
H-21	19.75	4.15
XC-142	5.5	35.4
X-22A	-	62.96
X-19A	-	17.2
XV-5A	-	44.9
XC-142 (50 ft wheel clearance)	1.96	4.4
b. <u>Measured Particle Densities in the Close Vicinity of the Rotor Plane</u>		
Source of Test Data	Densities (mg/ft <sup>3</sup> )	
	Maximum	Minimum
Full-scale dual tandem test rig, two Lycoming T-53 engines (Reference 21)	31	--
KAC mock-up of X-22 at engine intakes (Reference 22)	85	--
Kaman HTK helicopter (Reference 20)	8.0	2.7
Kaman HTK helicopter hovering near an HOK helicopter (Reference 20)	24.5	5.4
Vertol Model 107 helicopter (Reference 23)	7.5	1.0
H-21 at Yuma (Reference 15)	31 64	2.8

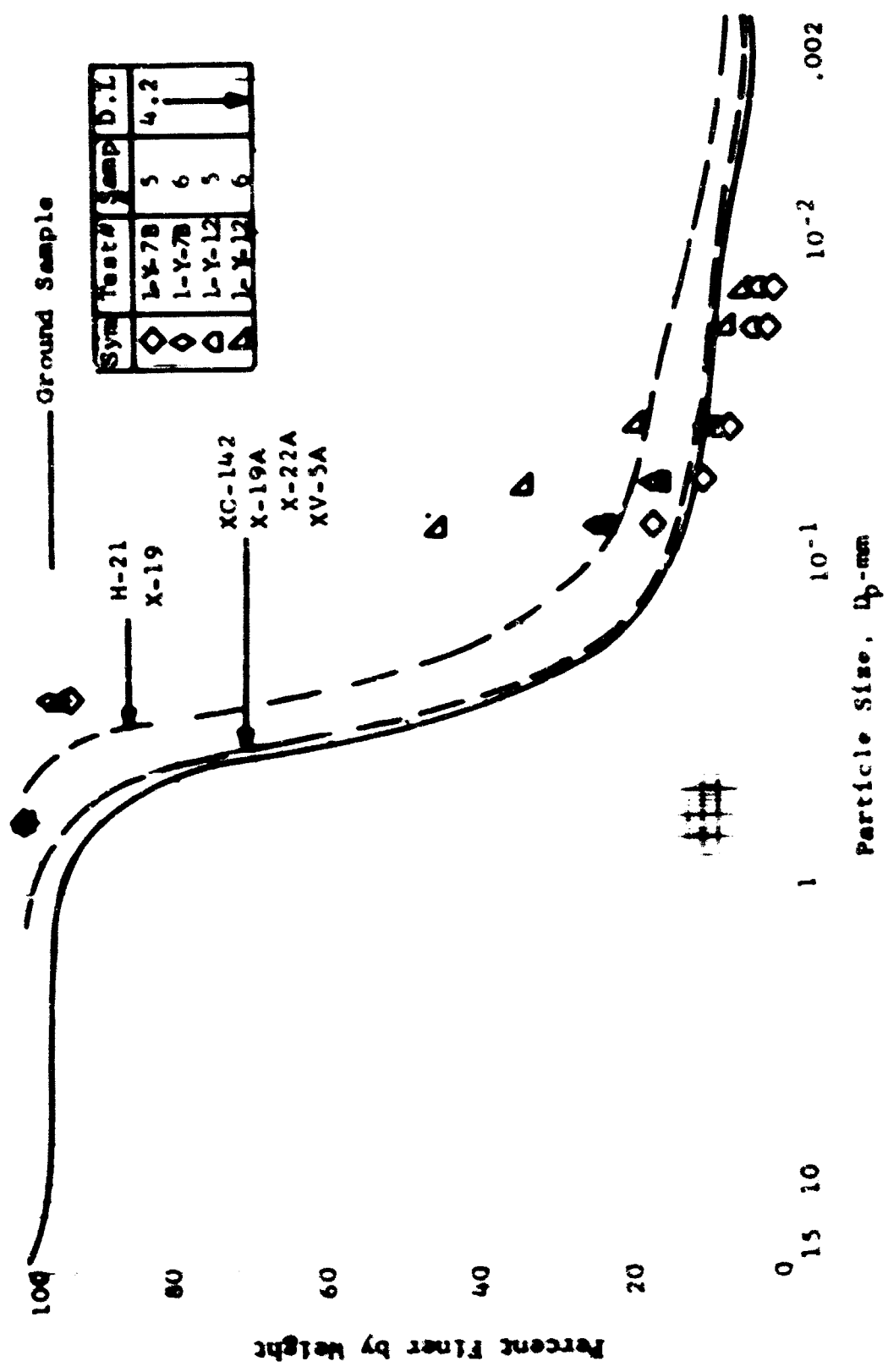


Figure 30. Particle Size Profiles (Ground Sample and the Airborne Sample at the Rotor Plane) for Various Aircraft.

The corresponding airborne particle sizes for the H-21 and X-19A aircraft are appreciably smaller than the ground sample sizes.

Figure 50 also contains the test data obtained from Reference 15 for the H-21 helicopter. In general, good correlations are indicated between the predicted and measured particle sizes. More detailed information on these tests is presented in the appendix.

The maximum and mean (50 percent finer by weight) particle size distributions for the H-21, XC-142, and XV-5A are presented in Figures 51, 52, and 53, respectively.

These figures show the variation of particle size (diameter in mm) with height above the ground for constant radial locations of  $X = 45$  feet and  $X = 90$  feet.

It can be noted from these figures that for a constant radial location, the maximum size of particles reduces with increasing height. Also, for a constant height above the ground (e.g., 7 feet), larger maximum size particles can be found further away from the aircraft ( $X = 90$  feet). This latter trend is a function of aircraft disc loading, height above the ground, and aircraft geometry; it may reverse depending on the combinations of these parameters (e.g., see Figure 51 for heights of less than 5 feet above the ground).

#### c. Effect of Terrain

The rotor downwash signatures thus far discussed are strongly dependent on the type of terrain and the dynamic pressure generated by the lifting aircraft.

As reported in Reference 9, the point of incipient erosion for any terrain can be related to the aircraft's disc loading; thus, the criteria under which the rotor downwash will create a dust cloud for a given terrain can be established. The data

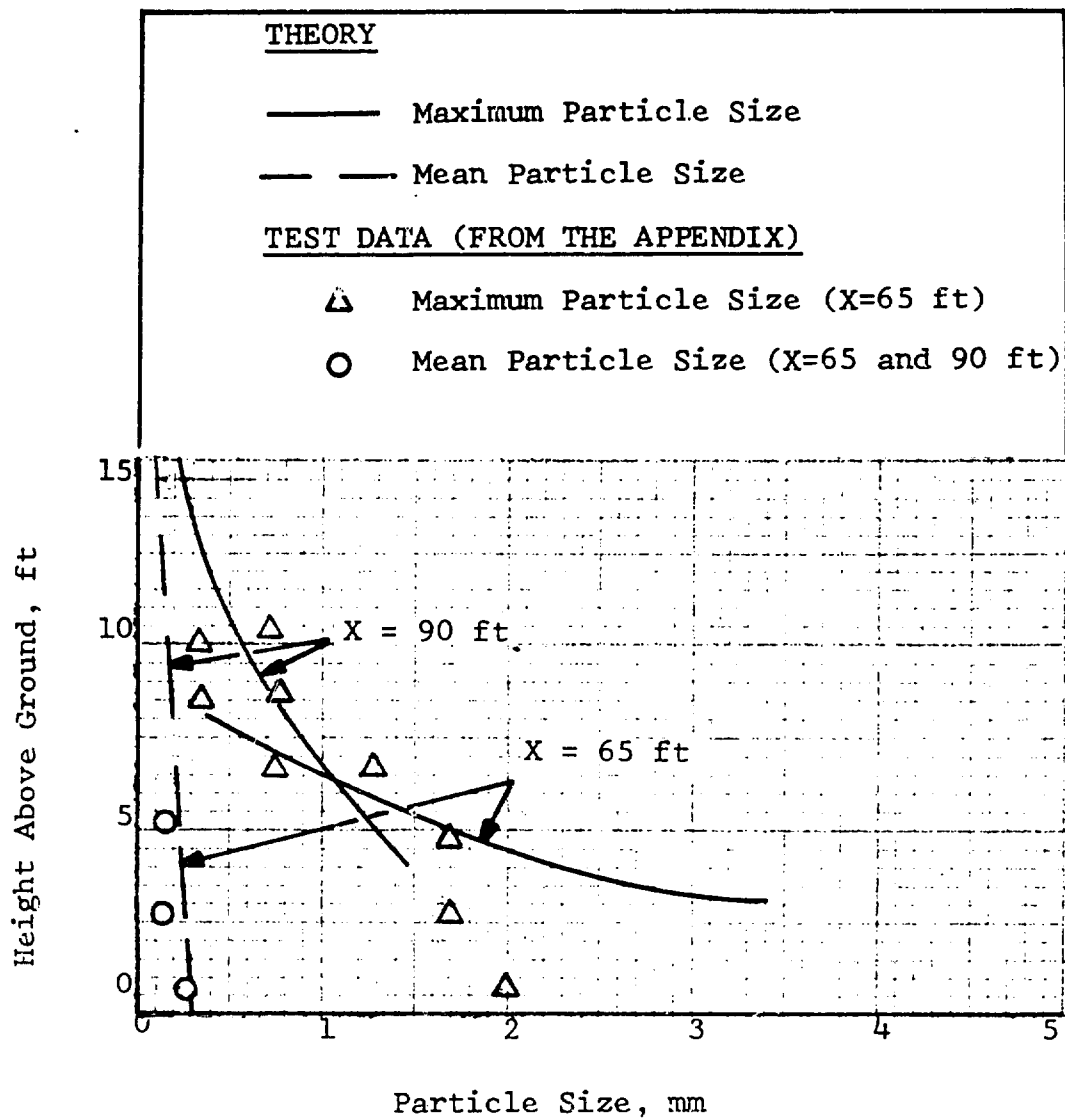


Figure 51. Particle Size Distributions for the H-21 Aircraft.

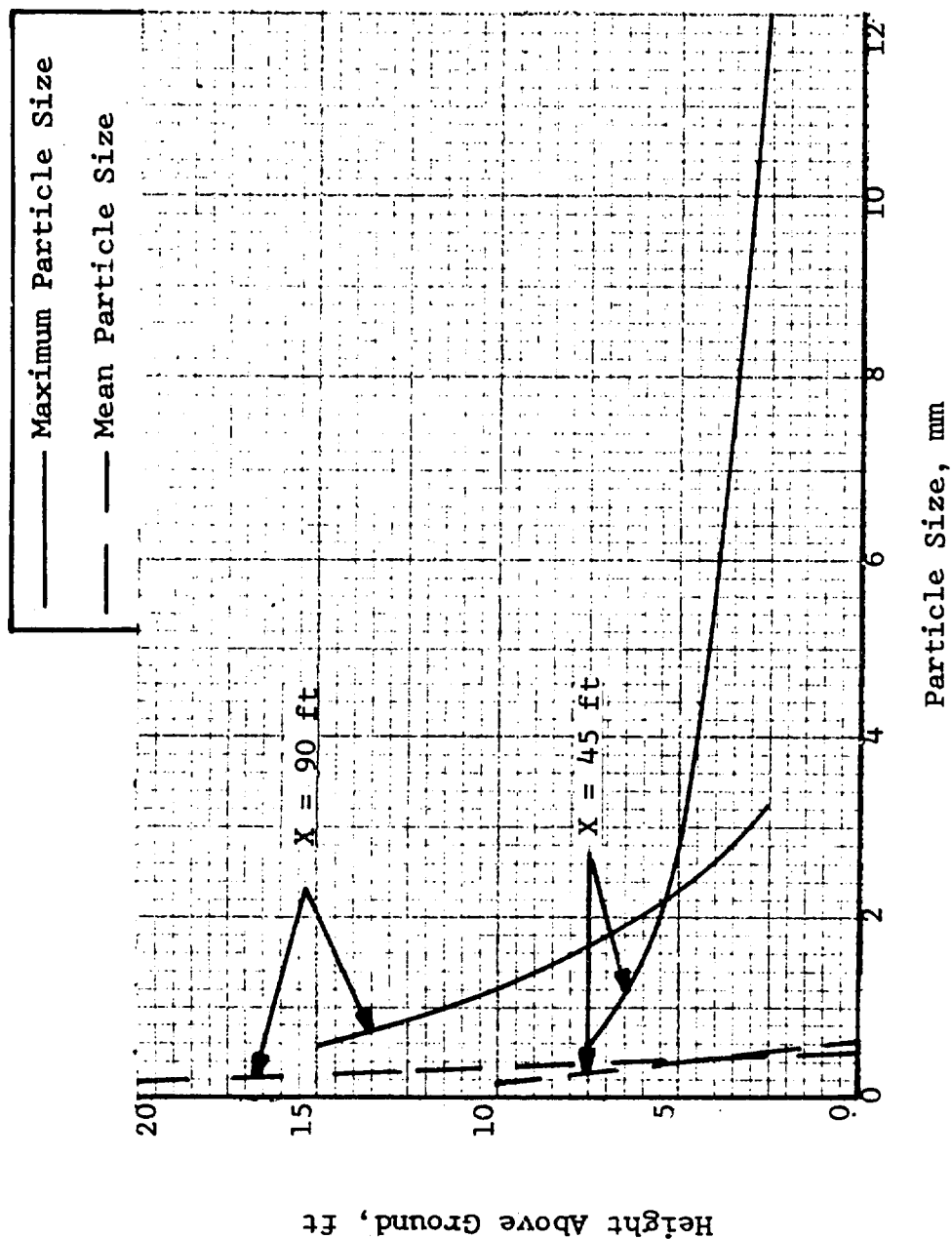


Figure 52. Particle Size Distributions for the XC-142 Aircraft.

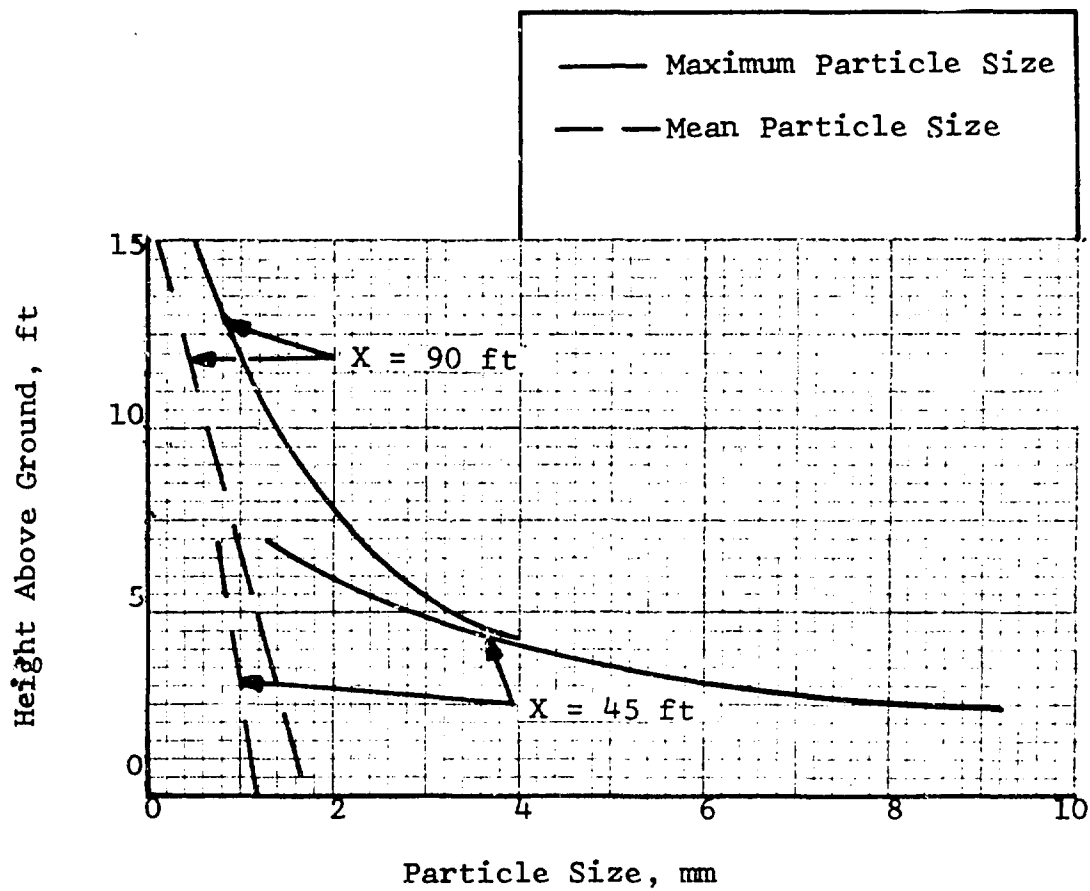


Figure 53. Particle Size Distributions for the XV-5A Aircraft.



for the incipient erosion of various terrains as presented in Reference 9 are summarized in Figure 54. As can be noted from this figure, terrains such as silty sand or water can be eroded by all aircraft considered in this study; crushed stone, plowed earth, or soaked sand will be eroded only by the XC-142 or X-22A; and packed lean clay will be eroded only by the XV-5A.

### C. DOWNWASH SIGNATURE EFFECTS

Presented in this section are the results of the effects of rotor downwash environment on pilot's visibility, engine, ground equipment and personnel.

#### 1. Pilot's Visibility

The computations of pilot's visibility as affected by the dust cloud were performed assuming the object and background light intensities in the uncontaminated atmosphere of  $I_s = 0.2$  foot-lambert and  $I_o = 0.1$  foot-lambert, respectively.

In addition, the aircraft heading relative to the object was taken as 45 degrees along the pilot's line of sight. Although the prime concern in pilot's visibility through a dust cloud is an unimpaired ground reference, the reduction in pilot's visibility is herein computed in terms of light transmittance (T) as a function of object height above the ground.

The results which were obtained for the five selected V/STOL aircraft are presented in Figures 55 through 60, which show a reduction of light transmittance with reduction in object height. This trend occurs due to an increase in particle density and cloud penetration distance as object height from the ground is reduced. For a constant object height, the variation of light transmittance with horizontal distance from the pilot to the object depends on the dust cloud characteristics and aircraft geometry (e.g., compare Figure 55 with Figure 58).

For direct comparison of loss of pilot's visibility from various V/STOL aircraft, the light transmittance results

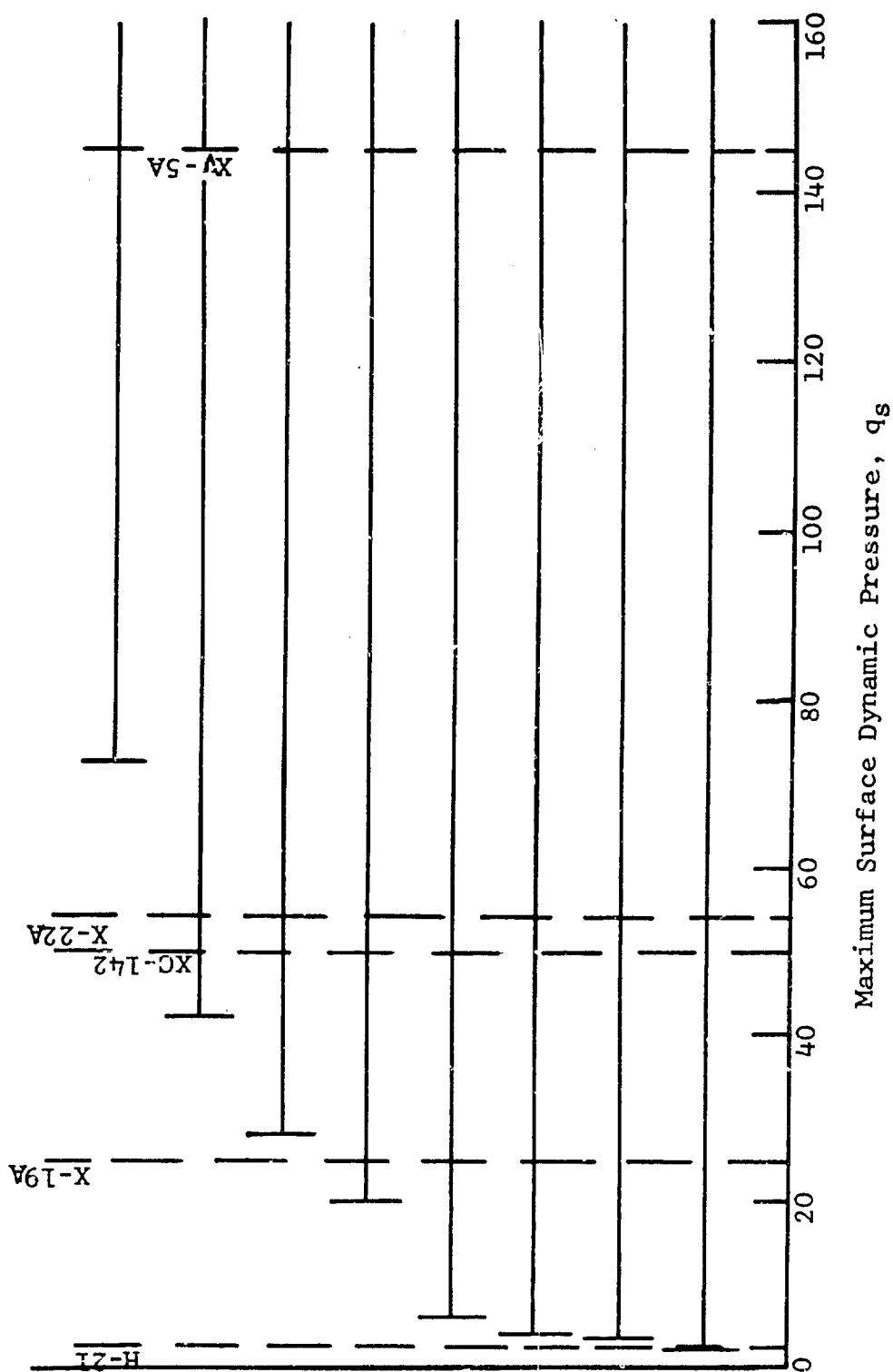


Figure 54. Variation of Incipient Erosion With Terrain.

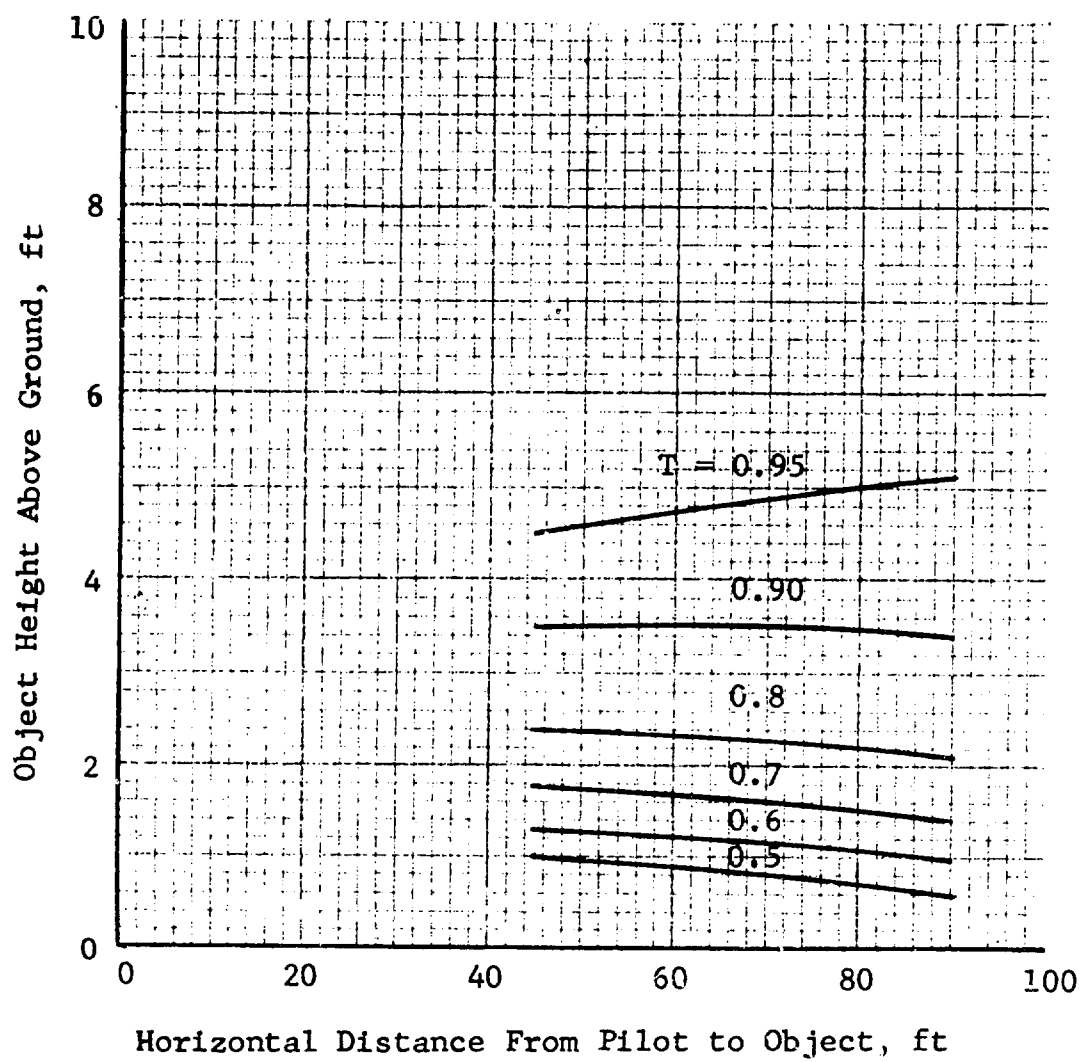


Figure 55. Light Transmittance for the H-21 Aircraft.  
Wheels on Ground,  $\psi = 45^\circ$ .

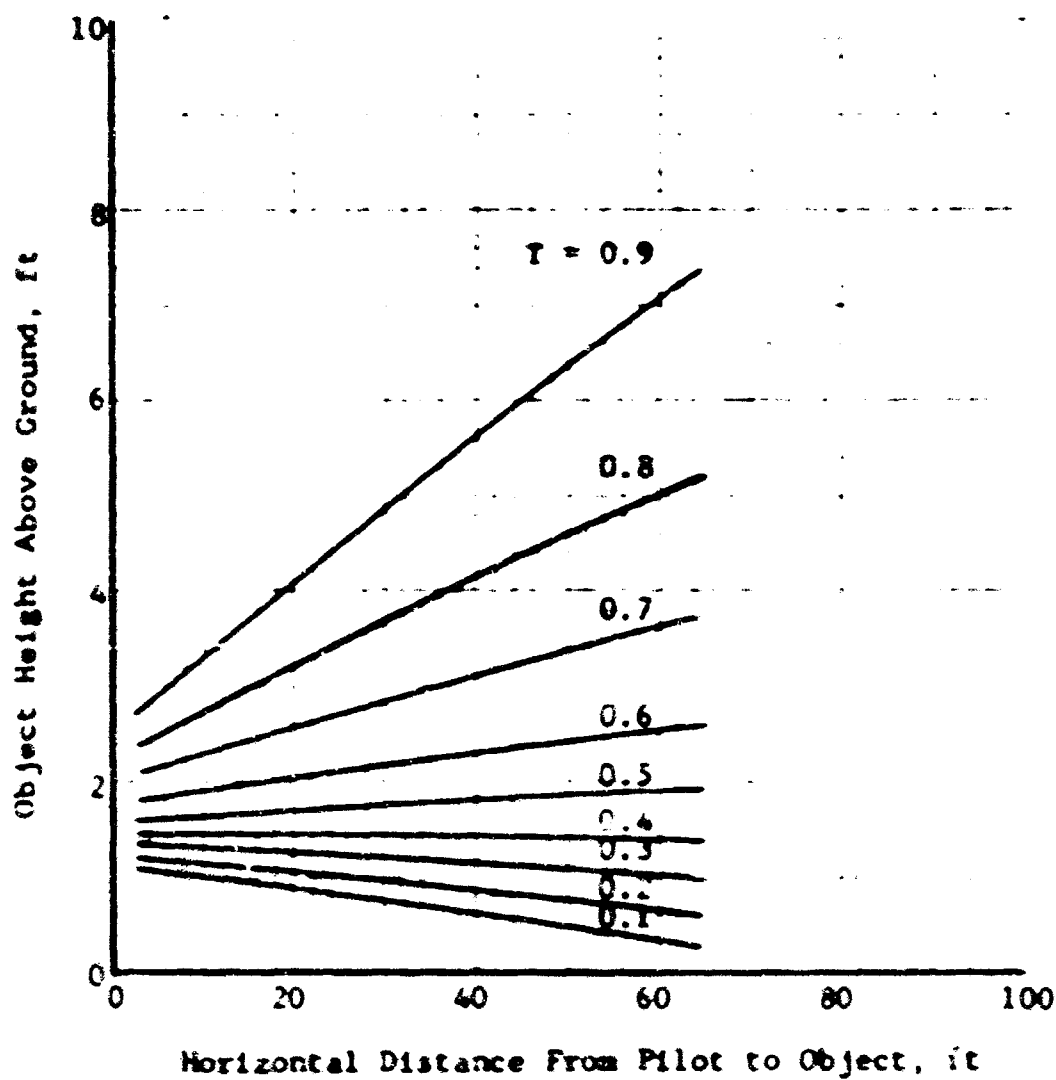


Figure 56. Light Transmittance for the XC-142 Aircraft.  
Wheels on Ground,  $\psi = 45^\circ$ .

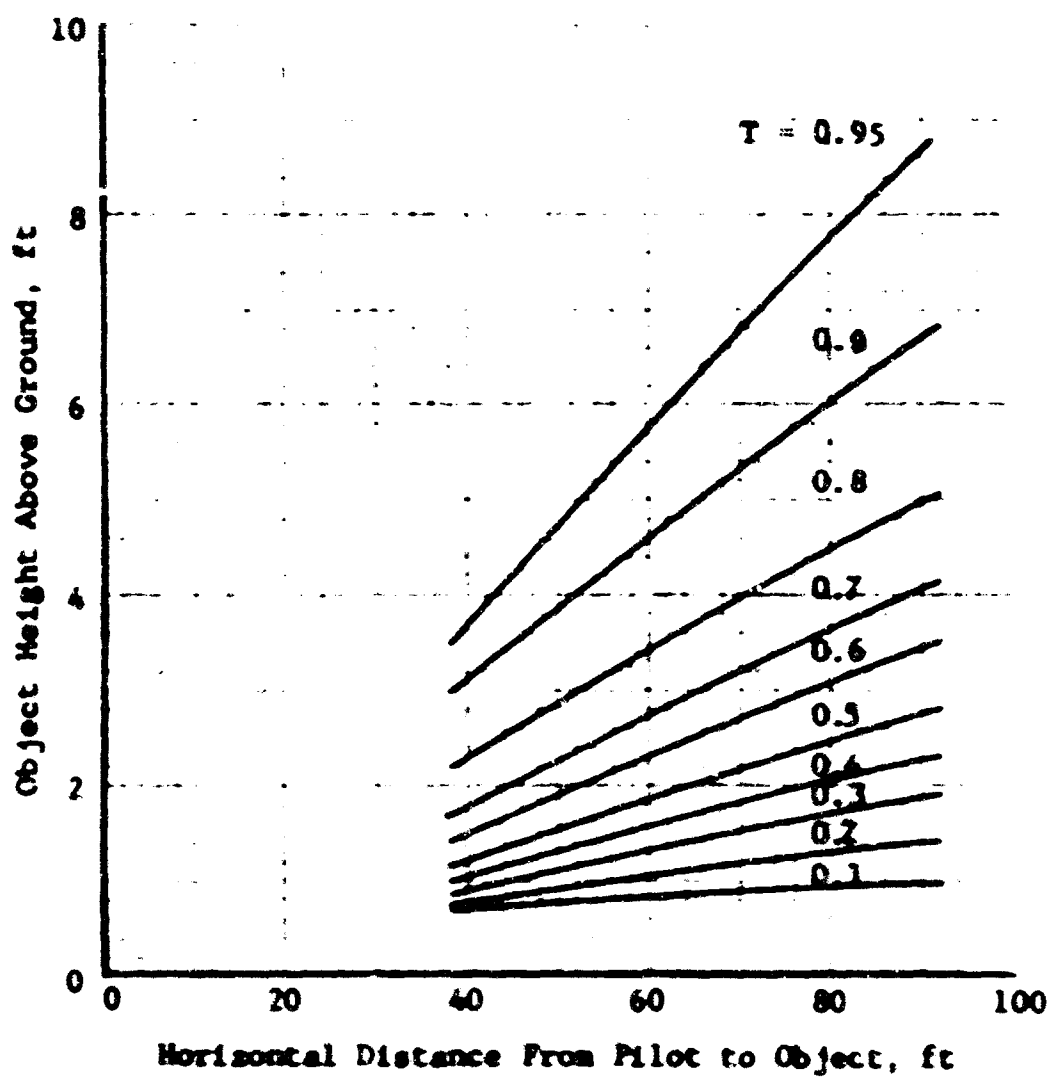


Figure 57. Light Transmittance for the X-22A Aircraft. Wheels on Ground,  $\psi = 45^\circ$ .

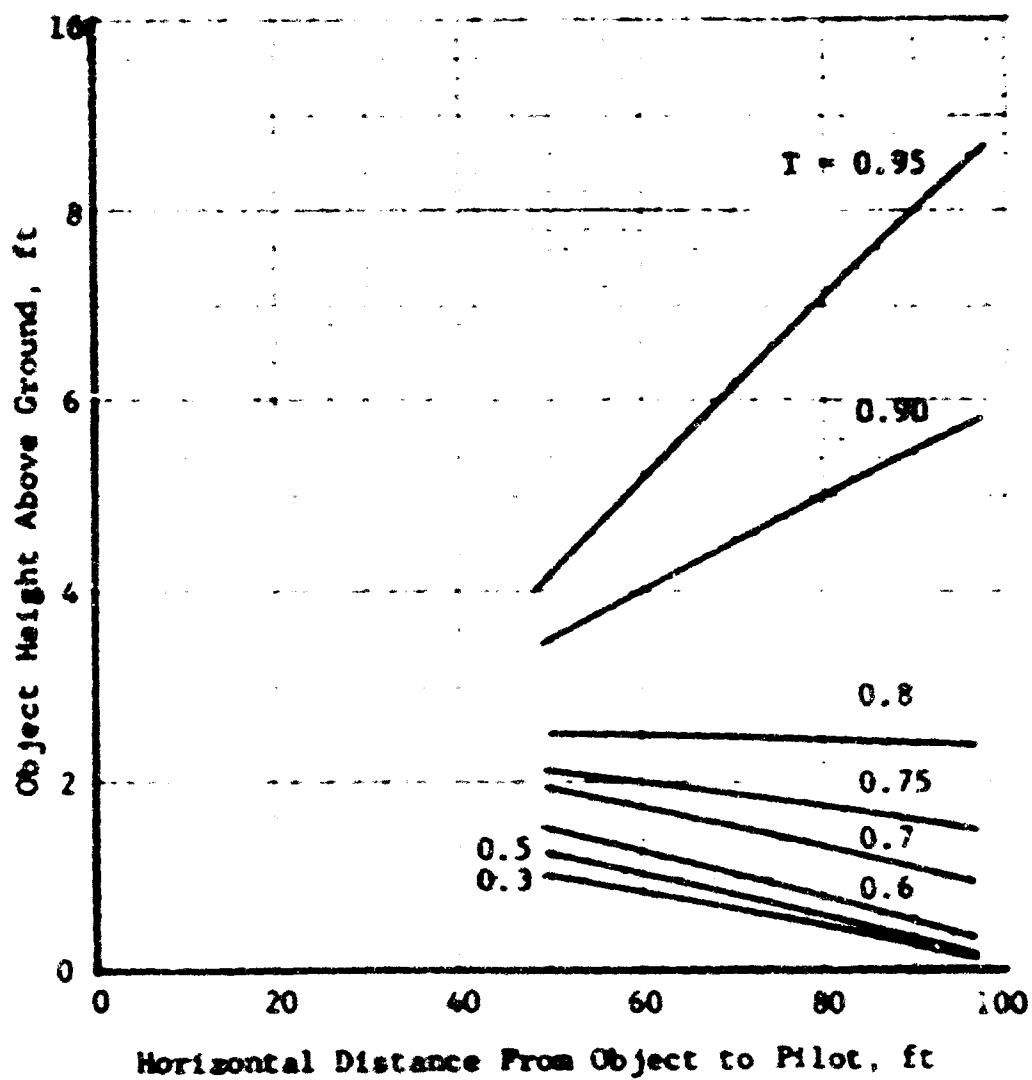


Figure 58. Light Transmittance for the X-19A Aircraft.  
Wheels on Ground,  $\psi = 45^\circ$ .

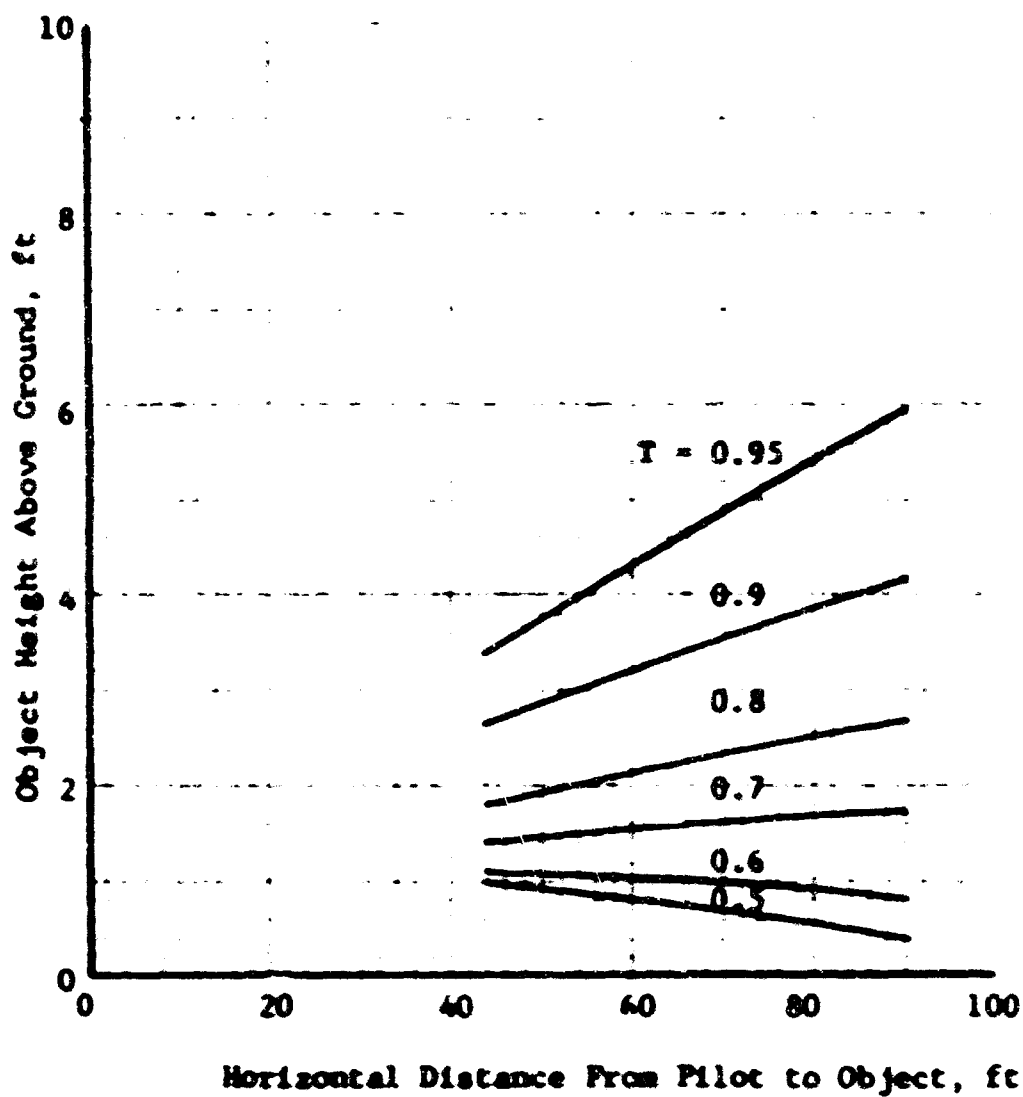


Figure 59. Light Transmittance for the XV-5A Aircraft.  
Wheels on Ground,  $\psi = 45^\circ$ .

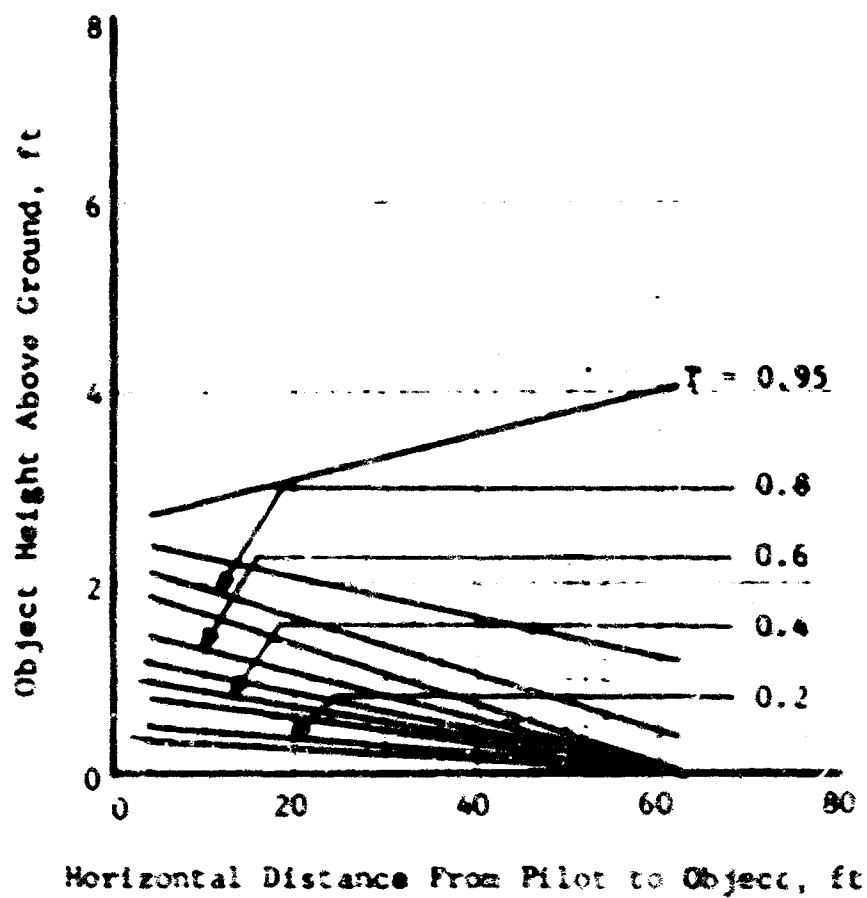


Figure 60. Light Transmittance for the X-142 Aircraft.  
Wheels on Ground, Wheel Height = 50 Feet.



(Figures 55 through 60) were utilized to compute minimum perceivable object size for 1 foot object height above the ground. These results, together with the uncontaminated atmosphere data, are presented in Figure 61. In general, Figure 61 shows an order of magnitude reduction in pilot's visibility due to the dust cloud for all aircraft as compared to the visibility in uncontaminated atmosphere. Variations of visibility for specific aircraft are functions of aircraft disc loading, gross weight, and orientation of the pilot with respect to the sighted object. The latter variable affects both the depth of penetration in the cloud ( $d$ ) and the distance to the object ( $S_h$ ). Both of these parameters are important in determining the minimum perceivable object size. Effect of distance from the pilot to the object is demonstrated in Figure 61 by comparing the results of perceivable object size for the XC-142 aircraft for zero and 50 feet wheel clearance. Even though particle density close to the ground is significantly higher for zero wheel clearance than for 50 feet height, the visibility in terms of object size is better at lower height due to the reduced distance,  $S_h$ .

## 2. Engine Damage

Another significant effect of downwash signatures is that on engine damage. The discussion presented below outlines the types of damage to engine components and the resulting effects on engine performance. Also, the effects of sand and dust filtration on extending engine life and improving engine performance are discussed.

### a. Damage of Engine Components

Based on the test data presented in References 22 through 27, the following types of turbine engine damage have been incurred by operation of various types of engines in a sand and dust environment:

- (1) Compressor blade leading edge bending and peening.
- (2) Compressor blade trailing edge rounding.

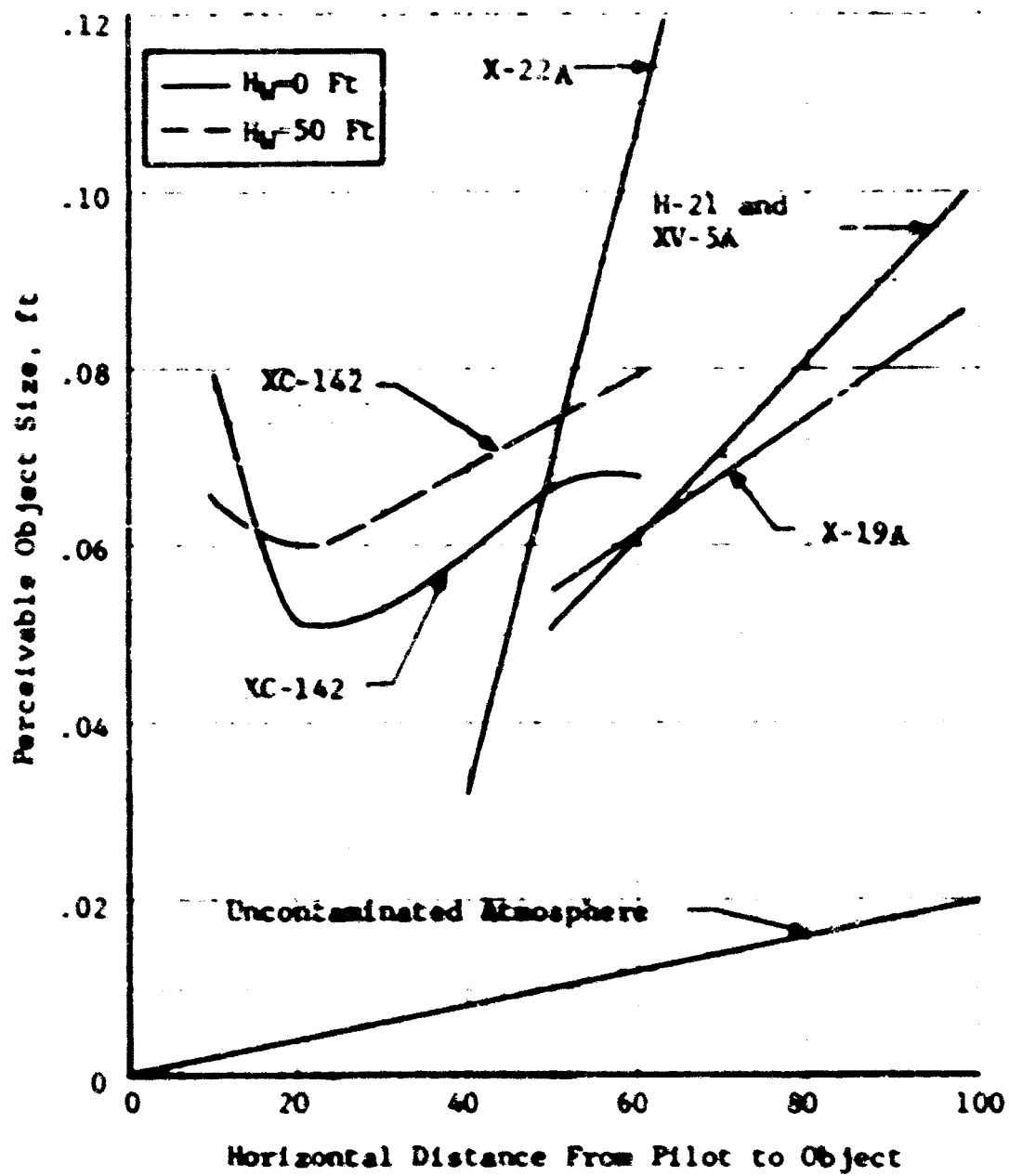


Figure 61. Perceivable Size of an Object Sighted Through Dust Clouds Generated by Various Aircraft.

- (3) Erosion of compressor blade tips and stator vane roots.
- (4) Scale-like dirt accumulation.

The leading edge bending and peening of the first and possible second stage compressor blades is caused by ingestion of large size particles (greater than 200 microns). These particles, which are subsequently reduced in size through a direct impact on the first stage compressor blades and the small size particles (less than 200 microns) directly ingested, cause trailing edge rounding of compressor blades in the second and succeeding stages.

The ingested sand and dust which is centrifuged outward as it proceeds axially causes erosion of compressor blade tips and stator vane roots. As a result of this damage, the mass distribution of both compressor blades and stator vanes changes such that the natural frequency of the compressor blades is increased while that of the stator vanes is reduced.

Scale-like dirt has been found accumulated on diffuser combustion chamber and other engine components after prolonged engine operations in contaminated atmosphere.

b. Deterioration in Engine Performance

As shown in References 22 through 27, sand and dust ingestion adversely affects engine performance. Continued operation in the contaminated atmosphere will produce damage which in turn reduces engine available power and increases engine fuel consumption.

Analysis of the test data presented in References 22 through 27 indicates that engine power loss can be related to the accumulated weight of ingested sand and dust. Figure 62 presents trends of ingested sand and dust weight as a function of engine airflow corresponding to a 5-percent reduction in engine normal rated power.

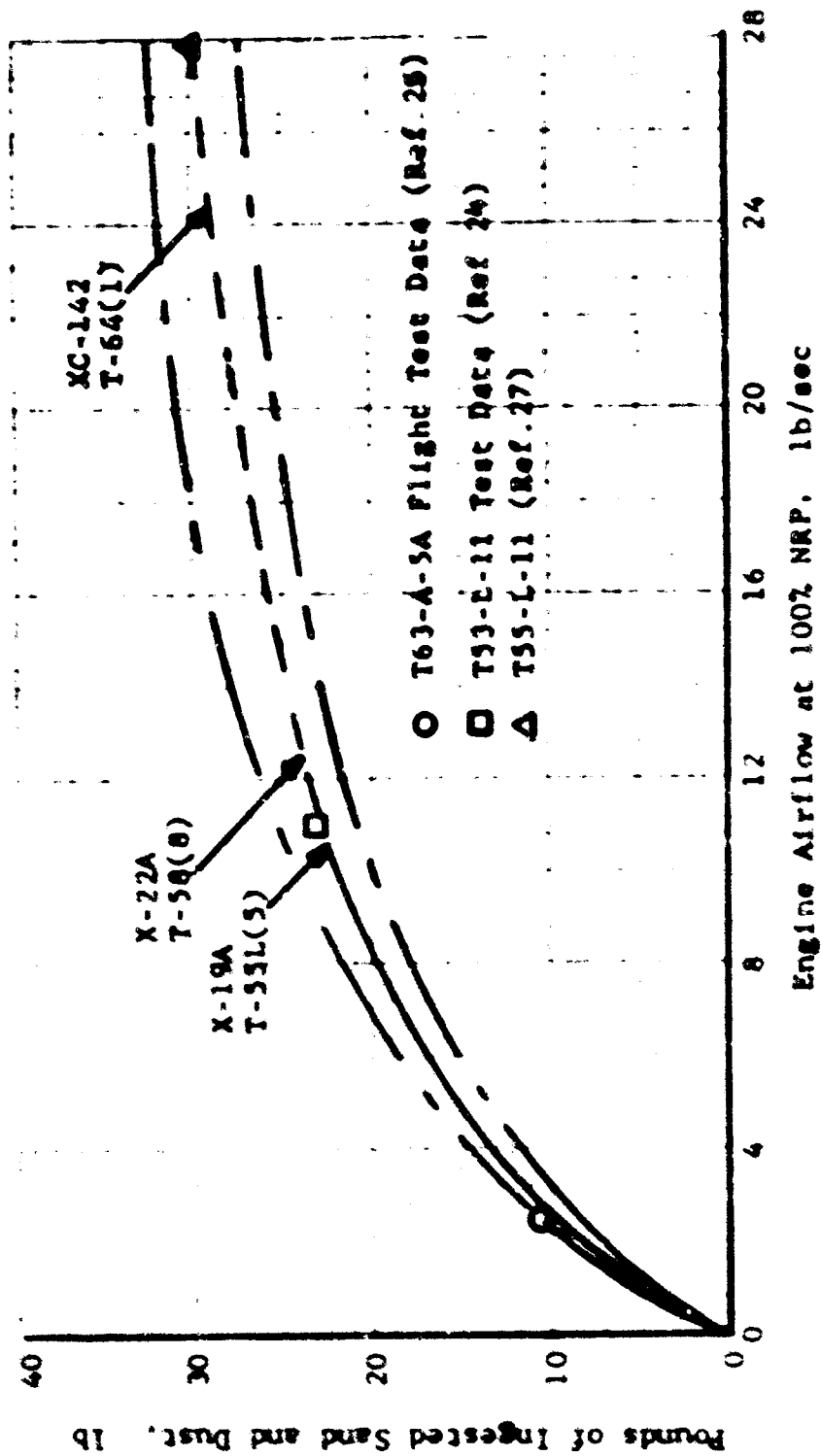


Figure 62. Variation of Engine Ingested Sand and Dust With Engine Airflow for a 5-Percent Reduction in Normal Rated Power.

The results presented in this figure are based on limited test data obtained for the T-53-2 engine (Reference 25) and the T-55-L-11 engine (Reference 27). These results can be extrapolated to other V/STOL aircraft engines. A bandwidth of approximately  $\pm 10\%$  (from the available test data) is shown in this figure to account for variations in susceptibility of a particular engine design to damage and relative hardness of the contaminant material.

Figure 62 also shows the amount of sand and dust which can be ingested by the T-64(1), T-58(8), and T-55L(5) engines, prior to 5-percent loss in normal rated power. Based on these results, the engine endurance corresponding to the XC-142, X-22A, and X-19A aircraft has been calculated and is presented in Table V.

c. Improvements Offered by Dust Filtration

Considerable improvements in engine life and performance is possible with sand and dust filtration. The degree of this improvement, as indicated in Figure 63, is very much dependent on filtration efficiency of air particle separators installed on the engines. Figure 63 shows that even with the current air particle separator designs (75% to 90-percent filtration efficiency), net operational gain in engine endurance of 4 to 10 is achievable. The net operational gain is herein defined as the ratio of engine endurance with particle filtration (protected engine) to that with no particle filtration (unprotected engine) corresponding to 5-percent reduction in engine normal rated power.

The filtration efficiency warranted for a given design is a function of engine susceptibility to the particle damage and engine maintenance schedule desired. As shown in Figure 63, the net operational gain increases very rapidly with filtration efficiency beyond 80 percent and becomes large at 100-percent filtration efficiency.

TABLE V				
RESULTS OF DUST INGESTION BY VARIOUS V/STOL ENGINES FOR A 5-PERCENT REDUCTION IN NORMAL RATED POWER				
Aircraft	Sand Ingested (lb)	Airflow (lb/sec)	$\rho_P$ (lb/ft <sup>3</sup> )	Engine Endurance (minutes)
XC-142	29	24.5	$7.7 \times 10^{-5}$	20
X-22A	24	12.4	$34.2 \times 10^{-5}$	7.2
X-19	22.5	10.7	$2.7 \times 10^{-5}$	99

### 3. Personnel and Ground Equipment Damage

This section presents the effects of rotor downwash signature on personnel and ground equipment in terms of primary and secondary wind damage. Primary damage relates to direct injury to man and destruction of equipment. Secondary damage pertains to the indirect effect of downwash upon man and equipment such as impaired work capabilities of a man or displacement of objects placed in the rotor downwash environment.

Based on the test data of Reference 10, rotor downwash impingement can directly cause injury to man. The extent of injury can vary from damage to loose areolar tissues about the eyes at wind speeds of 100 knots, to severe confluent subconjunctival hemorrhages at speeds of 515 knots. Figure 64 graphically presents levels of direct and indirect damage to man and equipment due to impingement of downwash velocities generated by the selected aircraft.

Comparing the results of Figure 64, it can be noted that the downwash velocity from the X-19A, X-22A, XV-5A, and XC-142 aircraft at respective distances of up to 13, 20, 26, and 36 feet can cause a serious injury to man's eye areolar tissues.

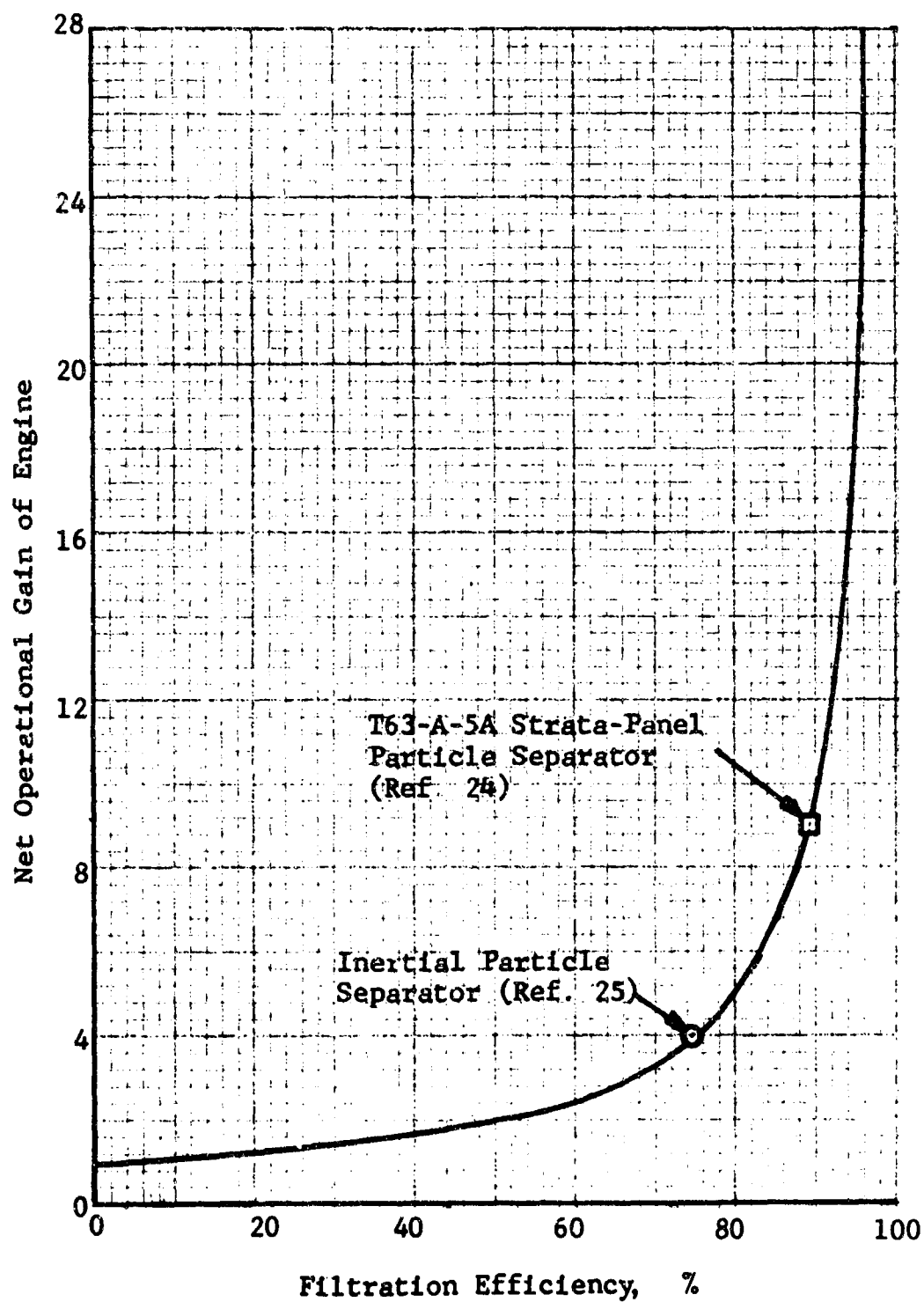


Figure 63. Engine Net Operational Gain for a 5-Percent Reduction in Normal Rated Power.

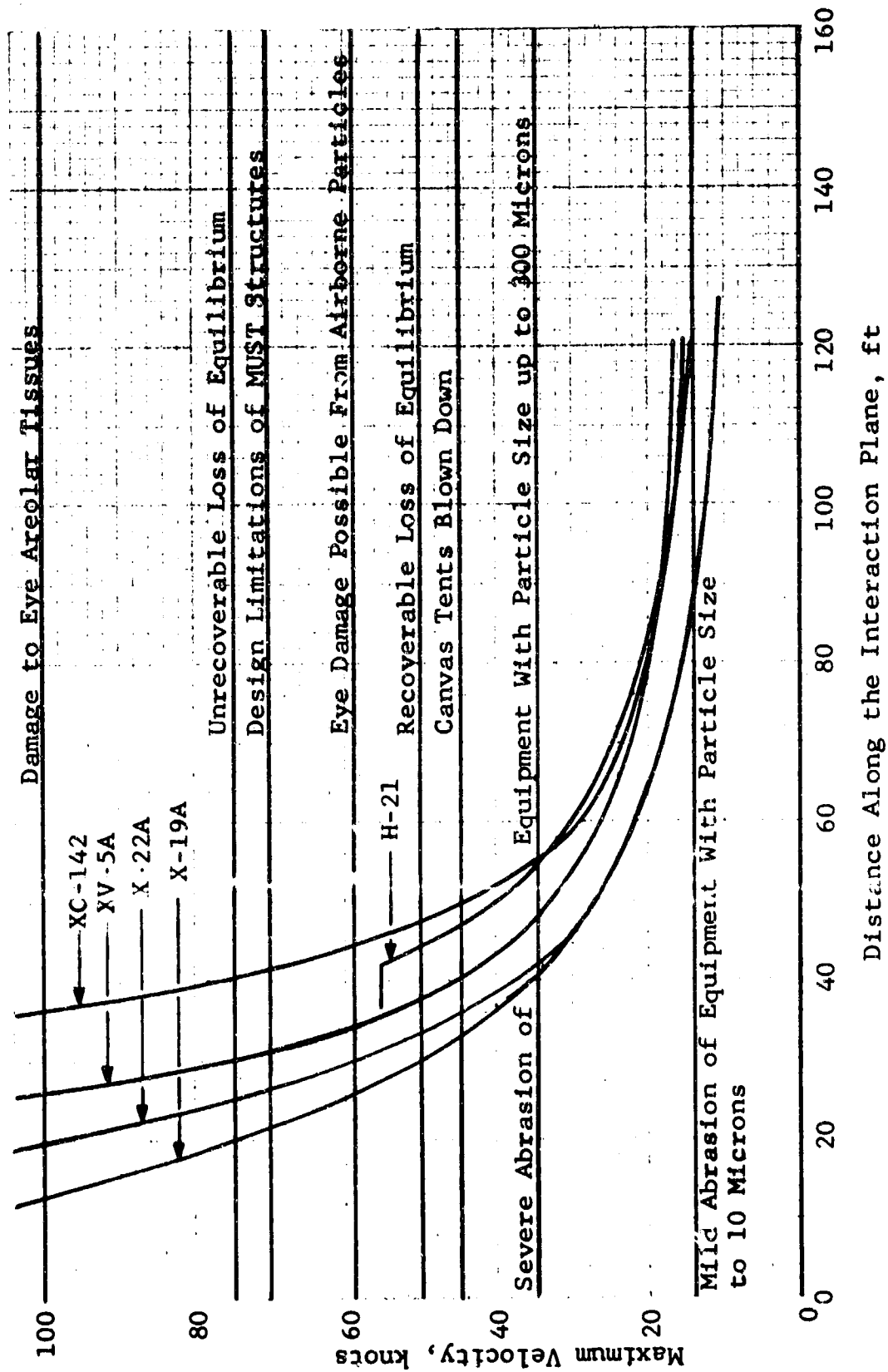


Figure 64. Effects of Rotor Downwash Upon Man and Equipment for Various Aircraft. Wheels on the Ground.



Also, the design limitations of MUST structures can be exceeded in the downwash environment generated by the four aircraft at distances of up to 21.5, 26, 31, and 41.5 feet, respectively. These design limitations of MUST structures would not be exceeded by the downwash velocities of the H-21 helicopter. Canvas tents can be blown down by the downwash velocities of each of the five selected V/STOL aircraft. These velocities can cause a severe penetration and abrasion of equipment with particle sizes of up to 300 microns. This type of equipment damage can be incurred at distances up to 40 to 60 feet from each aircraft.

In general, it can be stated that the high-disc-loading aircraft such as the XC-142, X-22A, X-19A, and XV-5A are potentially capable of generating a more hazardous downwash environment to man and equipment than the low-disc-loading V/STOL aircraft such as the H-21.

#### IV. CONCLUSIONS AND RECOMMENDATIONS

1. The analytical methods presented herein for predicting rotor downwash signatures generally correlate well with the limited test data.
2. High downwash velocities generated by high-disc-loading aircraft decay much more rapidly than the low velocities generated by low-disc-loading aircraft. As a result, the latter velocities generated in ground effect persist at greater radial distances along the ground.
3. For the type of terrain analyzed, the size of a dust cloud generated by a V/STOL aircraft is primarily dependent on aircraft gross weight rather than rotor disc loading. The maximum cloud sizes reduce slightly with increasing disc loading (constant gross weight) but reduce appreciably with reduction in aircraft gross weight.
4. The pilot's far-field visibility through a dust cloud depends upon the density and size of the cloud and the location of the sighted object relative to the pilot.
5. Sand and dust ingestion in V/STOL engines causes severe damage to engine components, thus reducing engine life and resulting in appreciable reduction in engine performance. Particle separators with filtration efficiencies in excess of 80 percent are required for any VTOL aircraft for sustained operations in sand and dust environment.
6. High-disc-loading aircraft are potentially capable of generating a more hazardous downwash environment to man and equipment than low-disc-loading aircraft.
7. It is recommended that further tests be conducted to define better and to confirm more firmly the analytical methods for predicting the rotor downwash signatures.

## V. REFERENCES

1. Heyson, H. H., "An Evaluation of Linearized Vortex Theory as Applied to Single and Multiple Rotors Hovering in and out of Ground Effect", NASA TND-43, September 1959.
2. Fradenburgh, E. A., "Flow Field Measurements for a Hovering Rotor Near the Ground", Fifth Annual Western Forum, American Helicopter Society, Inc., September 1958.
3. Goland, L., "The Normal Induced Velocity in the Vicinity of a Thrust Rotor", University of Pennsylvania Dissertation, 1962, Dynasciences Corporation Report No. DCR-12, December 1962.
4. Heyson, H. H., and Katzoff, S., "Induced Velocities Near a Lifting Rotor With a Nonuniform Disk Loading", NACA Report 1319, 1957.
5. Gessow, A., and Myers, G. C., Jr., "Aerodynamics of the Helicopter", The MacMillan Company, 1952.
6. Heyson, H. H., "Induced Velocity Near a Rotor and Its Application to Helicopter Problems", Proceedings of the Fourteenth Annual Forum, American Helicopter Society, Inc., April 1958.
7. Ludwig, G. R., and Brady, W. G., "Theoretical and Experimental Studies of Impinging Uniform and Nonuniform Jets", TRECOM Technical Report 64-42, U.S. Army Aviation Materiel Laboratories, Fort Eustis, Virginia, August 1964.
8. Glauert, M. B., "The Wall Jet", Journal of Fluid Mechanics, Vol. 1, Pt. 6, December 1956.
9. George, M. M., and Perlmutter, A. A., and Butler, L., "Downwash Impingement Design Criteria for VTOL Aircraft", TRECOM Technical Report 64-48, U.S. Army Aviation Materiel Laboratories, Fort Eustis, Virginia, August 1964.

10. Schane, W. P., LTC, MC, "Effects of Downwash Upon Man", USAARU Report No. 68-3, U. S. Army Aeromedical Research Unit, Fort Rucker, Alabama, November 1967.
11. Bolonovich, M., and Marks, M. D., "Experimental Downwash Velocity, Static Pressure, and Temperature Distributions in Ground Effect for a 75-Foot Jet Driven Rotor", AHS Journal, Vol. 4, No. 2, April 1959.
12. Newsom, W. A., and Tosti, L. P., "Slipstream Flow Around Several Tilt-Wing VTOL Aircraft Models Operating Near Ground", NASA TND-1382.
13. Morse, A., and Newhouse, H., "VTOL Downwash Impingement Study - Surface Erosion Tests", TREC Technical Report 60-67, U. S. Army Aviation Materiel Laboratories, Fort Eustis, Virginia, October 1960.
14. Coronato, A. A., "Overhaul on Condition - Eliminate Time Between Overhaul", Sikorsky Aircraft, Division of United Aircraft Corporation, Stratford, Connecticut, AHS Seventeenth Annual National Forum, May 3-5, 1961, Washington, D.C.
15. Rodgers, S. J., "Evaluation of the Dust Cloud Generated by Helicopter Rotor Blade Downwash", USAAVLABS Technical Report 67-81, U. S. Army Aviation Materiel Laboratories, Fort Eustis, Virginia, March 1968.
16. Spreiter, J. R., and Sacks, A. H., "The Rolling Up of the Trailing Vortex Sheet and Its Effect on the Downwash Behind Wings", Aerodynamics Session, Eighteenth Annual Meeting, I.A.S., New York, January 23-26, 1950.
17. Bagnold, R. A., FRS, "The Physics of Blown Sand and Desert Dunes", Methuen and Company LTD, London, July 1953.
18. Kuhn, R. E., "An Investigation to Determine Conditions Under Which Downwash From VTOL Aircraft will Start Surface Erosion From Various Types of Terrains", NASA TND-56, September 1959.

19. Bartley, S. H., "The Psychophysiology of Vision", Handbook of Experimental Psychology (edited by S. S. Stevens), John Wiley and Sons, Inc., New York, Chapman and Hall Ltd., London, 1951.
20. Watzen, E., "Amount of Dust Recirculated by a Hovering Helicopter", Kaman Aircraft Corporation Report No. R-169, Bloomfield, Connecticut, December 1956.
21. Pruyn, R. R., "Effects of Airframe Geometry on Downwash Problems of Tandem Ducted - Propeller VTOL Aircraft", Kellett Aircraft Corporation Report No. KAC 179T80-6, Willow Grove, Pennsylvania, January 1964.
22. Curtis, N. C., Jr., "Downwash Tests of the Dual Tandem Ducted Propeller VTOL Research Aircraft Configurations to Evaluate Engine Inlets, Protection Devices and Study Aerodynamic Interference", Kellett Aircraft Corporation Report No. 179T80-12, Willow Grove, Pennsylvania, November 1965.
23. Anon., "Unpublished Data on the Effects of Foreign Object Ingestion on the Mission Endurance of the Vertol Model 107 (CH-46A) Helicopter", Vertol Division of the Boeing Company, Morton, Pennsylvania.
24. Connors, H. D., "Development of the Lycoming Internal Particle Separator", Proceedings of the Seventh Annual National Conference on Environmental Effects on Aircraft and Propulsion Systems", Report No. 67-ENV-5, Princeton, New Jersey, September 1967.
25. Bianchini, G. V., "Field Evaluation of an Air Cleaner for the T63 Engine Powered OH-6A Aircraft", Proceedings of the Seventh Annual National Conference on Environmental Effects on Aircraft and Propulsion Systems, Report No. 67-ENV-6, Princeton, New Jersey, September 1967.
26. Stephenson, C. D., Shohet, H. H., and Speiden, E. F., "CH-54A and CH-53A Engine Air Particle Separator (EAPS) Development", Proceedings of the Seventh Annual National Conference on Environmental Effects on Aircraft and Propulsion Systems, Report No. 67-ENV-7, Princeton, New Jersey, September 1967.

27. Model Spec. No. 124.27 dated 15 February 1965 and Amendment No. 2 dated 12 April 1967, Revised 1 June 1967, entitled T55-L-11 Shaft Turbine Engine (Lycoming Model LTC4B-11B), Lycoming Division, AVCO Corporation, Stratford, Connecticut.

APPENDIX  
SURFACE EROSION TEST DATA

In conjunction with the tests at Yuma conducted by MSA Research Corporation (Reference 15), this contractor obtained test data on the weight and size of particles entrained from the ground and transported along the wall jet.

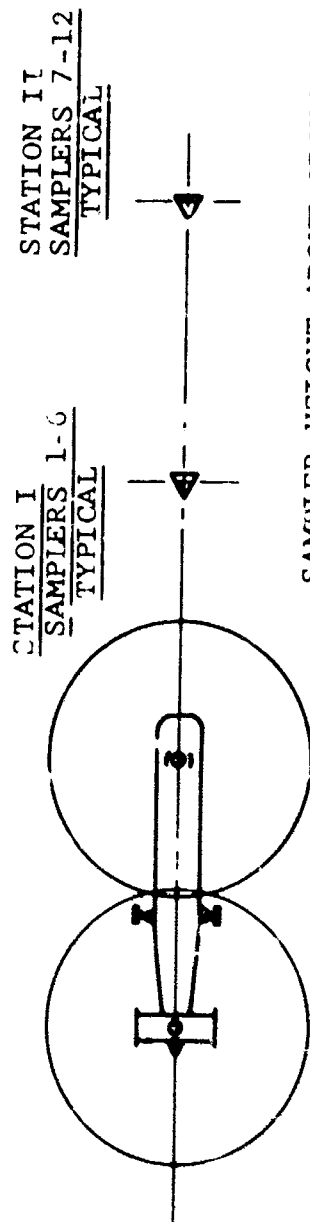
The dust particles were collected in specially designed particle traps which were located in the vicinity of the H-21 helicopter hovering in ground proximity. The particle trap layout used during the tests is shown in Figure 65. The particle traps were made from 2-3/8-inch-inside-diameter plastic tubing. The shape of the basic trap was a "T" lying on its side. The leg of the "T" was the intake for the contaminated air, and a cup was provided on the bottom for collecting the dust sample. A wire mesh screen shaped into a cone with a surface area five times the inlet area of the trap was attached to the top of the trap. This was used as a filter which collected the dust particles while permitting the now clear air to flow out of the trap. The filter screen was made from 200 mesh wire cloth with 33.6-percent open area. The size of the screen openings was 0.0029 inch.

Six particle traps were mounted on a boom to a height of 10 feet, as shown in Figure 65. Two booms with a total of 12 traps were used for these tests. The location of the booms was varied from the front to the side of the helicopter depending on the sampling method selected for the particular test.

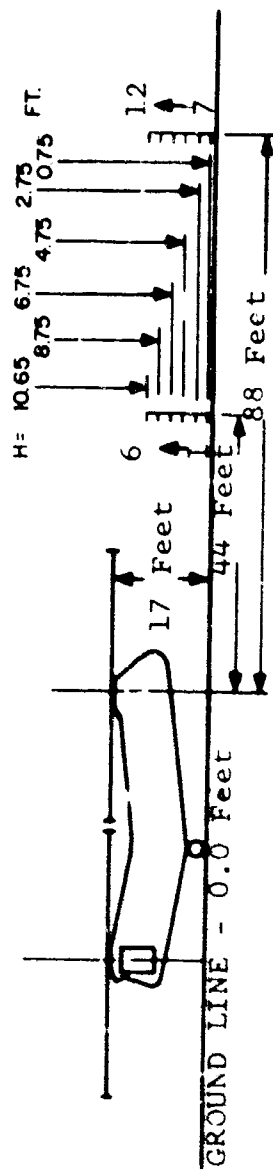
During all tests, a target was placed in the pilot's view, providing him with heading and distance information from the first sampler location. The pilot approached the target point, hovered at an altitude of approximately 1 foot wheel clearance for a specified period of time, and quickly backed away from the test area.

Data were obtained for a total of nine tests; four of these tests were selected as providing the most reliable data. The results for the remaining tests were questionable because of the conditions encountered during testing; i.e., the

TEST CONDITION I



SAMPLER HEIGHT ABOVE GROUND - FEET



(a) Test Condition I

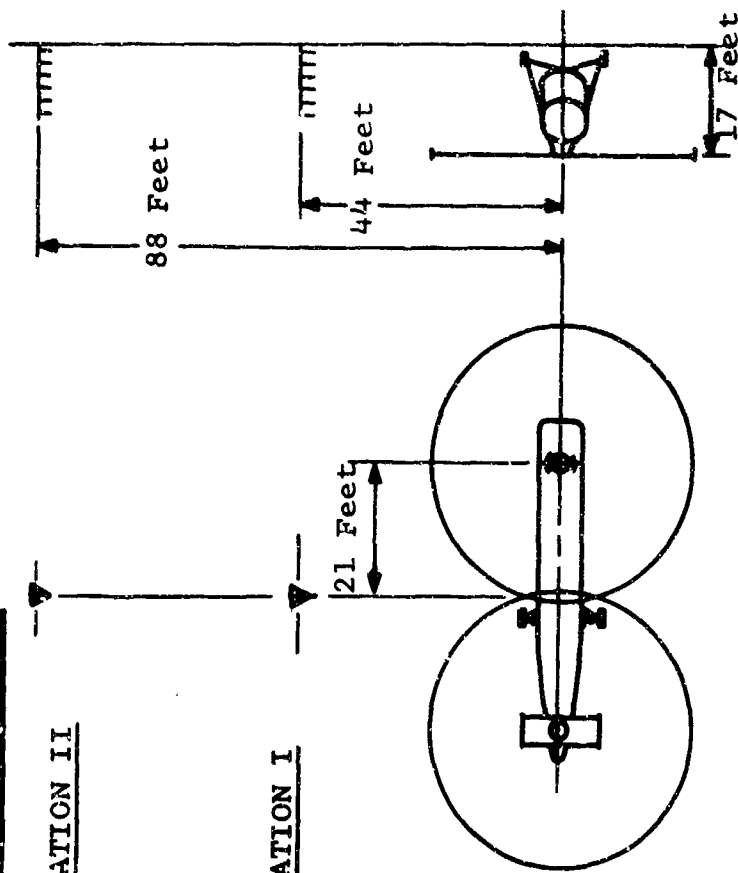
Figure 65. Particle Trap Layout.



TEST CONDITION II

STATION II

STATION I



(b) Test Condition II

Figure 65. Continued.

excessive surface winds, the poor orientation of helicopter with respect to the samplers, the undeterminable time of operation of the helicopter in the vicinity of the samplers, etc.

All samples collected were analyzed by the Vicksburg Waterways Experimental Station. The following information was obtained:

1. Weight of particles.
2. Size distribution of particles for selected samplers.
3. Maximum size of particles found in each sample.

The test data for Test Condition I, Run No. 5 and Run No. 7 and for Test Condition II, Run No. 4 and Run No. 9 are presented in Tables VI, VII, VIII, and IX, respectively. These tables show particle mass flow rates measured along longitudinal axis (Test Condition I) and lateral axis (Test Condition II) of the H-21 helicopter. The collection of data from both the front and side of the aircraft was performed to determine any variations that might exist in surface erosion due to the downwash interaction effects of the two rotors.

The results obtained from these tests at two radial stations from the front and sides of the H-21 helicopter are summarized in Figures 66 through 69.

The mass flow data are presented in Figures 66 and 67 for the front and side of the helicopter, respectively. The flow data are given in pounds of sand collected per second per unit area and are plotted as a function of height above the ground.

In Figure 66 the mass flow rate of particles measured along the front of the H-21 helicopter, as expected, is seen to decrease with increasing height above the ground. What is unusual, however, is that with the exception of the region very close to the ground, the flow rate increased with increasing radial distance. This is contrary to data obtained in Reference 13 for the 2-foot ducts. These data are

TABLE VI											
GRADATION TEST RESULTS - TEST CONDITION I, RUN NO. 5											
H-21 YUMA SAND AND DUST TESTS											
Run No. 5		Time: 4.0 Minutes			Condition - I						
Sample No.	Total Weight (grams)	Percent Finer by Weight (microns)							Maximum Particle Size		
		1000	500	250	74	58	36	18	14.5		
1	1.520	98.7	87.9	41.9	4.9	3.0	1.1	0.6	0.4	2000	
2	3.218									1700	
3	3.349	99.2	94.8	66.1	9.3	4.5	1.2	0.7	0.5	1700	
4	1.261									1300	
5	0.559									750	
6	0.321	100.0	99.0	86.7	18.9	10.2	4.6	2.2	1.9	750	
7	1.901	99.4	95.0	63.5	10.5	5.7	2.7	1.6	1.2	1700	
8	4.297									1700	
9	9.391	99.7	98.3	78.4	11.9	7.8	2.8	1.4	0.9	1300	
10	5.634									750	
11	2.958									750	
12	1.653	100.0	93.5	92.1	18.9	5.3	2.1	1.4	1.0	750	

TABLE VII												
GRADATION TEST RESULTS - TEST CONDITION I, RUN NO. 7												
H-21 YUMA SAND AND DUST TESTS												
Run No. 7	Time: 2 Minutes					Condition - I						
	Sample No.	Total Weight (grams)	Percent Finer by Weight (microns)					Maximum Particle Size				
			1000	500	250	74	58	36	18	14.5		
1		37.518	99.6	95.5	62.4	5.0	2.0	1.0	1.0	0.8		2000
2		1.291										1100
3		0.750	100.0	99.7	88.3	14.1	7.6	1.8	1.4	0.5		750
4		0.540										750
5		0.341										375
6			100.0	100.0	95.1	28.8	15.5	5.0	3.5	2.4		375
7		31.489	99.6	97.8	76.8	12.4	4.2	3.1	2.1	1.2		2000
8		9.545										1300
9		4.311	100.0	99.2	85.2	8.6	5.3	3.3	1.8	1.2		750
10		1.975										750
11		0.892										750
12		0.448	100.0	100.0	95.6	22.9	8.5	3.8	3.6	3.0		375

TABLE VIII											
GRADATION TEST RESULTS - TEST CONDITION II, RUN NO. 4											
H-21 YUMA SAND AND DUST TESTS											
Run No. 4	Time: 5 Minutes				Condition - II						
Sample No.	Total Weight (grams)	Percent Finer by Weight (microns)					Maximum Particle Size				
		1000	500	250	75	36	18	14.5			
1	89.895	99.6	96.4	67.7	8.1	3.9	1.9	1.2	0.8		2000
2	8.132										1100
3	2.339	100.0	98.0	76.2	12.4	6.4	3.6	1.2	1.0		750
4	1.070										750
5	0.572										1300
6	0.339	100.0	99.5	93.3	25.3	16.7	3.8	2.3	1.7		750
7	163.701	99.7	95.5	61.9	12.6	6.7	4.0	1.9	1.4		2000
8	18.619										2000
9	9.009	99.8	97.9	74.7	10.0	6.0	2.2	1.1	0.7		1300
10	-										
11	2.003										750
12	1.130	100.0	99.1	84.2	18.4	10.6	5.7	3.8	2.8		750

TABLE IX											
GRADATION TEST RESULTS - TEST CONDITION II, RUN NO. 9											
H-21 YUMA SAND AND DUST TESTS											
Run No. 9		Time: 2 Minutes			Condition - II						
Sample No.	Total Weight (grams)	Percent Finer by Weight (microns)							Maximum Particle Size		
		1000	500	250	74	58	36	18			
1	77.992	99.1	90.1	49.2	4.7	2.9	1.6	0.8	0.6	2000	
2	6.215									1700	
3	1.225	99.1	94.0	62.8	9.7	6.0	2.1	1.2	0.8	1100	
4	0.403									750	
5	0.255									750	
6	0.180	100.0	99.3	81.8	28.6	16.6	6.2	3.1	2.3	750	
7	68.189	99.3	95.2	65.6	14.6	5.4	4.7	4.1	3.4	2000	
8	12.880									2000	
9	7.109	99.8	96.2	68.2	6.6	8.5	1.5	0.9	0.6	1700	
10	2.429									1700	
11	1.791									750	
12	0.979	100.0	99.5	75.5	14.1	8.2	3.6	1.9	1.4	750	

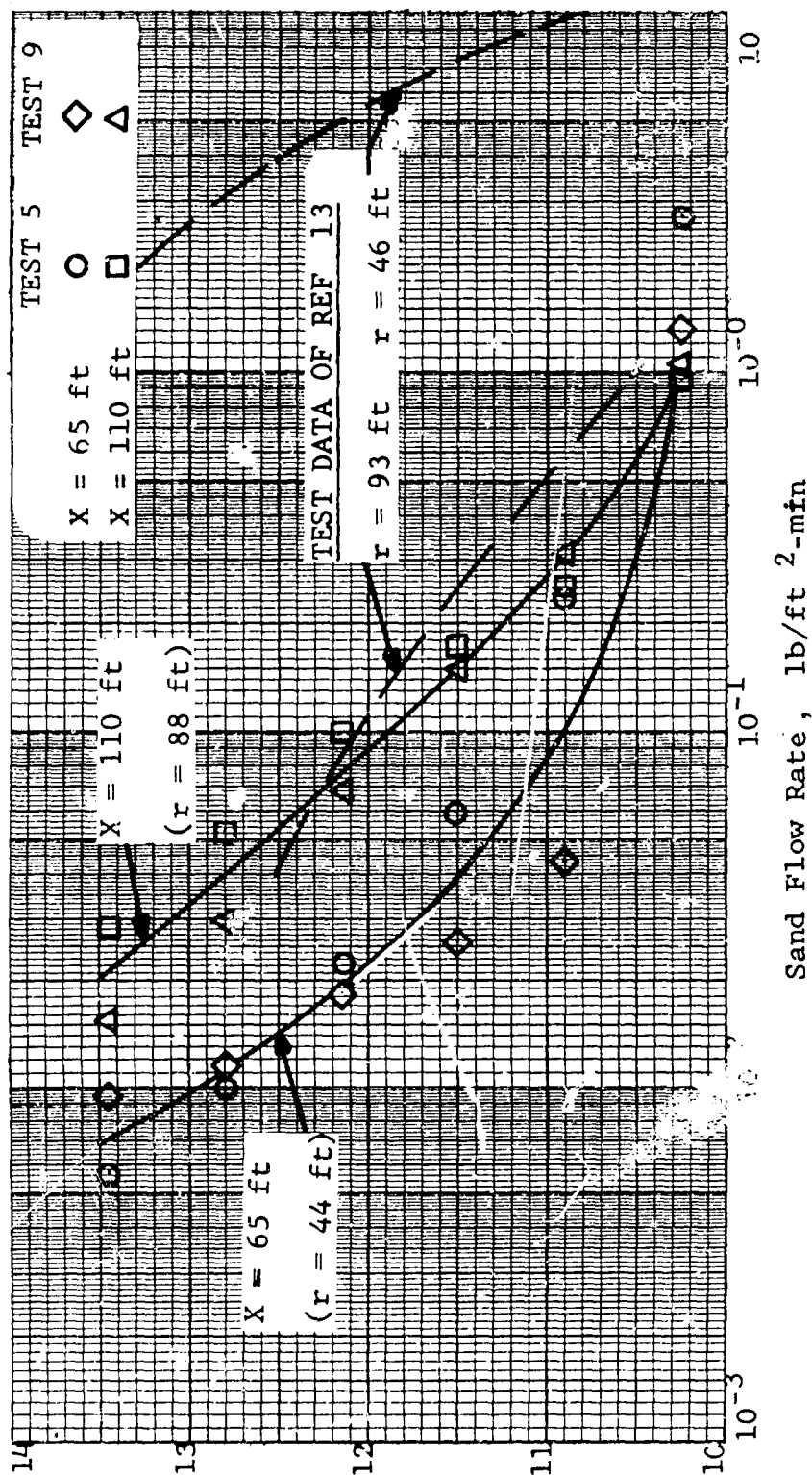


Figure 66. Mass Erosion Rates of Particles Entrained Forward of the H-21 Helicopter, Test Condition I - Phillips Drop Zone, H = 17 Feet.

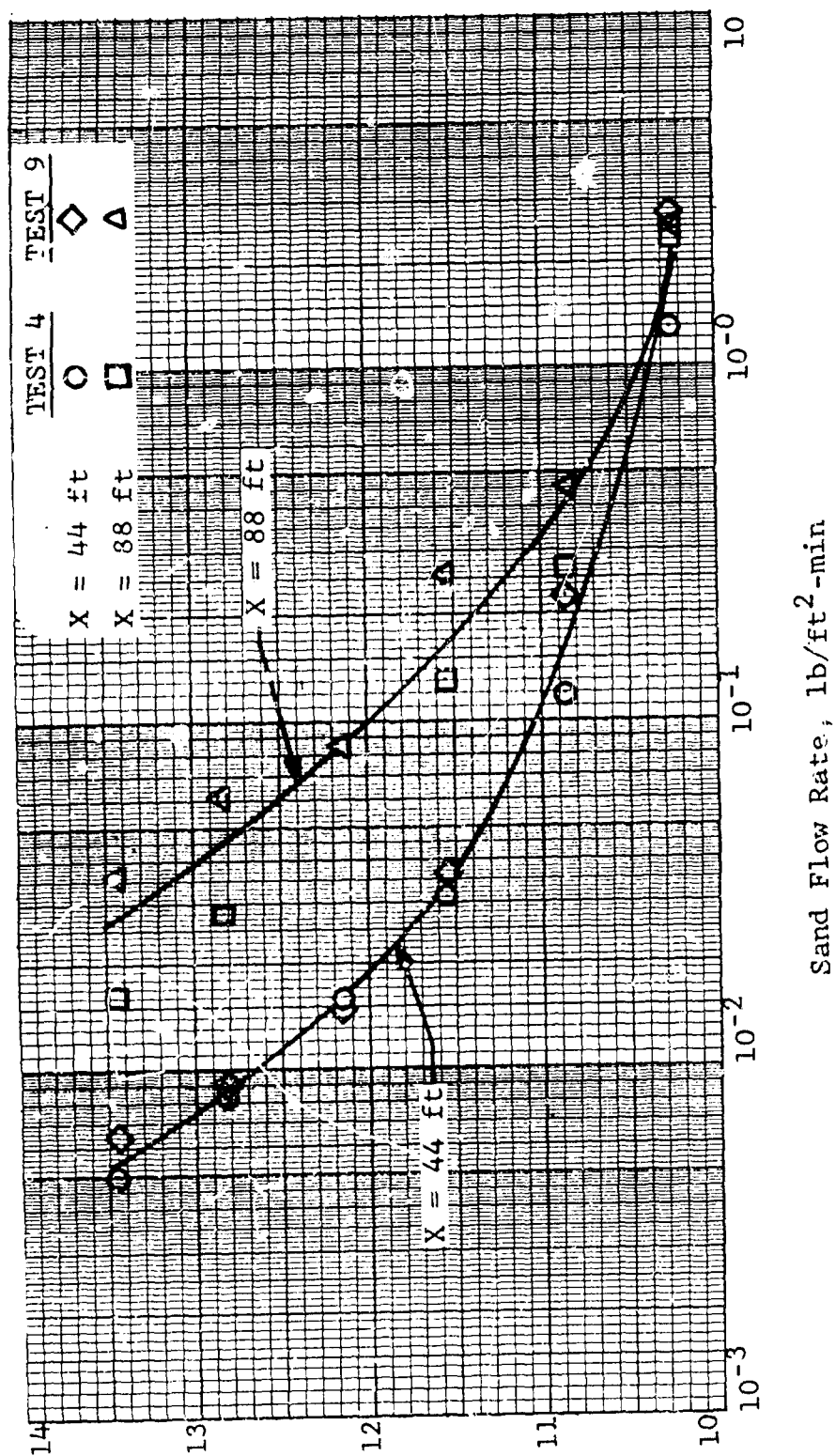


Figure 67. Mass Erosion Rates of Particles Entrained Outboard of the H-21 Helicopter, Test Condition II - Phillips Drop Zone, H = 17 Feet.



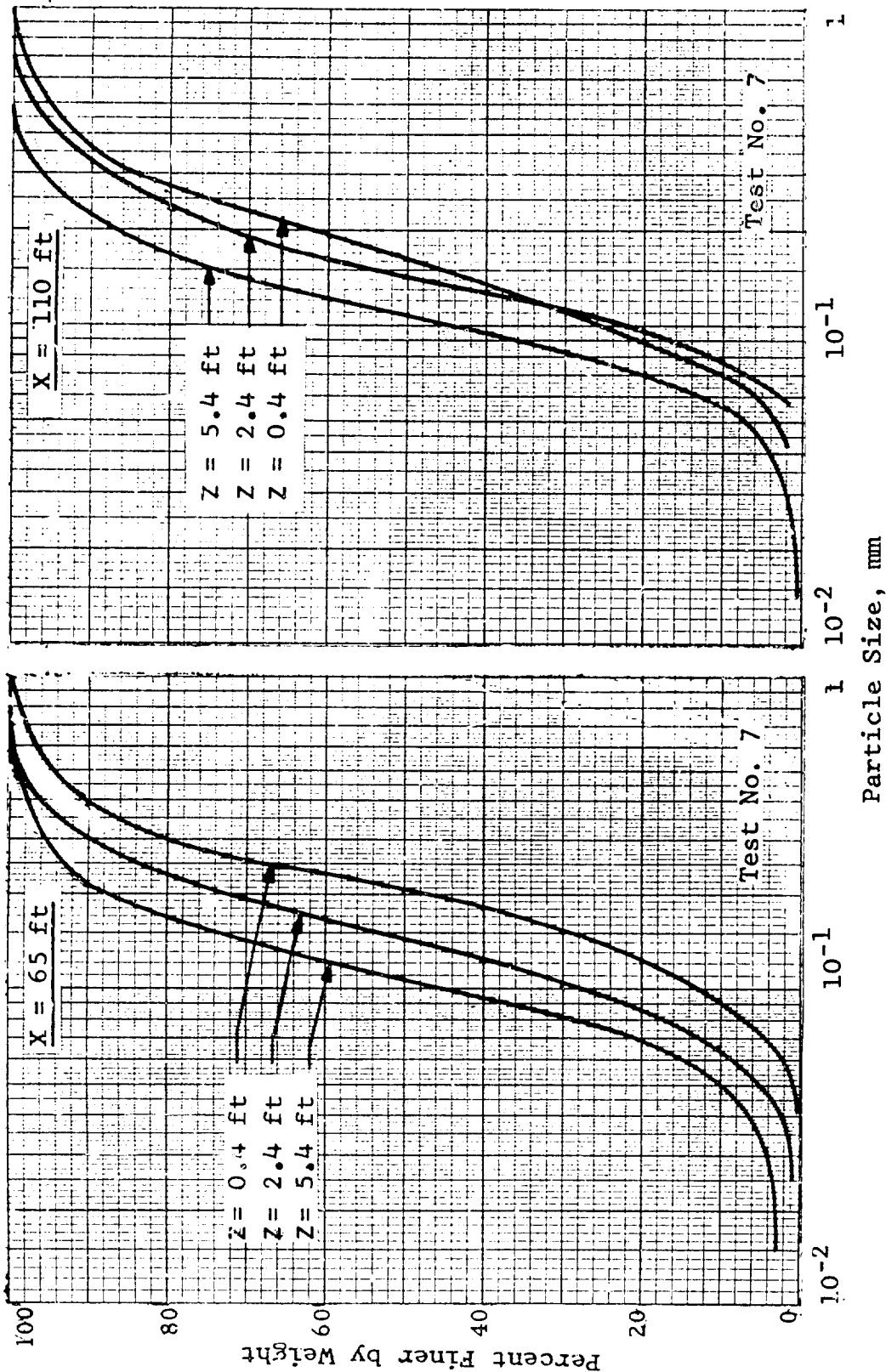


Figure 68. Particle Size Distribution Forward of the H-21 Helicopter, Test Condition I - Phillips Drop Zone,  $H = 17$  Feet.

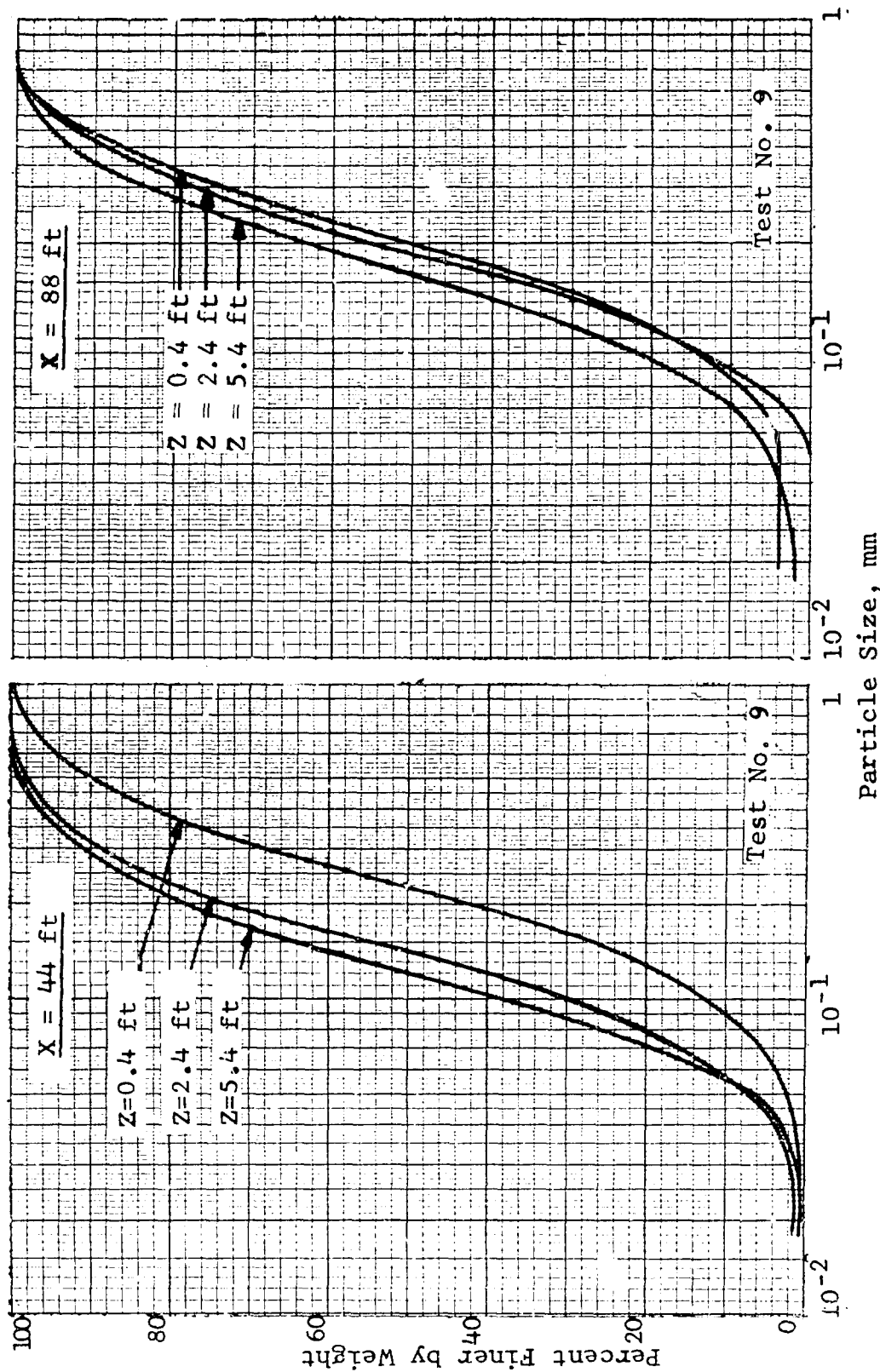


Figure 69. Particle Size Distribution Outboard of the H-21 Helicopter, Test Condition II - Phillips Drop Zone, H = 17 Feet.

superimposed on Figure 66 for comparison. The observation of the sand flow along the ground as reported by the pilot confirms the results obtained during this program. According to the pilot's observations, the entrained sand started to erode just in front of the first row of samplers and billowed upward to engulf the aft row of samplers completely. As a result of this flow mechanism, a majority of the sand particles were trapped very close to the ground by the first row of samplers and at higher locations from the ground by the second row. More data are required to define the point where the cross-over of flow rate will occur.

The flow rates along the side of the helicopter were obtained along a plane midway between the two rotors perpendicular to the longitudinal axis of the aircraft (interaction plane). These data are presented in Figure 67 as a function of height above the ground for two radial stations. The flow rates as shown in this figure are very similar to the data obtained along the front of the aircraft both in magnitude and variation with height. It appears that the amount of eroded particles does not significantly change due to the interaction of the two rotors even though the particles are transported further out radially.

The size distribution of particles collected in the samplers has been obtained for the same test conditions as those described previously. The results are presented in Figures 68 and 69 for the front and side of the helicopter, respectively. From these figures, it can be seen that the particle size reduces with an increase in both height above ground and radial location.

Unclassified

Security Classification

DOCUMENT CONTROL DATA - R & D		
<small>(Security classification of title, body of abstract and indexing annotation must be entered when the overall report is classified)</small>		
1. ORIGINATING ACTIVITY (Corporate author)		2A. REPORT SECURITY CLASSIFICATION
Dynasciences Corporation Blue Bell, Pennsylvania 19422		Unclassified
3. REPORT TITLE		2B. GROUP
INVESTIGATION OF THE DOWNWASH ENVIRONMENT GENERATED BY V/STOL AIRCRAFT OPERATING IN GROUND EFFECT		
4. DESCRIPTIVE NOTES (Type of report and inclusive dates)		
Final Report		
5. AUTHOR(S) (First name, middle initial, last name)		
M. George E. Kisielowski D. S. Douglas		
6. REPORT DATE	7A. TOTAL NO. OF PAGES	7B. NO. OF REFS
July 1968	149	27
8A. CONTRACT OR GRANT NO.	8B. ORIGINATOR'S REPORT NUMBER(S)	
DA 44-177-AMC-316(T)	USAAVLABS Technical Report 68-52	
A. PROJECT NO.	9A. OTHER REPORT NO(S) (Any other numbers that may be assigned this report)	
1T021701A047	Dynasciences Report No. DCR-275	
10. DISTRIBUTION STATEMENT		
This document has been approved for public release and sale; its distribution is unlimited.		
11. SUPPLEMENTARY NOTES		12. SPONSORING MILITARY ACTIVITY
		U. S. Army Aviation Materiel Laboratories, Ft. Eustis, Virginia
13. ABSTRACT		
<p>Analytical methods are developed for determining the downwash environment generated by multicopter/propeller V/STOL aircraft configurations operating in ground proximity.</p> <p>These methods are utilized to compute rotor flow field and contaminant dust cloud characteristics (including particle density and size distributions) for the H-21, XC-142, X-22A, X-19A, and XV-5A aircraft. The effects of the contaminated atmosphere on pilot's visibility, ground equipment, and personnel are also determined for these aircraft.</p> <p>The theoretically predicted results are generally in good agreement with the limited test data. Additional full-scale test data are required to verify further the assumptions inherent in the theory.</p>		

DD FORM 1473

REPLACES DD FORM 1473, 1 JAN 64, WHICH IS OBSOLETE FOR ARMY USE.

Unclassified

Security Classification

Unclassified

Security Classification

14. KEY WORDS	LINK A		LINK B		LINK C	
	ROLE	WT	ROLE	WT	ROLE	WT
Rotor Downwash Mass Flow Rate Particle Density Disc Loading Cloud Content						

Unclassified

Security Classification